



**AALBORG UNIVERSITY**  
DENMARK

**Aalborg Universitet**

## **Openings in Wind Driven Natural Ventilation**

True, Jan Per Jensen

*Publication date:*  
2003

*Document Version*  
Early version, also known as pre-print

[Link to publication from Aalborg University](#)

*Citation for published version (APA):*

True, J. P. J. (2003). *Openings in Wind Driven Natural Ventilation*. Dept. of Building Technology and Structural Engineering, Aalborg University.

### **General rights**

Copyright and moral rights for the publications made accessible in the public portal are retained by the authors and/or other copyright owners and it is a condition of accessing publications that users recognise and abide by the legal requirements associated with these rights.

- Users may download and print one copy of any publication from the public portal for the purpose of private study or research.
- You may not further distribute the material or use it for any profit-making activity or commercial gain
- You may freely distribute the URL identifying the publication in the public portal -

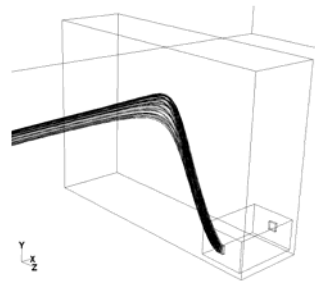
### **Take down policy**

If you believe that this document breaches copyright please contact us at [vbn@aub.aau.dk](mailto:vbn@aub.aau.dk) providing details, and we will remove access to the work immediately and investigate your claim.



---

# Openings in Wind Driven Natural Ventilation



**Phd. Thesis**

**Aalborg University**

**Jan P. Jensen True**

---

## CONTENTS

<b>1. Introduction.....</b>	<b>4</b>
1.1. Natural ventilation.....	5
1.1.1. Driving forces for Natural ventilation.....	5
1.1.2. Outdoor climate and microclimate.....	9
1.2. Description of Problem .....	11
1.3. Scope of work .....	14
<b>2. Fluid Flow .....</b>	<b>16</b>
2.1. Types of flow .....	16
2.1.1. Flow separation.....	19
2.2. Governing flow equations .....	20
2.2.1. Conservation of Mass .....	20
2.2.2. Conservation of Momentum .....	21
2.2.3. Conservation of Energy .....	24
2.3. Jet flow theory.....	26
2.3.1. Measurements of airflow from bottom hung windows used for natural ventilation .....	29
2.4. Measurement of airflow .....	34
2.4.1. The Bernoulli Equation.....	35
2.4.2. flow through a constriction .....	36
2.4.3. The Sharp edged orifice .....	37
2.4.4. Orifice flow vs. Flow through openings in buildings .....	42
2.5. Crack flow and flow through large openings .....	44
2.6. Airflow around buildings .....	49
2.6.1. Flow pattern around building.....	50
2.6.2. Wind Profile.....	52
2.7. Similarity principles .....	53
<b>3. Measurements and methods.....</b>	<b>55</b>
3.1. Experimental Methods .....	55
3.1.1. Pressure measurements .....	55
3.1.2. Velocity measurements.....	57
3.2. Wind tunnel.....	57
<b>4. Computational Fluid Dynamics.....</b>	<b>59</b>

4.1.	Numerical method.....	59
4.1.1.	The finite volume method.....	59
4.2.	Turbulence modelling .....	62
4.2.1.	Mixing Length Model.....	63
4.2.2.	k- $\epsilon$ Model.....	63
4.2.3.	Reynolds stress Model.....	64
4.2.4.	Wall Functions.....	67
4.3.	Quality control of CFD .....	68
4.3.1.	Grid distribution.....	68
4.3.2.	Boundary conditions.....	72
4.3.3.	Turbulence models.....	74
<b>5.</b>	<b>Experimental and numerical analysis of Simplified cross-flow building model.....</b>	<b>77</b>
5.1.	Geometry of the models .....	78
5.2.	Experimental set-up .....	80
5.2.1.	Measurement series.....	82
5.3.	Computational fluid dynamics .....	82
5.4.	Results .....	83
5.4.1.	Velocity distribution and Airflow Pattern.....	85
5.4.2.	Pressure distribution .....	92
5.4.3.	Airflow rate.....	101
5.5.	Discussion .....	111
<b>6.</b>	<b>Experimental and numerical analysis of Building scale model</b>	
6.1.	Geometry of building scale model .....	113
6.2.	Experimental set-up .....	115
6.3.	Computational fluid dynamics .....	118
6.4.	Results and discussion.....	119
6.4.1.	Wind profile.....	119
6.4.2.	Airflow pattern.....	120
6.4.3.	Pressure distribution .....	132
6.4.4.	Airflow rate.....	153
6.5.	Discussion .....	168
<b>7.</b>	<b>Conclusions and discussion .....</b>	<b>172</b>
7.1.	General discussion .....	172
7.2.	Recommendations for future work.....	175

**Danish summary..... 177**  
**References ..... 181**

## 1. INTRODUCTION

Heating, ventilation and air conditioning of buildings (HVAC) is a large source of energy usage in the EU today (the building sector accounts for 30 % of the total energy use in the world today (IPCC, 2001)). Since the oil crisis in the beginning of the seventies and the increasing focus on global warming, engineers and other researchers have been turning their attention to energy saving precautions in connection with HVAC. The use of passive energy sources such as the sun and the wind in building and HVAC design have become increasingly popular. Heating storage in building elements, optimisation of solar heat gain and natural ventilation are examples of the usage of renewable energy sources in HVAC and building design. However still much research is needed in the design of passive technologies, especially in the design of hybrid and natural ventilation. Many implemented natural ventilation systems are not functioning as well as was intended. The design procedure for hybrid and natural ventilation is not as well established as is the case for mechanical ventilation. The use of automatic control may result in thermal user discomfort, whereas extended user control may result in poor indoor air quality which the users may not be fully aware of, but experience in other ways.

In the industrialised countries today people spend more than 90 % of their time in an artificial created environment. This emphasises the importance of the indoor environment being both healthy as well as comfortable. Therefore it is important that the design of natural ventilation accounts for both a comfortable thermal indoor environment as well as obtaining the necessary airflow rate to secure a comfortable atmospheric indoor environment. The main objective of creating a comfortable indoor environment is the wellbeing of the users of the building, but there is also another incentive since a comfortable indoor environment may reduce sickness and increase productivity.

The present thesis deals with wind driven natural ventilation, but a short overview of some common models for the determination of airflow through

openings in natural ventilation influenced by both thermal as well as wind forces is given in the following section.

## **1.1. NATURAL VENTILATION**

The concept of purpose provided natural ventilation is not a new one, but has been in use since fire places was brought into the dwelling resulting in a need for an opening in the roof to let out smoke. Today natural ventilation is undergoing a renaissance and more new buildings and refurbished buildings are being designed using natural ventilation, some well known examples are the Reichstag building in Berlin, the Commerzbank in Frankfurt and the headquarters of NCC in Copenhagen.

In order to reduce energy usage by applying natural ventilation the overall picture has to be considered. The reduction of the fan-power and the energy usage of the heating and/or cooling coil have to be compared to the energy loss by natural ventilation. Cold air entering a building has to be heated in both cases, but in natural ventilation there is no possibility of heat exchange between the incoming and outgoing air.

### *1.1.1. DRIVING FORCES FOR NATURAL VENTILATION*

The driving forces for natural ventilation are thermal buoyancy and wind. In the design of natural ventilation these forces are converted into pressure differences from which the airflow is calculated.

Dependent on the configuration of openings in the building the natural ventilation may be considered to be single-sided or cross ventilated and the effect of thermal buoyancy compared to that of the wind may vary. Figure 1.1 shows a cross ventilated and a single-sided ventilated building with an indication of the wind direction. In the shown cross ventilated case the buoyancy has no influence due to the openings being placed in the same height, however if the openings were placed in different heights the thermal buoyancy would effect the airflow and would either work with or against the wind dependent on the location of the openings and the wind direction. Usually when natural ventilation is designed to be buoyancy driven the

outlet opening is placed in the roof in order to minimize or utilize the effect of the wind. In the single-sided case the influence of the wind is for small openings limited to the fluctuations or the turbulence in the wind. If the opening has a large width compared to the building the wind can have a direct effect on single-sided ventilation since horizontal pressure gradients exist especially at angled flows. The effect of thermal buoyancy in single-sided ventilation is dependent on the height (and area) of the opening and of course the temperature difference between the in- and outside of the building.

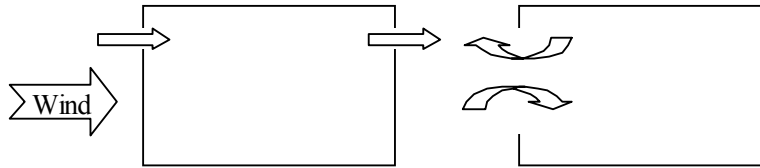


**Figure 1.1 Cross ventilation (left) and single sided ventilation (right).**

### Ventilation by thermal buoyancy alone

Thermal buoyancy is the effect of density differences due to different temperature levels. In order to determine airflows different zones of constant temperatures are defined and the pressure difference at height  $h$  can then be determined from a definition of the neutral plane (ASHRAE fundamentals, 1993) and the hydrostatic pressure distribution:

$$\begin{aligned} \Delta P &= (\rho_o - \rho_i) \cdot g \cdot (h - h_{npl}) \\ &\approx \frac{\rho_i \cdot (T_i - T_o) \cdot (h - h_{npl})}{T_o} \end{aligned} \quad (\text{Equation 1.1})$$

Where  $\rho_o$  and  $\rho_i$  are the outside and inside densities [ $\text{kg}/\text{m}^3$ ]

$H_{npl}$  is the height of the neutral plane [ $\text{m}$ ].

$T_i$  and  $T_o$  are the absolute indoor and outdoor temperatures respectively [ $^{\circ}\text{K}$ ].



In equation 0.1 the following approximated ratio between density and temperature is used:  $(\rho_o - \rho_i)/\rho_i \approx (T_i - T_o)/T_o$ .

In the single-sided ventilation case the neutral plane is placed in the vertical middle of the opening and the air will flow in through the bottom part and out through the upper part (assuming that the inside temperature is higher than the outside). When more than one opening is present the neutral plane can be located between the openings and the air will flow in through the openings placed below the neutral plane and out through those located above. The location of the neutral plane is dependent on the ratio of the opening areas (in- and outlets). If the neutral plane is placed in an opening the resulting flow will of cause be both in and outwards.

The airflow through an opening can then be determined from the pressure difference by:

$$q = C_D A \sqrt{\frac{2 \cdot \Delta P}{\rho}} = C_D A \sqrt{\frac{2 \cdot \Delta T \cdot g \cdot |h - h_{npl}|}{T}} \quad (\text{Equation 1.2})$$

Where  $C_D$  is the discharge coefficient [-]  
 $A$  is the area of the opening [ $m^2$ ]

It should be noted that this expression assumes that the neutral plane is placed outside the opening and hereby the airflow being unidirectional and the velocity distribution in the opening is constant. In the single-sided case the expression is of cause not applicable but using half the opening area and making an assumption of the velocity distribution in the opening being parabolic the expression can be adjusted (Andersen et al., 2002):

$$q = \frac{1}{3} C_D A \sqrt{\frac{\Delta T \cdot g \cdot h}{T}} \quad (\text{Equation 1.3})$$

### **Ventilation by wind alone**

In wind driven cross ventilation the airflow through an opening is determined by the surface pressures on the building generated by the wind. The design of wind driven ventilation is usually based on averaged surface

pressure coefficients for each building surface and an internal pressure determined from the opening areas and the surface pressure coefficients. The pressure coefficients describe the ratio of the local surface pressure and the dynamic pressure in the wind (found in the undisturbed wind in the height of the building):

$$C_p = \frac{P - P_0}{\frac{1}{2} \rho U_0^2} \quad (\text{Equation 1.4})$$

Where  $P$  is the local surface pressure [Pa]  
 $P_0$  is the reference pressure [Pa]  
 $U_0$  is the reference velocity [m/s]

The pressure coefficients can either be approximated by available tabular data or found by wind tunnel experiments or numerical predictions (Computational Fluid Dynamics).

From these pressure coefficients the airflow can be determined for a given opening (1) placed in a given surface:

$$q_1 = C_{D1} A_1 \sqrt{\frac{2 \cdot \Delta P_1}{\rho}} = C_{D1} A_1 U_0 \sqrt{|C_{P1} - C_{Pi}|} \quad (\text{Equation 1.5})$$

Where  $C_{Pi}$  is the internal pressure coefficient determined by a mass balance equation [-]

The discharge coefficient is usually assigned a value of 0.6 – 0.7. A value of 0.6 corresponds to the discharge coefficient of a sharp-edged orifice.

### **Ventilation by wind and thermal buoyancy**

As mentioned earlier the wind and thermal buoyancy forces are described in terms of pressure differences in order to obtain airflows through building envelope openings. When both wind and thermal buoyancy are present the pressure difference across a given opening is calculated from the pressure obtained from the effect of the wind added to the resulting pressure from the thermal buoyancy. Combining the expressions for the pressure differences for wind and buoyancy respectively for an opening  $j$  leads to:

$$\Delta P_j = \left( \underbrace{\frac{1}{2} \rho_u C_{p_j} v_{ref}^2}_{Wind} + \underbrace{\rho_u g (h_{npl} - h_j)}_{Buoyancy} \frac{\Delta T}{T} \right) - P_i \quad (Equation 1.6)$$

From this expression it is clear that combining the forces will either increase or decrease the total pressure difference across the opening.

A more detailed description of the calculation methods in natural ventilation can be found in the literature, see for example (Allard et al., 1998) or (Andersen et al., 2002) The mentioned literature also gives a good summation of important empirical results for different situations.

#### *1.1.2. OUTDOOR CLIMATE AND MICROCLIMATE*

The outdoor climate as well as the microclimate surrounding the observed building are factors that influence the natural ventilation and the design of it. The thermal buoyancy is driven by the temperature difference between the in- and outdoors and since the indoor temperature is approximately constant the outdoor temperature is decisive for the available driving pressure. In Denmark the temperatures used for design purposes are the Danish Design Reference Year which includes measured temperatures and wind data from representative months from a 15 year period (Andersen et al., 1982). Figure 1.2 shows the monthly mean outdoor temperatures and an indication of the variation during each month (10 % are above the indicated interval and 10 % are below).

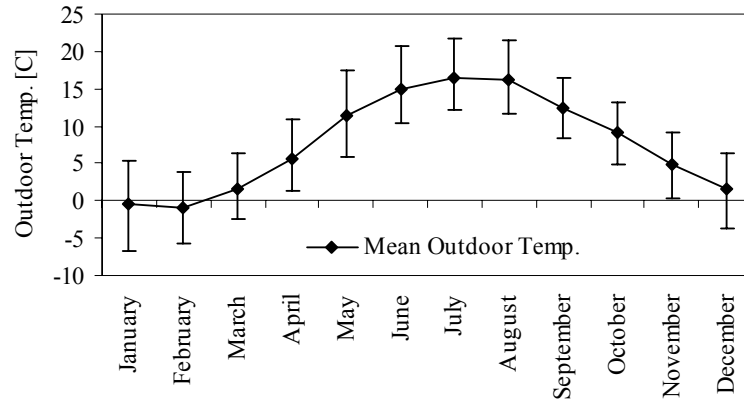


**Figure 1.2 Monthly mean outdoor temperatures with an indication of the variation during each month (10 and 90 % fractile)**

Comparing the temperatures shown in Figure 1.2 with an assumed indoor temperature of 20°C it is clear that the driving pressure for thermal buoyancy is highest in winter whereas it may be limited in the summer period.

In the same way as for the outdoor temperature the wind speed has been depicted in Figure 1.3.

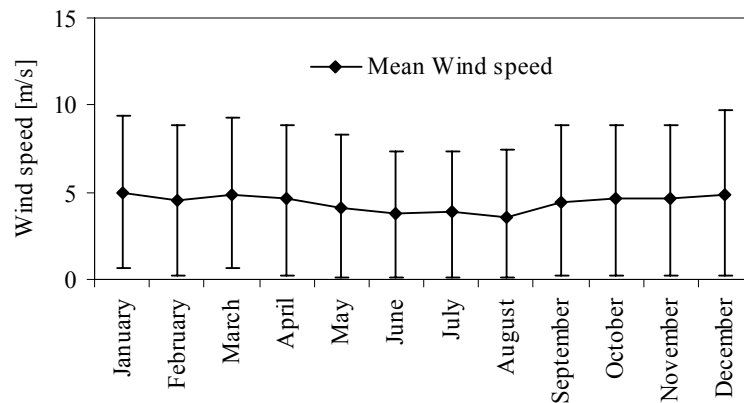


**Figure 1.3 Monthly mean wind speed with an indication of the variation during each month (10 and 90 % fractile).**

The wind has an almost constant mean value of 4 m/s and the variation is also similar for the different months. Obviously there are times when the driving force of the wind is close to 0 and the natural ventilation will have to rely on the thermal driving force. It should be mentioned that both figures are based on values from all hours of the year. If however only the hours between 6.00 - 18.00 were considered the lower limit would increase for both the temperature as well as the wind speed.

The surroundings of the building influence both the thermal driving force as well as the wind. The thermal driving force is influenced by the sun and the surroundings as well as the thermal properties of the surroundings. The wind can be influenced dramatically by surrounding buildings, vegetation and topology. Tabular data of wind pressure coefficients are normally based on cubic or rectangular shapes and either with or without surrounding standard shaped buildings, see (Orme et al., 1994). The pressure distribution on a specific building may vary too much from the standard cases and for the calculations to be accurate.

## **1.2. DESCRIPTION OF PROBLEM**

As mentioned earlier the design method of natural ventilation is based on converting the driving forces into pressure differences from which the airflow through openings are calculated. In the design of wind driven natural ventilation the average surface pressures of the sealed building are applied. Numerous studies concerning the pressure distribution on buildings have been carried out, an example with a wind incident angle of 0 degrees is shown in Figure 1.4 (Bjerregaard et al., 1980).

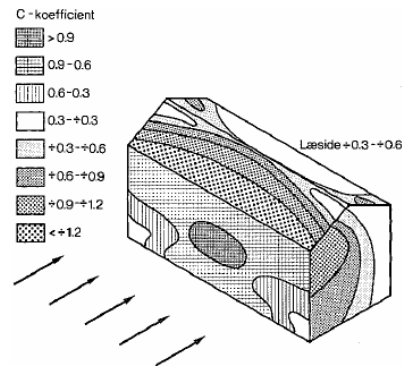


**Figure 1.4 Pressure distribution on wind exposed building. The wind incident angle is 0 degrees. (Bjerregaard et al., 1980)**

Figure 1.4 clearly shows that there can exist a large variation in the surface pressure on the building and that the location of openings in the building will be decisive for the available driving pressure. Therefore the determination of airflow rates based on the use of averaged values of pressure coefficients may be connected with discrepancies due to the large variation. At angled flows the variation of pressure on a given surface may also lead to a even larger deviance from the average value.

Another factor that may alter the pressure distribution is the varying wind direction which may occur in reality. (Jiang et al., 2002) has compared the distribution of the total driving pressure across a building for a wind direction of 45 degrees with the distribution for a variable wind direction from 0 to 90 degrees but with a mean of 45 degrees and has found an altered pressure distribution which is more even and higher than the steady case.

(Murakami et al., 1991) has emphasised that the fluid mechanics of air infiltration is completely different to that of cross ventilation. The difference lies in the dissipation of the jet entering the room. The jet from a crack is completely dissolved in the room and the pressure inside the room can be assumed to be uniform whereas the windward jet from a cross ventilation opening can transfer dynamic pressure to the outlet opening. This makes the earlier mentioned flow equation based on the Bernoulli

theorem inaccurate since it assumes that the air is transported between two pressure “basins” of constant pressure.

Models including the transfer of kinetic energy between openings have been suggested, see (Carrilho da Graca et al., 2002):

$$q_2 = C_D A_2 \sqrt{2 \left( P_{in} + \frac{1}{2} \rho \cdot v_L^2 \cdot \left( \frac{A_1}{A_2} \right)^{\frac{2}{3}} \right) - P_{out}} \quad (\text{Equation 1.7})$$

Where  $P_{in}$  and  $P_{out}$  are the pressures before and after the second opening [Pa].

$A_1$  and  $A_2$  are the opening areas of the up- and downstream openings respectively [m<sup>2</sup>]

$v_L$  is the velocity of the flow as it reaches the second opening [m/s].

(Murakami et al., 1991) described the flow between the openings in cross ventilation by the concept of a “virtual stream tube”. The idea of a stream tube has been analysed by (Karabuchi et al., 2002) not within the room but upstream of the building by computational fluid dynamics. Figure 1.5 shows an example of the obtained flow tubes with a wind direction of 67.5 degrees.

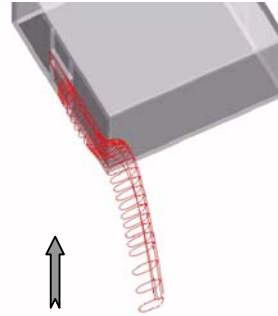


**Figure 1.5** Flow tube for the air going into the opening, with a wind direction of 67.5 degrees. (Karabuchi et al., 2002).

Another matter of interest is the fact that the flow equation is derived from a contraction in a confined flow which can be argued to be incomparable with the flow through a building opening which is either forced through the

opening or around the building. Figure 1.5 however shows that the flow to some extent is “confined” within a flow tube.

### 1.3. SCOPE OF WORK

A problem encountered in the design of natural ventilation deals with the determination of the airflow rate through openings. This is in sharp contrast to mechanical ventilation where a fan delivers a certain airflow rate at a given pressure loss through the ventilation system. Of course the natural forces of wind and thermal buoyancy can also affect a mechanical ventilation system but the influence is insignificant due to much higher pressure losses in the system from filters and other components.

The airflow rate in wind driven natural ventilation is dependent on a large number of variables. Considering a building with the layout shown in Figure 1.6 where  $U_0$  is the reference velocity,  $\beta$  is the wind direction and  $\Delta P$  is the pressure difference across the building envelope where the openings are placed.

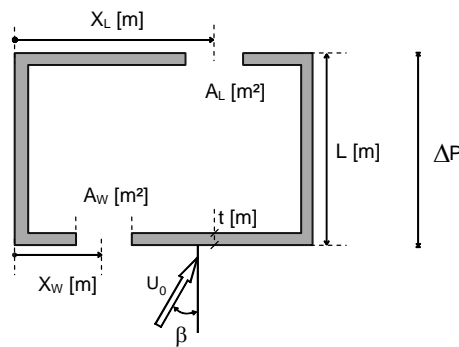


**Figure 1.6 Important parameters in the determination of airflow through a building.**

The wind induced pressure distribution on the building and hereby the driving pressure for the airflow through the openings will in addition to



being dependent on the surroundings also be dependent on the shape of the building. Placing an opening in the building may influence the pressure distribution and whether the pressure distribution obtained from the sealed building can be used to predict the airflow through openings placed in the same building is one of the questions that are examined in the present thesis.

In addition to the building structure being decisive for the pressure distribution the airflow rate is also dependent on the internal structure of the building as well as the location, size and geometry of the openings. The location and the size are important both in regards to the building as well as compared to the other openings. If equation 1.5 is considered the pressure difference across an opening contains the internal pressure in the building which in the design of natural ventilation is assumed to be in a state of static equilibrium and the internal airflow is disregarded this may lead to discrepancies due to the possibility of “flow contact” between the openings. This “flow contact” can be physically described as the transfer of kinetic energy between openings.

The location of the openings in the building has an indirect influence on the airflow rate due to the variation of the pressure distribution across the building surface. The common design procedure today does not account for the location of the openings but utilises averaged surface pressure coefficients in the determination of the airflow rate.

In the thesis the influence of these factors are investigated by a combination of theoretical, experimental and numerical considerations.

## 2. FLUID FLOW

A fluid can be defined as a substance that deforms when subjected to shear stresses. In order for shear stresses to exist the fluid must be viscous, which is the case for all real fluids. However an ideal fluid may be defined as nonviscous (or inviscid) and therefore no shear stresses can exist in the flow.

A force acting on a fluid causes the fluid to flow. Fluids can be divided into liquids, which are usually considered incompressible, and gasses, which can be considered compressible. A fluid is considered incompressible if the change in density is small compared to the initial density ( $\Delta\rho/\rho_0 \ll 1$ ). Gasses in isothermal flow are however usually considered incompressible if the dynamic pressure is small compared to the atmospheric pressure, and usually gaseous flow is considered incompressible if the velocity of the flow is less than 100 m/s (Schlichting, 1979). This is always the case in airflow in and around buildings.

The study of fluid flow is based upon some fundamental laws: conservation of mass, momentum and energy. These equations contain properties that are specific and decisive for the considered fluid flow: density, viscosity, compressibility and thermal properties.

### 2.1. TYPES OF FLOW

A fluid in motion consists of a large number of molecules moving in the general direction of the flow. The velocity of a particle can be considered a vector quantity and varies from moment to moment and the path a particle follows is called a streamline.

In a laminar flow the fluid is moving in an orderly fashion and in parallel lines, see Figure 2.1.

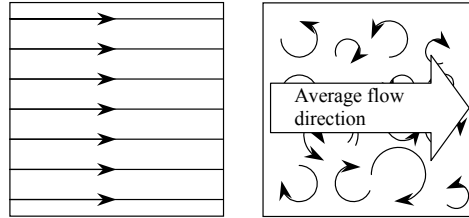


**Figure 2.1** In the laminar flow the fluid moves in an orderly fashion in parallel lines. The turbulent case is on the other hand characterised by a chaotic behaviour consisting of different size vortices that change in both time and space, but still containing a dominant flow direction.

The turbulent flow is oppositely characterised by a chaotic behaviour where the particles are moving in different directions and at different velocities. In the turbulent flow both the direction as well as the velocity may change in both time and space.

In a free laminar flow, i.e. in a large distance from any obstacles, the particle velocity is equal in both magnitude and direction. In the vicinity of an obstacle the streamlines are distorted and the velocity is no longer constant in neither the flow direction nor parallel to the flow direction. Due to the viscosity of the fluid, frictional forces are introduced between the layers just as it is the case in the vicinity of the obstacle where the velocity is reduced to 0.

The proportionality factor between the shear stress and the velocity gradient is called the dynamic viscosity (Schlichting, 1979):

$$\tau = \mu \cdot \frac{du}{dy} \quad (\text{Equation 2.1})$$

Where  $\tau$  is the shearing stress (Pa)  
 $\mu$  is the dynamic viscosity (kg/m-s)

The above equation is known as *Newton's law of friction* and the value of  $\mu$  is dependent on the fluid and the temperature.

The velocity increase from the surface of the obstacle to the velocity in the free flow happens through a layer called the *boundary layer*, where the velocity gradient ( $du/dy$ ) is large.

A common example of the development of boundary layers is Prandtl's motion along a flat plate (Prandtl, 1904).

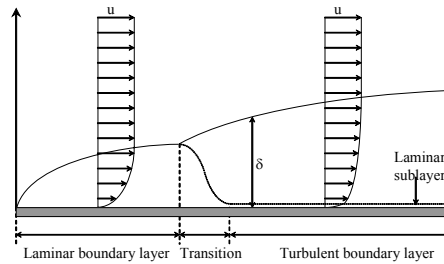


**Figure 2.2 Flow over a flat plate with velocity profiles in the laminar and turbulent boundary layer.**

The transition from laminar to turbulent flow happens a certain distance from the starting point of the flat plate. This distance can be determined by the velocity, the viscosity and the density of the fluid. These factors can be combined in the dimensionless number called the Reynolds number, which is defined by:

$$Re = \frac{\rho \cdot u \cdot l}{\mu} \quad (\text{Equation 2.2})$$

Where  $\rho$  is the density of the fluid ( $\text{kg/m}^3$ )  
 $u$  is the free stream velocity ( $\text{m/s}$ )  
 $l$  is the distance to the transition ( $\text{m}$ )

The Reynolds number is an important parameter in the determination of the transition from laminar to turbulent flow. The transitional Reynolds number is usually referred to as the critical Reynolds number, and has a value of  $Re_{\text{crit}} \approx 50000$  for the flow over a flat plate (Schlichting, 1979), and  $Re_{\text{crit}} \approx 2500$  for pipeflow and a similar value for windows and openings (Jensen True & Larsen, 2000).

Since the flow in the turbulent region consists of diverse movements of the particles both in time and space, a way of regarding the problem is that of

statistics. The instantaneous velocity can be written as a velocity fluctuation ( $u'$ ) added to the mean velocity ( $u$ ):

$$\hat{u}_i = u_i + u'_i \quad (\text{Equation 2.3})$$

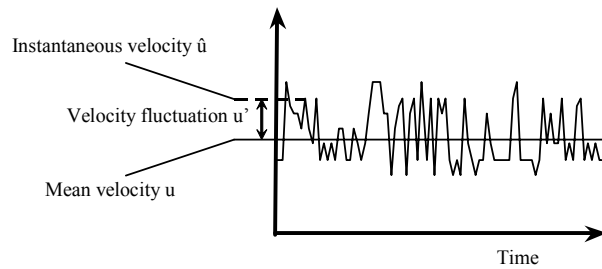


**Figure 2.3 Velocity fluctuations in turbulent flow.**

A graphical depiction of the definition is shown in Figure 2.3, where the velocity for a point in space has been depicted.

The turbulence intensity can be used as a measure of turbulence. The turbulence intensity is defined by the standard deviation of the velocity fluctuations divided by the mean velocity:

$$TI = \frac{\sqrt{u'^2}}{u} \quad (\text{Equation 2.4})$$

### 2.1.1. FLOW SEPARATION

When a flow is parallel to an obstacle the pressure in the boundary layer is only decreasing slightly, and the flow follows the plate for all its length. If the plate on the other hand is placed at an angle compared to the flow, the flow will accelerate from the stagnation point towards the sides, see Figure 2.4. The maximum point is located in the stagnation point and decreases towards the sides. Behind the plate the air movement is very turbulent and the static pressure always lower than in the free stream.

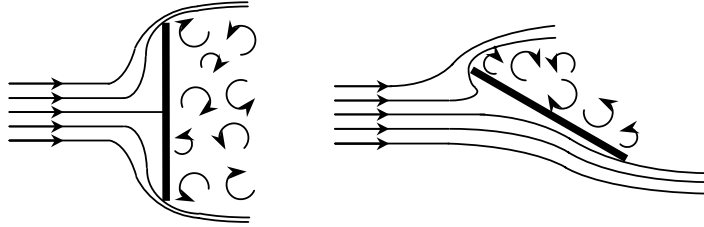


**Figure 2.4 Separation of flow induced by obstacle placed perpendicular to and at an angle compared to the flow direction.**

## 2.2. GOVERNING FLOW EQUATIONS

Fluid dynamics can be described as the study of transport of mass, momentum and energy. Transport can be caused by fluid motion in the direction of the flow (convection) or by diffusion and/or conduction in any direction.

The governing flow equations can be summed up in three basic laws:

1. *Conservation of mass*
2. *Conservation of momentum*
3. *Conservation of energy*

### 2.2.1. CONSERVATION OF MASS

The equation of conservation of mass or the continuity equation is derived from the principle that: the mass flow into an infinitesimal volume is equal to the mass flow out of the same volume. No mass is destroyed or created in the flow through the volume.

The continuity equation can be written as (instantaneous values):

$$\frac{\partial \rho}{\partial t} + \frac{\partial(\rho \hat{u})}{\partial x} + \frac{\partial(\rho \hat{v})}{\partial y} + \frac{\partial(\rho \hat{w})}{\partial z} = 0 \quad (\text{Equation 2.5})$$

Since equation 1.5 is defined by instantaneous values, equation 1.3 is applied and each part is averaged:

$$\frac{\partial u}{\partial x} + \frac{\partial v}{\partial y} + \frac{\partial w}{\partial z} = 0 \quad (\text{Equation 2.6})$$

The densities has been removed since the flow is assumed to be incompressible and the fluctuations are removed since the average value of the fluctuations is 0.

### 2.2.2. CONSERVATION OF MOMENTUM

Momentum is the product of mass and velocity, it is therefore obvious that momentum can be transported by convection, but momentum can also be transported by the action of viscosity or turbulence. The transport of momentum can, in Cartesian co-ordinates, happen in each of the three directions, x, y and z.

The equations of conservation of momentum or Navier-Stokes' equations, as they are usually referred to, are derived with a starting point in Newton's

2. Law:  $F = m \cdot a$ .

The forces acting on the volume can be divided into two parts:

1. Forces acting on the volume itself, i.e. thermal forces. ( $F_{i,\text{volume}}$ )
2. Forces acting on the surfaces of the volume, i.e. pressure and shear forces. ( $F_{i,\text{surface}}$ )

From this the Navier-Stokes equations can be written (for the y-direction, e.g. the direction of gravity):

$$\hat{\rho} \cdot \frac{D\hat{v}}{Dt} = \hat{\rho} \cdot g + \frac{\partial \hat{\tau}_{yy}}{\partial y} + \frac{\partial \hat{\tau}_{xy}}{\partial x} + \frac{\partial \hat{\tau}_{yz}}{\partial z} \quad (\text{Equation 2.7})$$

The stresses ( $\tau$ ) in equation 1.7 can be replaced by Stokes law of friction, which is a generalised version of the Newton law of friction, see equation 1.1:

$$\hat{\tau}_{ij} = -\hat{p} \cdot \delta_{ij} + \mu \left( \frac{\partial \hat{u}_i}{\partial x_j} + \frac{\partial \hat{u}_j}{\partial x_i} \right) \quad (\text{Equation 2.8})$$

Equation 1.8 applies to an incompressible fluid and expresses that the stress-tensor is proportional to the velocity gradients and that the deformation is caused by the hydrostatic pressure when the velocity gradients are equal to 0.

The earlier mentioned proportionality factor between the stress and the velocity gradient is called the dynamic viscosity ( $\mu$ ) and expresses the exchange of momentum between molecules.

Combining equations 1.7 and 1.8 yields:

$$\begin{aligned} \hat{\rho} \left( \frac{\partial \hat{v}}{\partial t} + \hat{u} \frac{\partial \hat{v}}{\partial x} + \hat{v} \frac{\partial \hat{v}}{\partial y} + \hat{w} \frac{\partial \hat{v}}{\partial z} \right) = \\ \hat{\rho} g - \frac{\partial \hat{p}}{\partial y} + 2\mu \frac{\partial^2 \hat{v}}{\partial y^2} \\ + \mu \left( \frac{\partial^2 \hat{v}}{\partial x^2} + \frac{\partial^2 \hat{u}}{\partial x \partial y} \right) + \mu \left( \frac{\partial^2 \hat{v}}{\partial z^2} + \frac{\partial^2 \hat{w}}{\partial y \partial z} \right) \end{aligned} \quad (\text{Equation 2.9})$$

Applying the continuity equation (equation 1.6) this leads to:

$$\begin{aligned} \hat{\rho} \left( \frac{\partial \hat{v}}{\partial t} + \hat{u} \cdot \frac{\partial \hat{v}}{\partial x} + \hat{v} \cdot \frac{\partial \hat{v}}{\partial y} + \hat{w} \cdot \frac{\partial \hat{v}}{\partial z} \right) = \\ \hat{\rho} g - \frac{\partial \hat{p}}{\partial y} + \mu \cdot \left( \frac{\partial^2 \hat{v}}{\partial x^2} + \frac{\partial^2 \hat{v}}{\partial y^2} + \frac{\partial^2 \hat{v}}{\partial z^2} \right) \end{aligned} \quad (\text{Equation 2.10})$$

The instantaneous density is a function of the instantaneous temperature, this is however ignored except for the part including  $g_i$  which is substituted by Boussinesqs' approximation:

$$\hat{\rho} \cdot g = -\rho_0 \cdot \beta \cdot g \cdot (\hat{T} - T_0) \quad (\text{Equation 2.11})$$

Applying this as well as equation 1.3 and taken the mean value equation 1.10 becomes:



$$\begin{aligned}
 & \rho_0 \cdot \left( \frac{\partial v}{\partial t} + u \cdot \frac{\partial v}{\partial x} + v \cdot \frac{\partial v}{\partial y} + w \cdot \frac{\partial v}{\partial z} \right) = \\
 & - \rho_0 \cdot \beta \cdot g \cdot (T - T_0) - \frac{\partial p}{\partial x} \\
 & + \mu \cdot \left( \frac{\partial^2 v}{\partial x^2} + \frac{\partial^2 v}{\partial y^2} + \frac{\partial^2 v}{\partial z^2} \right) \\
 & - \rho_0 \cdot \left( \frac{\partial \overline{v'^2}}{\partial y} + \frac{\partial \overline{u' \cdot v'}}{\partial x} + \frac{\partial \overline{v' \cdot w'}}{\partial z} \right)
 \end{aligned}
 \tag{Equation 2.12}$$

The terms containing fluctuations are called Reynolds stresses and are the effects of turbulent transport, and acts as a stress on the fluid, hence the name (Rodi, 1984).

The Reynolds stresses can be replaced by Boussinesq's description of the turbulent viscosity:

$$- \overline{u'_j \cdot u'_i} = \frac{\mu_t}{\rho} \cdot \left( \frac{\partial u_i}{\partial x_j} + \frac{\partial u_j}{\partial x_i} \right) - \frac{2}{3} \cdot k \cdot \delta_{ij}
 \tag{Equation 2.13}$$

Where  $\delta_{ij}$  is the Kronecker delta (-)

$\mu_t$  is the turbulent viscosity (kg/m·s)

$k$  is the turbulent kinetic energy, defined by:

$$k = \frac{1}{2} \cdot \left( \overline{u'^2} + \overline{v'^2} + \overline{w'^2} \right)
 \tag{Equation 2.14}$$

$\mu_t$  (in equation 1.13) is called the turbulent viscosity, but is not a viscosity as described in equation 1.1, but effects the flow in the same way.

Placing Boussinesq's description of the turbulent viscosity (1.13) in 1.12 the following expression is obtained:

$$\begin{aligned}
 & \rho \cdot \left( \frac{\partial v}{\partial t} + u \cdot \frac{\partial v}{\partial x} + v \cdot \frac{\partial v}{\partial y} + w \cdot \frac{\partial v}{\partial z} \right) = \\
 & -\rho \cdot \beta \cdot g \cdot (T - T_0) - \frac{\partial p}{\partial y} \\
 & + 2 \cdot \frac{\partial}{\partial y} \left( (\mu + \mu_t) \cdot \frac{\partial v}{\partial y} \right) \\
 & + \frac{\partial}{\partial y} \left( (\mu + \mu_t) \cdot \left( \frac{\partial v}{\partial x} + \frac{\partial u}{\partial y} \right) \right) \\
 & + \frac{\partial}{\partial z} \left( (\mu + \mu_t) \cdot \left( \frac{\partial w}{\partial y} + \frac{\partial v}{\partial z} \right) \right)
 \end{aligned} \tag{Equation 2.15}$$

If  $\mu$  and  $\mu_t$  are assumed constant and by applying the continuity (equation 1.6) equation 1.15 can be reduced to:

$$\begin{aligned}
 & \rho \cdot \left( \frac{\partial v}{\partial t} + u \cdot \frac{\partial v}{\partial x} + v \cdot \frac{\partial v}{\partial y} + w \cdot \frac{\partial v}{\partial z} \right) = \\
 & -\rho \cdot \beta \cdot g \cdot (T - T_0) - \frac{\partial p}{\partial x} \\
 & + \mu_{eff} \cdot \left( \frac{\partial^2 v}{\partial x^2} + \frac{\partial^2 v}{\partial y^2} + \frac{\partial^2 v}{\partial z^2} \right)
 \end{aligned} \tag{Equation 2.16}$$

where  $\mu_{eff}$  is the "effective" viscosity constructed from adding the two viscosities.

This expression applies to the y-direction and similar expressions can be found for the x- and z-directions.

### 2.2.3. CONSERVATION OF ENERGY

The energy equation is derived in the same way as for the continuity equation from an infinitesimal volume, and from the first law of thermodynamics which says that the increase in energy in the volume is equal to the work carried out upon the volume plus the applied heat.

The energy equation can be written as:

$$\begin{aligned} & \rho \cdot c_p \cdot \left( \frac{\partial \hat{T}u}{\partial x} + \frac{\partial \hat{T}v}{\partial y} + \frac{\partial \hat{T}w}{\partial z} \right) \\ & = \lambda \cdot \left( \frac{\partial^2 \hat{T}}{\partial x^2} + \frac{\partial^2 \hat{T}}{\partial y^2} + \frac{\partial^2 \hat{T}}{\partial z^2} \right) \end{aligned} \quad (\text{Equation 2.17})$$

In the same way as previously the instantaneous values are replaced by the mean value plus a fluctuation, which leads to:

$$\begin{aligned} & \rho \cdot c_p \cdot \left( \frac{\partial Tu}{\partial x} + \frac{\partial Tv}{\partial y} + \frac{\partial Tw}{\partial z} \right. \\ & \quad \left. + \frac{\partial T' u'}{\partial x} + \frac{\partial T' v'}{\partial y} + \frac{\partial T' w'}{\partial z} \right) = \\ & \lambda \cdot \left( \frac{\partial^2 T}{\partial x^2} + \frac{\partial^2 T}{\partial y^2} + \frac{\partial^2 T}{\partial z^2} \right) \end{aligned} \quad (\text{Equation 2.18})$$

The terms including fluctuations are called turbulent heat fluxes, and these can be replaced by Boussinesq's description of turbulent heat transport:

$$-\overline{u'_i T'} = \frac{\mu_t}{\rho \cdot \sigma_h} \cdot \frac{\partial T}{\partial x_i} \quad (\text{Equation 2.19})$$

where  $\sigma_h$  is the turbulent Prandtl number (-).

Applying this to equation 1.18 yields:

$$\begin{aligned} & \rho \cdot c_p \cdot \left( \frac{\partial Tu}{\partial x} + \frac{\partial Tv}{\partial y} + \frac{\partial Tw}{\partial z} \right) = \\ & \left( \lambda + \frac{c_p \cdot \mu_t}{\sigma_h} \right) \cdot \left( \frac{\partial^2 T}{\partial x^2} + \frac{\partial^2 T}{\partial y^2} + \frac{\partial^2 T}{\partial z^2} \right) \end{aligned} \quad (\text{Equation 2.20})$$

### 2.3. JET FLOW THEORY

When air enters a room it forms a jet which due to entrainment will experience a velocity decay and an expansion. If the jet is placed close to a wall or the ceiling the jet will form a *wall jet* and if the jet is placed more freely it will form a *free jet*, see Figure 2.5. The velocity decay and the expansion of the jet has a large influence on the airflow in cross ventilated rooms since the use of the flow equation in natural ventilation is based upon a completely dissolved jet and hereby no flow contact between the openings. Flow contact between openings has been observed in several cross flow investigations (Carrilho de Graca et al., 2002, Jensen True et al. 2003, Jiang et al., 2003).

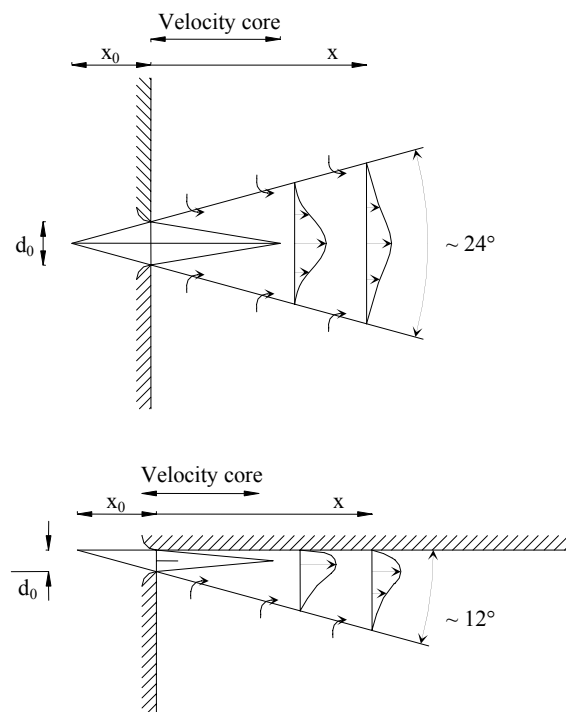


**Figure 2.5** Schematic outline of the flow from a free jet and a wall jet respectively.

A 2D free jet can have a constant velocity core which is up to 6 times the diameter of the opening and a 2D wall jet can have a constant velocity core which is up to  $12 \cdot h_0$ . The growth angle of the jet is approximately  $24^\circ$  for a circular jet and  $33^\circ$  for a plane free jet, in the wall jet case the growth angle will be approximately half these values.

The factor  $x_0$  shown in Figure 2.5 is the virtual origin of the jet which is the “source” point of the jet.

In theory the free jet is assumed to flow into an infinitely large space, whereas the wall jet flows along a surface and with no other constrictions. Using these assumptions and applying preservation of momentum it is possible to deduce formulas for the centreline velocity decay of the jet (or in the case of a wall jet the decay of the maximum velocity). The characteristic behaviour of a turbulent free jet can be described by (Rajaratnam, 1976):

$$(2D) \quad \frac{u_x}{u_0} = \frac{K_p}{\sqrt{2}} \sqrt{\frac{h_0}{x+x_0}} \quad (\text{Equation 2.21})$$

$$(3D) \quad \frac{u_x}{u_0} = \frac{K_a}{\sqrt{2}} \frac{\sqrt{a_0}}{x+x_0} \quad (\text{Equation 2.22})$$

The flow in a 3-dimensional turbulent wall jet with area ( $a_0$ ) is identical to the flow in a 3-dimensional free jet with twice the area ( $2 \cdot a_0$ ) and in the 2-dimensional case twice the height ( $h_0$ ). Therefore the velocity decay in case of a wall jet can be described by ( $a_0$  is simply replaced by  $2 \cdot a_0$ ):

$$(2D) \quad \frac{u_x}{u_0} = K_p \sqrt{\frac{h_0}{x+x_0}} \quad (\text{Equation 2.23})$$

$$(3D) \quad \frac{u_x}{u_0} = K_a \frac{\sqrt{a_0}}{x + x_0} \quad (\text{Equation 2.24})$$

The parameters  $K_p$  and  $K_a$  are characteristic constants dependent on the geometry of the opening. These characteristic values are Reynolds number dependent, but are constant at fully turbulent flow. Values of  $K_a$  and  $K_p$  are well-defined for commercial openings used in mechanical ventilation. Values for different air terminal devices can be found in (ASHRAE Fundamentals, 1993).

The equations 1.21 to 1.24 are based on ideal jets where momentum is preserved, for real jets there is a loss in momentum in the opening and for wall jets there is also a loss due to friction from the wall. The effect of the wall friction on the velocity decay can result in a changed distance proportionality exponent. The proportionality exponents in equations 1.23 and 1.24 are -0.5 and -1 respectively. A momentum loss will lower these values, different exponents based on measurements are given in (Schwarz and Cosart, 1960) (-0.555, plane wall jet), (Bakke, 1957) (-1.12, radial wall jet), (Waschke, 1974) (-1.15, radial wall jet) and (Sforza and Herbst, 1970) (-1.14, square wall jet).

The thickness of the jet ( $\delta$ ) is linearly proportional to the distance to the opening (virtual origin), and can therefore be described by:

$$(2D) \quad \delta = D \cdot (x + x_0) \quad (\text{Equation 2.25})$$

The thickness of the jet ( $\delta$ ) is defined as the distance from the centreline or the wall to the location where the velocity is half the maximum jet velocity ( $0.5 \cdot u_x$ ).

The undisturbed isothermal free jet can be shown to have self similar profiles or universiel profiles described by (Rajaratnam, 1976):

$$\frac{u(y)}{u_x} = \exp(-0.693 \cdot (y/\delta)^2) \quad (\text{Equation 2.26})$$

The corresponding profile for a wall jet is described by (Verhoff, 1963):

$$\frac{u(y)}{u_x} = 1.48 \cdot (y/\delta)^{1/7} (1 - \text{erf}(0.68 \cdot y/\delta)) \quad (\text{Equation 2.27})$$

Where *erf* is the error function.

### 2.3.1. MEASUREMENTS OF AIRFLOW FROM BOTTOM HUNG WINDOWS USED FOR NATURAL VENTILATION

At Aalborg University research have been carried out regarding airflow characteristics for windows, see (Heiselberg et al., 1999, 2000, 2001), (Svidt et al., 2000), (Jensen and Larsen, 2000) and (Bjørn et al., 2001). This research has resulted in the characterisation of airflow from both bottom- and sidehung windows, and also stratified flow as well as isothermal flow. Characteristic values for windows used in natural ventilation can be found in the above mentioned references. The following is an analysis of the isothermal measurements which can be found in references (Jensen and Larsen, 2000), (Bjørn et al. 2001) and (Heiselberg et al. 2001).

Figure 2.6 shows the window section where the measurements were carried out, the top depiction shows a sketch of the location in the wall and the smaller photos below shows one of the button-hung windows. The measurements were conducted in a full-scale test room at Aalborg University, the room was divided into two sections; one simulating outdoor conditions and the other the office room under investigation. The window section shown in Figure 2.6 was placed between the two sections.

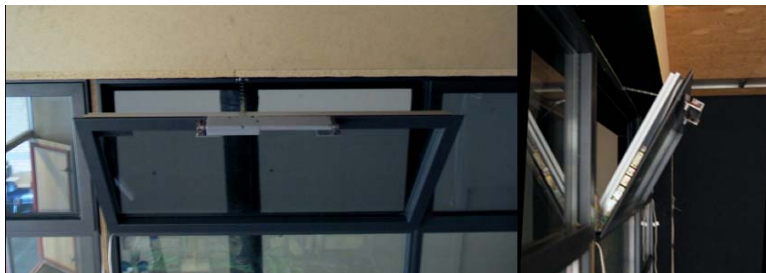
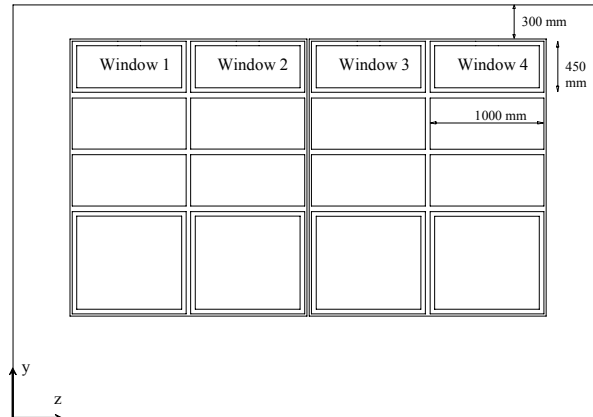


**Figure 2.6** The windows used in the analysis.

The bottom-hung windows were placed at the top of the window frame and the distance from the frame to the ceiling was 300 mm, therefore the airflow from the windows were influenced by the Coanda effect and formed a wall jet at a distance from the facade.

Two different flow situations has been observed, these are shown in the following Figure 2.7. The first flow situation is where the top-edge of the window has not exceeded the window frame, here the flow will form a free-jet which eventually will turn into a wall-jet because of the relatively small distance to the ceiling. The second flow situation is where the edge of the window exceeds the window frame, here the initial jet is directed towards the ceiling and the wall-jet is established very close to the facade.



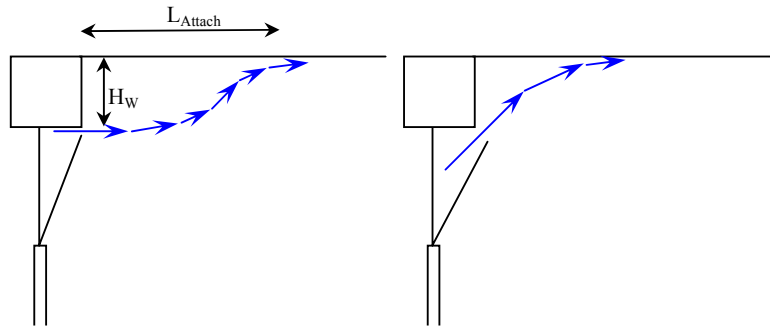


**Figure 2.7** The jet formed from the window is dependent on the opening angle.

The distance from the backwall to the place where the jet attaches to the ceiling varies dependent on the window configuration. The following table shows the observed distances from the wall to where the wall-jet is formed based on velocity profile measurements. The values shown in the Table 2.1 only covers the situation where the top of the window does not exceed the edge of the window frame. The difference in the values for windows 1 and 2 is due to window 1 is placed close up against the frame of the window to the one side. This effects the airflow because an angled jet is created at each side of the window which is limited to the one side when window 1 is open. When all four windows are open this effect is completely removed.

Configuration	Window 1	Window 2	Windows 1-4
$L_{attach}$	1,6 – 2,0 m	1,2 – 1,9 m	1,0 – 1,3 m
$L_{attach}/H_{WF}$	5 – 7	4 – 6	3 – 4

**Table 2.1** Distance to the attachment point

Five different opening areas have been used for the configurations using only window 1 and 2 respectively. Figure 2.8 shows the measured velocity profiles when only window 2 (see Figure 2.6) is open and with an opening area of 0.119 m<sup>2</sup> corresponding to the point where the top of the window is in line with the edge of the window frame.

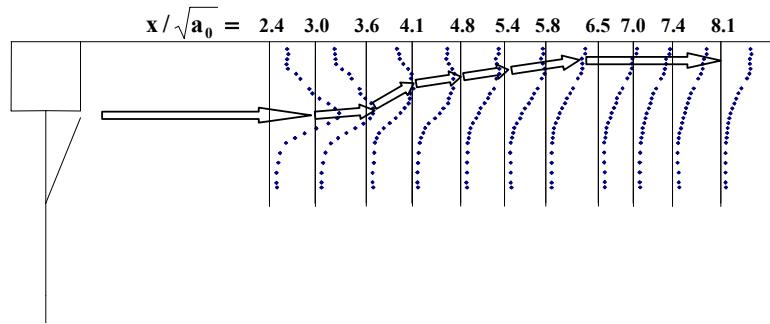


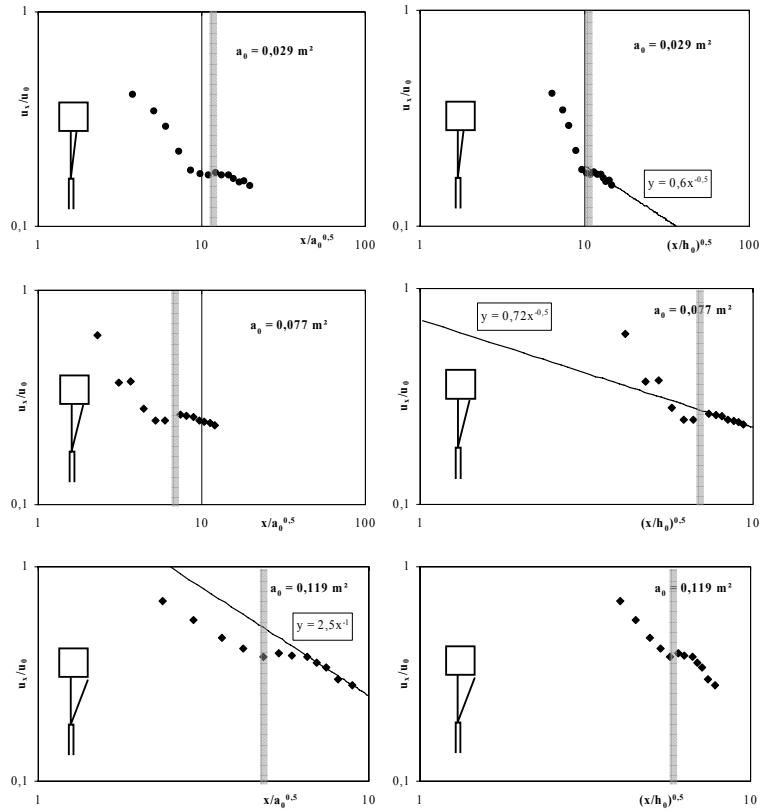
**Figure 2.8 Measured velocity profiles and the approximate direction of the main flow.**

The depictions below shows the velocity decay as a function of the relative distance and the distance squared for measurements where only window 2 is open. The thick line added in the depictions is the approximate point of where the jet attaches to the ceiling. The small sketch to the left in the depictions shows the approximate opening angle of the window.

Since no measurements of the inlet velocity were conducted the following is based on the geometrical opening area and not the effective area of the opening. The distance to the “virtual origin” ( $x_0$ ) in the jet flow equations has been disregarded since they have a tendency to assume diverse values and because they affect the magnitude of the characteristic constants (K-values) these will not be immediately comparable.

The first part of the jet has the characteristics of a 3-dimensional free jet, however for the measured part of the domain this is a “development” region in which the jet is turned towards the ceiling. The velocity decay for the 2 smaller opening areas show the characteristics of a 2-dimensional wall-jet after the jet attaches to the ceiling it is however expected that a 3-dimensional wall jet would form further away from the window. The smaller openings were expected also to form a 2 dimensional free jet before reaching the ceiling, but due to the large opening areas in the sides of the window (see Figure 2.6) momentum is dragged out of the “main” jet which affects the airflow.

For the opening areas of 0,119 m<sup>2</sup> and 0,172 m<sup>2</sup> the wall-jet is transformed into a 3-dimensional wall-jet after a short 2-dimensional phase. The largest opening size shows the approximate characteristics of a 3-dimensional wall-jet for the whole measured domain.



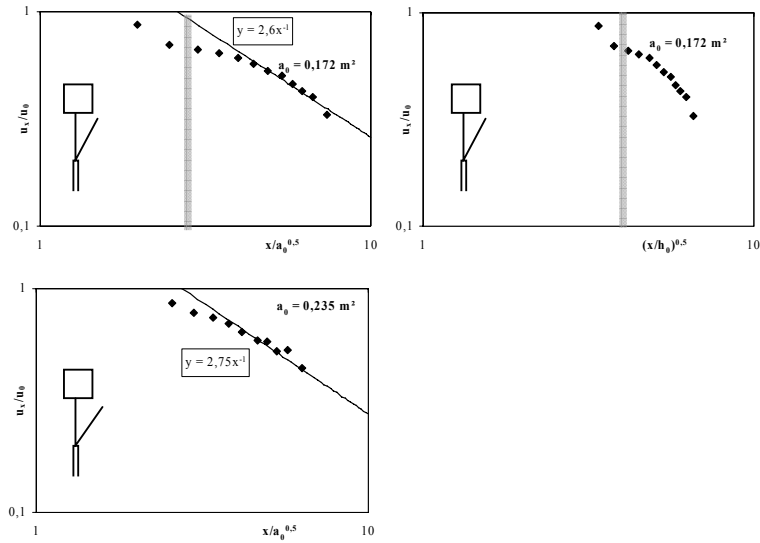


**Figure 2.9 Measured velocity decay for window 2 at different opening areas.**

The obtained characteristic constants from the measurements are shown in Table 2.2.

Opening area	0.029	0.077	0.119	0.172	0.235
2D wall-jet	0.6	0.72	-	-	-
3D wall-jet	-	-	2.5	2.6	2.75

**Table 2.2 Characteristic values divided into the different jet types that occur for the five opening areas.**

There is a small increase in the K-values which corresponds to the decreasing influence of the angled jets formed at the two sides of the window which drag out less momentum from the main jet.

## 2.4. MEASUREMENT OF AIRFLOW

A common way of measuring the airflow in pipes or ducts is by the use of pressure measuring devices such as pressure tube anemometers, orifices,

nozzles or Venturi tubes (see Ower and Panckhurst, 1977). In all of these the airflow is found from a loss coefficient and the pressure, based on the Bernoulli equation.

When predicting airflow rates in natural ventilation a characteristic flow coefficient called the discharge coefficient ( $C_D$ ) is used for each opening. The value of this coefficient is usually assumed to have a magnitude of about 0.6, which corresponds to the contraction coefficient found from a sharp edged orifice in pipe flow.

#### 2.4.1. THE BERNOULLI EQUATION

The Bernoulli equation is named after D. Bernoulli who stated the theorem in 1738 (Ower and Panckhurst 1977). The theorem is derived by the conception of streamlines and is based on the flow of an inviscid fluid.

The Bernoulli equation can be derived by considering a small element between two streamlines, and equating the total forces acting on the element with the change of momentum per second. By integration this leads to (again the density is assumed to be constant):

$$\frac{v^2}{2} + g \cdot h + \frac{p}{\rho} = \text{constant} \quad (\text{Equation 2.28})$$

This expression applies to all sections of a given stream-tube. When the stream-tube becomes infinitely narrow it may be considered as forming a streamline and therefore equation 1.28 gives the relation between pressure and velocity along a streamline.

The quantity  $h$  may be taken as the height to any arbitrary point of reference. Therefore when the flow is horizontal  $h$  becomes 0 and equation 1.28 becomes:

$$\frac{1}{2} \cdot \rho \cdot v^2 + p = \text{constant} \quad (\text{Equation 2.29})$$

This is the Bernoulli equation in the most commonly used form.

### 2.4.2. FLOW THROUGH A CONSTRICTION

Considering a flow in a pipe with a constriction, with  $a_1$  denoting the cross sectional area of the non-constricted part and  $a_2$  denoting the cross sectional area of the constricted end of the pipe, see Figure 2.10.

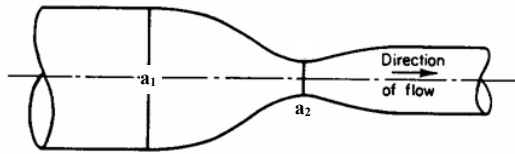


**Figure 2.10** Flow through a constriction (Ower and Panckhurst, 1977)

If the Bernoulli equation is applied to a streamline in the flow, the following can be obtained:

$$\frac{1}{2} \cdot \rho \cdot (v_2^2 - v_1^2) = p_1 - p_2 \quad (\text{Equation 2.30})$$

In addition to this expression the mass flowing through  $a_1$  has to be equal to the mass flowing through  $a_2$ .

$$a_1 \cdot v_1 = a_2 \cdot v_2 \quad (\text{Equation 2.31})$$

Substituting  $v_1$  in equation 1.30 with  $v_1$  from equation 1.31:

$$v_2^2 = \frac{2 \cdot (p_1 - p_2)}{\rho \cdot (1 - (a_2/a_1)^2)}$$

Now the theoretical flow rate is obtainable by:

$$q_{\text{Theo}} = a_2 \cdot v_2 = a_2 \sqrt{\frac{2 \cdot (p_1 - p_2)}{\rho \cdot (1 - (a_2/a_1)^2)}} \quad (\text{Equation 2.32})$$

### 2.4.3. THE SHARP EDGED ORIFICE

When deriving the airflow rate dispersed from a sharp edged orifice the only difference from equation 1.32 is the area of the constriction ( $a_2$ ). The contracted area (*the vena contracta*) substitutes the area of the constriction and the equation becomes:

$$q_{Theo.orifice} = C_c a_2 \sqrt{\frac{2 \cdot (p_1 - p_2)}{\rho \cdot (1 - C_c^2 (a_2/a_1)^2)}} \quad (Equation 2.33)$$

The coefficient  $C_c$  is the loss coefficient due to the contraction of the flow, see Figure 2.11.

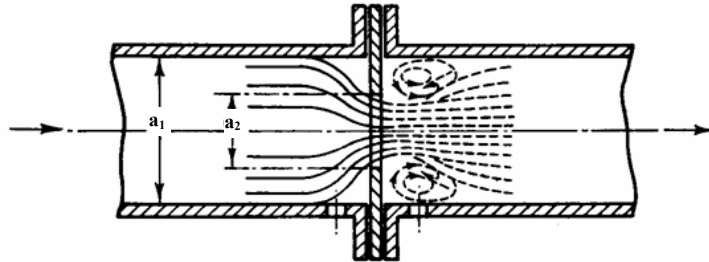


Figure 2.11 Flow through an orifice, (Ower and Panckhurst, 1977).

Since equation 1.33 applies to the ideal flow it does not account for frictional and turbulent losses, therefore a factor  $C_f$  defining the ratio of the true airflow rate to the theoretical is introduced. This yields:

$$q_{orifice} = C_f C_c a_2 \sqrt{\frac{2 \cdot (p_1 - p_2)}{\rho \cdot (1 - C_c^2 (a_2/a_1)^2)}} \quad (Equation 2.34)$$

Von Mises (see Olson, 1968) has shown from potential flow theory (i.e. ideal flow theory of an inviscid fluid) that the contraction coefficient ( $C_c$ ) is

equal to  $\pi/(\pi+2) = 0,611$  when  $a_2/a_1 = 0$  and the approach angle is equal to 90 degrees. Von Mises also calculated the contraction coefficient for different area ratios and at different flow approach angles, see Figure 2.12. The potential flow calculations are 2-dimensional, which means that  $C_c = b_{vc}/b_{pipe}$ , but this ratio is equal to  $a_{vc}/a_1$  in the axisymmetrical case.

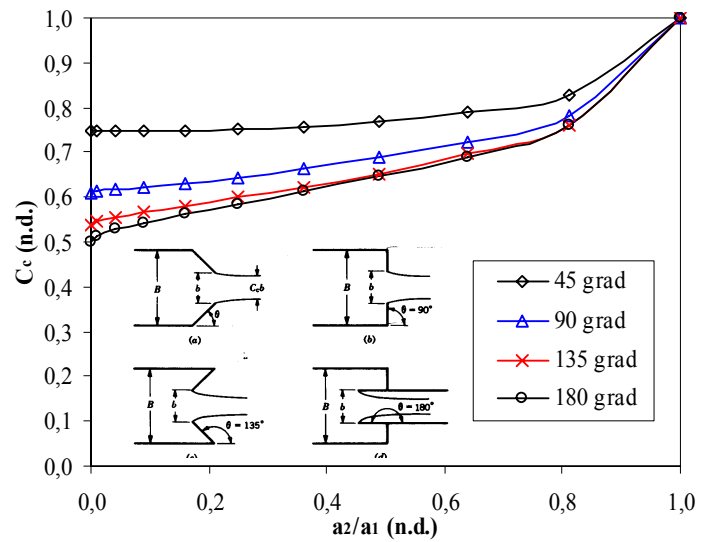


Figure 2.12 The contraction coefficient ( $C_c$ ) found from potential flow theory as a function of the area ratio ( $a_2/a_1$ ) (Olson, 1968).

Equation 1.34 can be simplified by introducing an overall discharge coefficient ( $C_D$ ):

$$q_{orifice} = C_D a_2 \sqrt{\frac{2 \cdot (p_1 - p_2)}{\rho \cdot (1 - (a_2/a_1)^2)}} \quad (\text{Equation 2.35})$$

$$\text{Where } C_D = C_f \cdot C_c \cdot \sqrt{\frac{1 - (a_2/a_1)^2}{1 - C_c^2 \cdot (a_2/a_1)^2}} \quad (\text{Equation 2.36})$$

Alternatively the discharge coefficient can be defined as (K):



$$q_{orifice} = K a_2 \sqrt{\frac{2 \cdot (p_1 - p_2)}{\rho}} \quad (\text{Equation 2.37})$$

$$\text{Where } K = \frac{C_f \cdot C_c}{\sqrt{1 - C_c^2 \cdot (a_2/a_1)^2}} \quad (\text{Equation 2.38})$$

Equation 1.37 is the commonly used flow equation for openings in the design of natural ventilation.

Figure 2.13 shows the discharge coefficients ( $C_D$  and  $K$ ) based on values from the German standard (DIN 1952, 1982) compared with the values found from potential flow theory (calculating the discharge coefficients using equations 1.36 and 1.38).

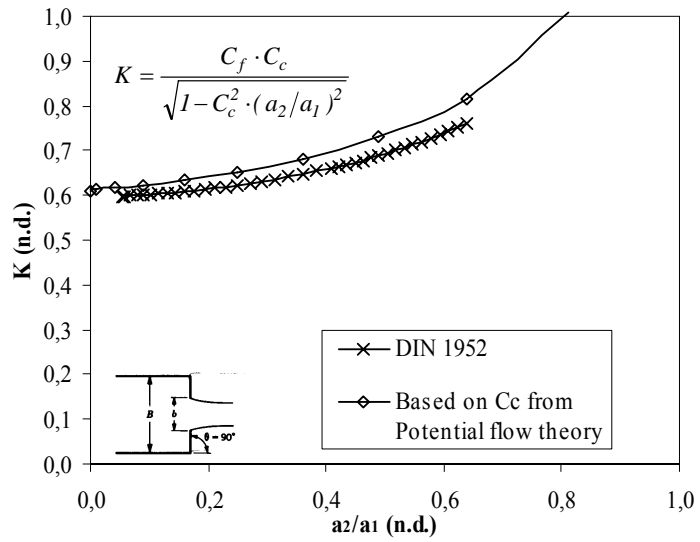
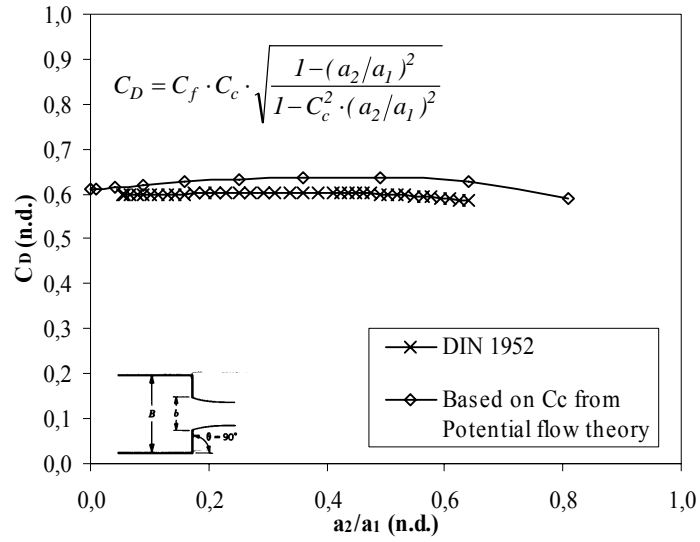


Figure 2.13 Discharge coefficient ( $C_D$ ) and flow coefficient ( $K$ ) found from values based on measurements and from potential flow theory.

The values follow the same pattern, but there is a deviance in the results due to the values found from potential flow theory are based on an ideal fluid ( $C_f = 1$ ). Expressing the discharge coefficient ( $C_D$ ) as in equation 1.36 yields an almost constant value independent of the area ratio.

The flow coefficient ( $K$ ) exceeds 1 for the values based on potential flow theory and the VDI values seems to have the same tendency if these were extended, this is due to the definition of  $K$  (see equation 1.38). In the same way flow coefficient values of Venturi tubes and flow nozzles can be found to be higher than 1 (see DIN 1952, 1982). However the orifice to pipe diameter ratio for orifices used in the measurement of airflow has to be between 0.2 – 0.8 (DIN 1952, 1982) corresponding to a max area ratio of 0.64.

Ower and Panckhurst (1977) have summed up the factors that affect the magnitude of the discharge coefficient. These are:

- (a) The density of the fluid ( $\rho$ )
- (b) The viscosity of the fluid ( $\mu$ )
- (c) The compressibility of the fluid
- (d) A speed characteristic of the flow ( $v$ )
- (e) The diameter of the constriction at the throat ( $d_2$ )
- (f) The diameter of the pipe ( $d_1$ )
- (g) The roughness of the pipe, expressed in terms of the average height of the excrescences ( $t$ ).
- (h) The velocity distribution in the pipe upstream of the constriction.

Neglecting (c) and (h), the factors influencing the discharge coefficient can be written as:

$$C_D = f(Re_2, a_2/a_1, t/d_1) \quad (\text{Equation 2.39})$$

The effect of the pipe roughness is usually small in practice and it is therefore often neglected. This effect of the pipe roughness depends on the size of the pipe and an analysis of this can be found in (Johansen, 1930).

The velocity or the Reynolds number in the flow is another important factor that influences the discharge coefficient. Figure 2.14 shows the low-Reynolds number effect on the discharge coefficient for different area ratios.

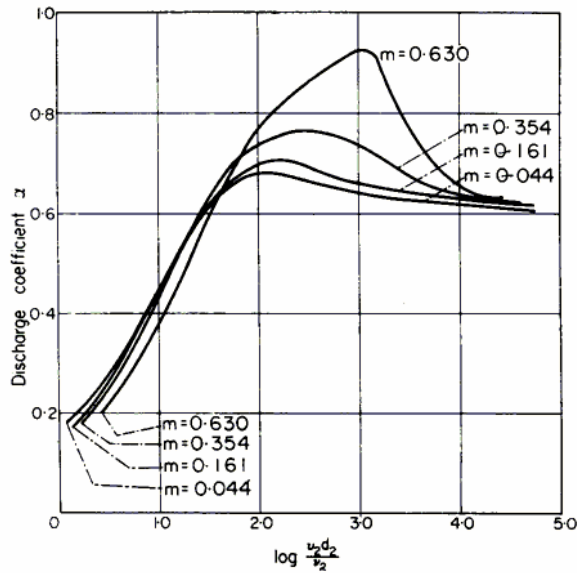


Figure 2.14 Orifice coefficients at low Reynolds numbers (Ower and Panckhurst, 1977). The factor  $m$  is equal to the area ratio ( $a_2/a_1$ )

#### 2.4.4. ORIFICE FLOW VS. FLOW THROUGH OPENINGS IN BUILDINGS

Comparing the flow through an orifice placed in a pipe with the flow through an opening in a building the use of the discharge coefficient found from a plate orifice can hardly be justified. The flow in a pipe is forced through the opening whereas the flow through an opening placed in a building has a “choice” of going into the opening or around the building (see Figure 2.15). The value of  $C_D = 0.6$  is however commonly used in connection with design of natural ventilation. This value is equal to the

coefficient (K) depicted in Figure 2.13 (for  $a_2/a_1 = 0$ ), and the equation used for the determination of the airflow rate is identical to equation 1.30:

$$q = C_D A \sqrt{\frac{2\Delta P}{\rho}} \quad (\text{Equation 2.40})$$

This would immediately imply (from equation 1.31) that the discharge coefficient is equal to  $C_f C_c / \sqrt{1 - C_c^2 (A_2/A_1)^2}$ , however since a determination of  $A_1$  (the area of the pipe, or the cross-sectional area of the upstream “flow tube” see Figure 2.15) is difficult to calculate the value of the area ratio ( $A_2/A_1$ ) is considered to be 0 or at least insignificant, and therefore:

$$C_D = C_c C_f \quad (\text{Equation 2.41})$$

If the depiction to the right in Figure 2.15 is considered the area ratio for flow through building envelope openings seems to be closer to 1 than 0 and the area ratio will have a large effect on the magnitude of the discharge coefficient (see Figure 2.13).

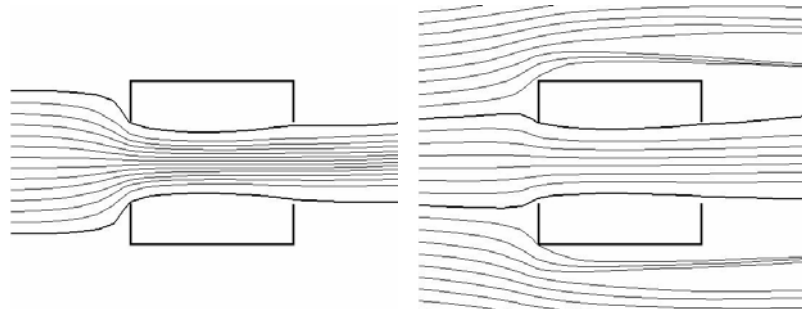


**Figure 2.15** Airflow forced through an opening (left) and “choice” airflow (right). The constricting pipe for the forced flow is not shown in the depiction.

Despite the fact that the use of the discharge coefficient may be dubious good results have been obtained for small openings, i.e. “cracks”.

## 2.5. CRACK FLOW AND FLOW THROUGH LARGE OPENINGS

The determination of whether an opening can be considered to be a crack or a large opening is dependent on a large number of factors, such as: Size, shape and location of opening, building geometry, room geometry, flow obstructions in the room, wind direction and microclimate.

The flow through small openings or “cracks” is “purely” pressure driven, which means that the jet is dissolved into the open space (the room or building) and the pressure distribution inside the room is uniform when an isothermal flow is considered. The flow in small openings is unidirectional, whereas the flow in a large opening can be bidirectional. The “size” of an opening is therefore not only dependent on the geometrical size of the opening, but also on factors that affect the general flow situation.

A crack is normally a narrow opening where the length of the opening is large compared to the depth of the opening. If the length of the opening is large enough the flow in the opening can be divided into two regions: An entry region and a fully developed region, (Etheridge and Sandberg, 1996).

Figure 2.16 shows a wind tunnel study of the airflow through a house provided with two large openings located opposite each other. The size of the openings has been varied. The flow is made visible using the particle method. Particles (semolina powder) have been scattered in a thin and uniform layer on the floor of the model building. Within areas with high velocity the particles are blown away by the wind in the wind tunnel. The direction of the wind was  $45^\circ$  and the size of the openings is defined by the porosity shown in the figure.

For the larger openings, the figure clearly displays the flow contact between the openings as manifested by the particle free path between the openings. However, at the smallest porosity there is no path between the openings. This can be interpreted as there being no flow contact which is one of the characteristics of a crack (Murakami et al 1991). Of course, in this case, the

absence of flow contact is affected by the presence of semolina powder. By decreasing porosity the flow is deflected towards the normal of the opening. This is a well-known property of a flow through screens (Laws et al 1978).

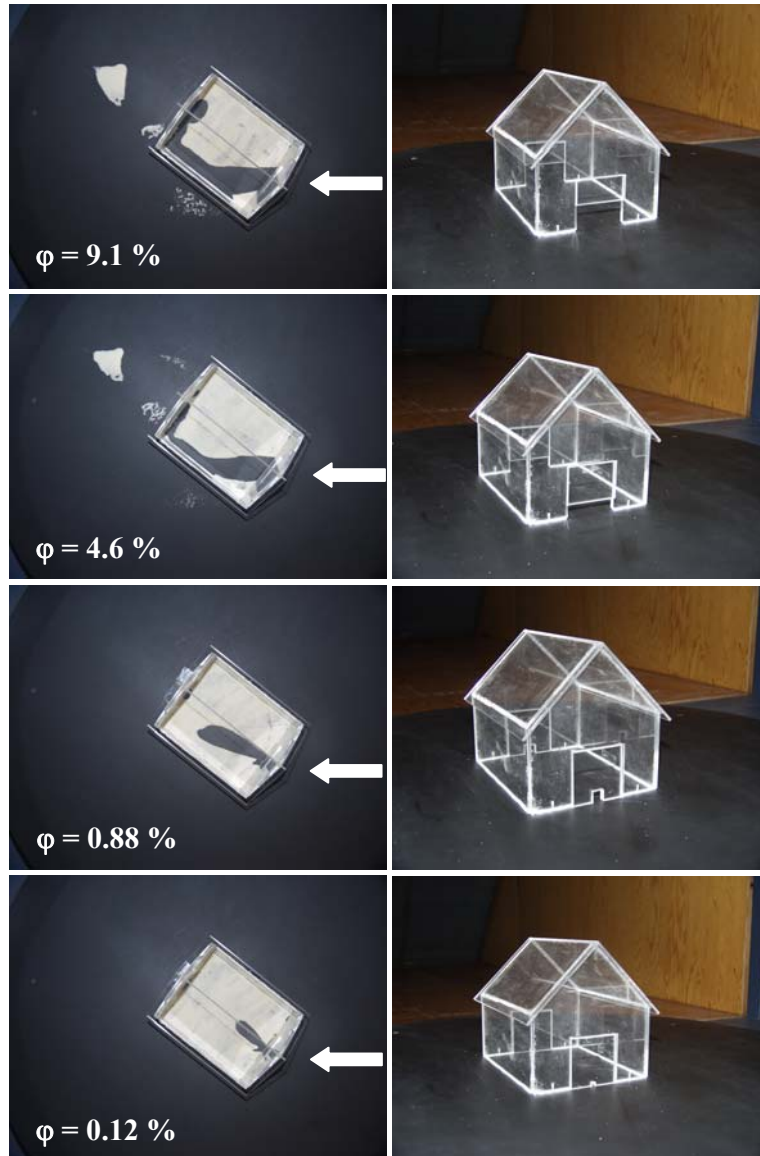
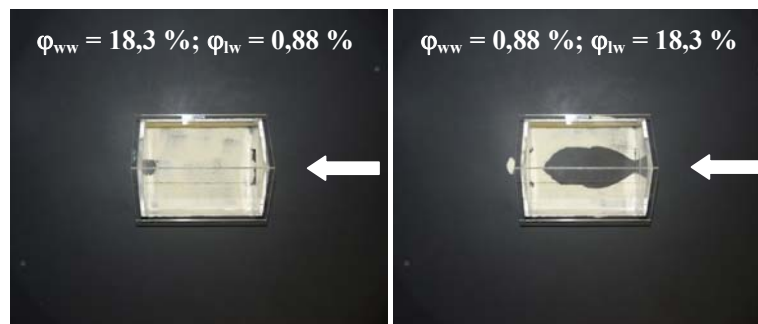


Figure 2.16 Visualisation of the internal flow (left side pictures). Wind coming from the right of the picture. The right side figures shows the corresponding openings in the model house.



As mentioned earlier not only the immediate size of the opening and the wind direction as shown in Figure 2.16 has an impact on the flow situation in a building. The area ratio of the openings also has a large impact on the flow situation in a building. Figure 2.17 shows the similar wind tunnel study of a cross ventilated house provided with openings located opposite each other. Here the size of the windward opening and leeward opening differs, the corresponding porosities are shown in the figure.



**Figure 2.17 Visualisation of internal airflow in case of different windward and leeward opening size.**

There is a clear difference in the internal flow pattern, when the windward opening is large compared to the leeward and vice versa. The particles at the inlet in the first mentioned case do not seem to be effected by the wind since the velocities are too low. Particle movement is however detected at the outlet. The second case shows that a jet is formed from the smaller inlet and only low velocities appear at the outlet. A similar jet will appear at the outlet of the first mentioned case and the airflow rate will be approximately the same in the two cases (In chapter 5 it will be shown that there is a difference in the airflow rate for the two cases.).

The problem of determining the flow rate ( $q$ ) is dependent both on parameters describing the shape of the building and the internal structure in contact with the flow through the building.

Considering a building with the layout shown in Figure 1.6 where  $U_0$  is the reference velocity,  $\beta$  is the wind direction and  $\Delta P$  is the pressure difference across the building envelope where the openings are placed.

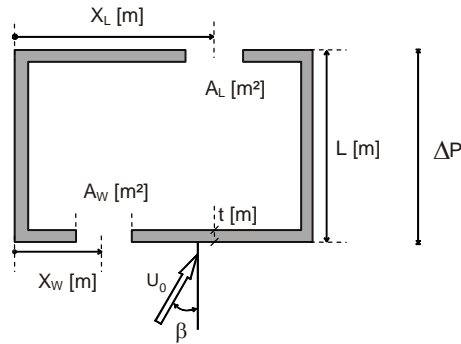


**Figure 2.18 Important parameters in the determination of airflow through a building.**

The wind induced pressure distribution on the building and hereby the driving pressure for the airflow through the openings will be dependent on the shape of the building which can be described by the following aspect ratios:

$$\left( \frac{L}{\sqrt{A_B}}, \frac{H}{\sqrt{A_B}} \right) \quad (\text{Equation 2.42})$$

Where  $A_B$  is the area of the building facade.

Similarly internal structure can be expressed by the following aspect ratios:

$$\left( \frac{X_W}{\sqrt{A_B}}, \frac{X_L}{\sqrt{A_B}}, \frac{X_W - X_L}{\sqrt{A_B}}, \frac{A_W}{A_B}, \frac{A_L}{A_B}, \frac{A_W}{A_L} \right. \\ \left. , f \frac{t}{\sqrt{A_W}}, f \frac{t}{\sqrt{A_L}}, f \frac{L}{\sqrt{A}}, \dots \right) \quad (\text{Equation 2.43})$$

The parameters in Equation 1.43 include the position of the openings in the facade, their relative position in the facade (i.e. seeing each other or not), the size of the opening in relation to the facade area (porosity), the relative size of inlet and outlet openings (the larger or smaller opening coming first) and friction against the opening sides and against the room surfaces.

Wind related parameters can be expressed by the wind direction and the turbulence in the wind:

$$\left(\beta, \frac{\lambda_{Turb}}{\sqrt{A_w}}\right) \quad \text{(Equation 2.44)}$$

where  $\lambda_{Turb}$  is the turbulent length scale.

The ratio  $\lambda_{Turb}/\sqrt{A_w}$  is the gust size in relation to the size of the opening. If  $\lambda_{Turb}/\sqrt{A_w} \ll 1$  (high frequency part) the produced pressure fluctuations are correlated only over a small part of the opening. On the other hand if  $\lambda_{Turb}/\sqrt{A_w} \gg 1$  (low frequency part) the pressure fluctuations are correlated over a large part of the opening.

A crack is normally an adventitious opening that is narrow. Therefore  $t/\sqrt{A_w} \gg 1$  and subsequently the friction against the opening sides is important.

For a large opening  $t/\sqrt{A_w} \ll 1$  and therefore the friction against the opening sides is negligible. Between openings in a building there is a flow contact manifested by a “flow tube” between the openings. This property can be taken as a definition of an opening. Examples of airflow patterns in rooms provided with large openings are shown in (Sawachi 2002).

## 2.6. AIRFLOW AROUND BUILDINGS

The subject of airflow around buildings is a topic which is of interest in both structural engineering as well as HVAC engineering. The determination of wind loads on buildings is important in calculation of

structural stability of buildings and the surface pressure generated by the wind is important in the determination of driving pressures in natural ventilation design as well as in the calculation of air infiltration.

### *2.6.1. FLOW PATTERN AROUND BUILDING*

The pressure in front of a building has a “built up” distance which is approximately 5 times the height of the building, and the region of low pressure behind the building extends more than  $6\cdot H$  (Baturin, 1972). If a building is sheltered by a similar building parallel to it upstream, the pressure on the second building is dependent on the distance between the buildings. The pressure on the front wall will not be fully restored until the distance is greater than  $15\cdot H$  (Baturin, 1972).

When a building is exposed to a boundary layer type flow, the building causes a disturbance in the wind and there is a vortex built up in front of the building and a flow separation above the building as well as to the sides. The flow will reattach to the roof if the length of the building is sufficiently large. The disturbance of the building reaches as far downstream as 15 times the height of the building. The airflow and hereby the surface pressure distribution on a building is dependent on the approaching wind, Figure 2.19 shows the streamlines and the corresponding pressure distribution of a quadratic building exposed to, respectively, a uniform flow and a flow with a real wind profile.

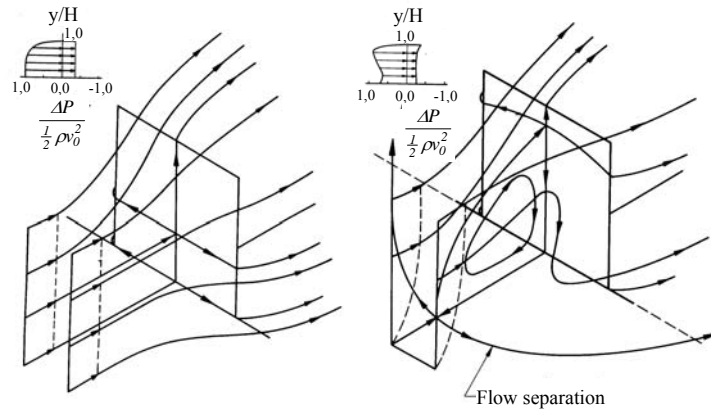


**Figure 2.19 Airflow around quadratic shaped building exposed to a uniform flow and a flow with a wind profile (Petterson et al., 1969).**

The vortex in front of the building is eliminated when the building is exposed to a uniform flow due to the fact that it is not possible to displace the air to the lower part. The corresponding pressure distribution is as a result of this, uniform at the lower part of the windward side as well as on the leeward side of the building. When the building is exposed to the wind profile a vortex is created in front of the building and the pressure distribution is also altered significantly. Due to the velocity of the wind is higher at the upper part of building the corresponding pressure is higher here than at the bottom and the air seeks downwards towards the area of lower pressure.

Available data of wind induced surface pressure distributions focuses on rectangular shaped buildings, and values obtained by measurements can be found in (Orme et al., 1994), (Allard et al., 1996), (Baturin, 1972). However if the geometry of the building or the surroundings differs too much from the standard cases found in literature the flow pattern may be altered and the need for wind tunnel or CFD modelling is required. The ASHRAE fundamentals handbook prescribes that buildings of an even slightly complex shape, such as a L- or U-shaped structures, can generate flow

patterns too complex to generalise for design (ASHRAE Fundamentals, 1993).

The use of computational determination of the airflow around buildings by CFD is becoming increasingly popular. The influence of computational parameters on the airflow around buildings have been studied by (Summers et al., 1986), (Murakami, 1989), (Baskaran, 1992). Fairly good correspondence between measurements and the simulated results were reported, and the accuracy from an engineering point of view sufficient.

### 2.6.2. WIND PROFILE

Due to the roughness of the terrain the wind is subjected to shear stresses from the ground that it passes. A boundary layer flow is established near the ground. The velocity of the wind is lowest at the ground and gradually increasing with the height. The velocity distribution for a wind profile can be described by the logarithmic profile (Monin and Yaglom, 1971):

$$\frac{u_z}{u_*} = \frac{1}{\kappa} \ln \left( \frac{z}{z_0} \right) \quad (\text{Equation 2.45})$$

Where  $u_z$  is the velocity at height  $z$ .  
 $u_*$  is the friction velocity  
 $\kappa$  is the Karman constant ( $\approx 0.4$ )  
 $z_0$  is the surface roughness.

The friction velocity ( $u_*$ ) represents the shear stress, and is defined as  $\tau = \rho u_*^2$ .

However since this expression is not good for practical use, good approximation can be obtained by a power law expression (Andersen et al., 2002):

$$\frac{u_h}{u_{10}} = k \cdot h^\alpha \quad (\text{Equation 2.46})$$

Where  $u_h$  is the velocity at height  $h$   
 $u_{10}$  is the wind velocity in "flat terrain" in 10 m height.

*k and  $\alpha$  are factors dependent on the terrain.*

(Andersen et al., 2002) prescribes the values shown in Table 2.3 for different types of terrain.

Type of Terrain	k	$\alpha$
Open, flat country	0,68	0,17
Urban area	0,35	0,25
City area	0,21	0,33

**Table 2.3 Factors describing the wind profile dependent on terrains of different roughness. From (Andersen et al., 2002)**

## 2.7. SIMILARITY PRINCIPLES

It is not always possible to conduct full-scale measurements and in these instances scale models can be an adequate alternative. Also from an economical point of view it is generally cheaper to construct a scale model than it is to create a full scale model in a laboratory. Scale models are common in wind tunnel studies and are used in various sciences and industries.

In order for scale models to be comparable with reality it is necessary for certain conditions to be fulfilled. These conditions consists of the relative boundary conditions being equal as well as the dimensionless numbers ( $Ar$ ,  $Re$  and  $Pr$ ) being equal. Additionally the characteristic constants for a given fluid should not vary too much. The general theory of similarity principles can be found in (Etheridge and Sandberg, 1996), (Nielsen, 1999) and (Awbi, 1991).

If the variables in the governing flow equations (see section 2.2) are made dimensionless (related to characteristic values for each variable for the given flow situation), the dimensionless numbers ( $Ar$ ,  $Re$  and  $Pr$ ) will appear in these equations. The dimensionless numbers are defined by: Reynolds number:  $Re = h_0 u_0 / \nu$ , Archimedes number:  $Ar = \beta g h_0 \Delta T / u_0^2$  and Prandtl number:  $Pr = \mu c_p / \lambda$ .

Having these numbers in mind it is clear that a model scaled by a factor  $1/f$  means that the velocity  $u_0$  has to increase by  $f$  in order for the Reynolds numbers to be identical. In order for the Archimedes numbers to be identical between reality and model the temperature has to increase by  $f^3$ . This means that large scaling factors will increase the temperature level dramatically. Since it is not always possible to obtain these very high temperature levels, another possibility is to ignore the Reynolds number on grounds that a fully turbulent flow should be independent of the Reynolds number. Alternatively a different fluid can be used and in the same way ignoring the Prandtl number on grounds that the flow is fully turbulent. Examples of using saltwater bath models for the analysis of buoyancy driven natural ventilation can be found in literature (see Andersen et al., 2000, Hunt et. al., 2000, Li et al., 2001 and Chen et al., 2000).



### 3. MEASUREMENTS AND METHODS

This chapter contains a description of the conducted measurements and the experimental methods used in connection with the project. All measurements were conducted in a wind tunnel at the Centre for Built Technology at the University of Gävle in Sweden.

#### 3.1. EXPERIMENTAL METHODS

##### 3.1.1. PRESSURE MEASUREMENTS

The pressure measurements were conducted using a transducer of the type *Druck PCDR22*. The pressure measuring device is an elastic deformation device which consists of a membrane connected to strain gages measuring the strain of membrane. In order to measure the pressure in given locations rubber tubes were connected to the transducer and since only one transducer was available more tubes could be connected to a valve (of the type *Scanivalve*) and hereby the pressure could be measured in multiple locations consecutively.

The measuring device was connected to a computer system where the measurements could be programmed and analysed. The output of the system were the pressure coefficients based on:

$$C_p = \frac{P - P_{s,2}}{P_{Dyn,1}} = \frac{P - P_{s,2}}{(P_{Total,1} - P_{s,1}) \cdot Q_{fact}}$$

Where  $P$  is the measured static pressure,  $P_{s,2}$  is the static pressure measured 10 cm below the ceiling in the middle of the wind tunnel (A Prandtl tube was fixed at this location),  $P_{Total,1}$  and  $P_{s,1}$  are the total and static pressures at a user given location and  $Q_{fact}$  is a correction factor compensating for any blockage effects.

The correction factor  $Q_{fact}$  is only important in case of the blockage area of the model being significant. The simple model described in chapter 5 is

small compared to the cross sectional area of the wind tunnel ( $A_{\text{model}}/A_{\text{WT}} = 0.4 \%$ ) which only results in a minor change in the pressure levels.

The scale model described in chapter 6 is on the other hand relatively large compared to the wind tunnel and the blockage effect is dependent on the angle at which the model is placed, see

Figure 3.1.

Figure 3.1 shows the area ratio squared as a function of the wind incident angle. The depicted area ratio (to the second power) is approximately equal to the ratio of the dynamic pressures with and without the model placed in the wind tunnel (assuming that the pressure loss due to the model does not affect the airflow rate from the ventilator).

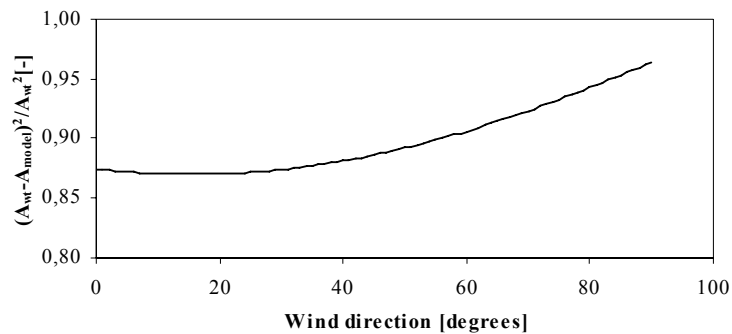


**Figure 3.1** Area ratio to the second power as a function of the wind incident angle.

The depicted area ratio should be equal to the factor ( $Q_{\text{meas}}$ ) mentioned earlier. However instead of using this factor the pressure was measured in the wind tunnel without the model in the height of the building and compared to the measured pressure with the model placed in the wind tunnel and in the same height but placed approximately 0.8 m upstream and 1 m to the side of the model. Here the factor was found to lie in the interval 0.77 – 0.84 dependent on the wind direction.

A measuring frequency of 10 Hz was used for both models described in chapter 5 and 6, while the number of samples was 150 for the simple model and 300 for the scale model due to higher turbulence.

### 3.1.2. VELOCITY MEASUREMENTS

In order to obtain knowledge of the airflow through the objects the velocity was measured in the vicinity of the openings. This was done using a hot wire anemometer placed in multiple locations in order to retrieve the velocity profile in the openings. The velocities were measured using a hot wire anemometer.

The hot-wire anemometer is a device measuring the temperature change on a thin electrically heated wire (caused by the flow of the fluid) and comparing this to the electrical current and the resistance in the wire. These relations are compared by two expressions describing the heat transfer rate (Holman, 1994):

$$q = (a + b\sqrt{u})(T_w - T_\infty) \quad (\text{Equation 3.1})$$

$$q = i^2 R_0 (1 + \alpha(T_w - T_0)) \quad (\text{Equation 3.2})$$

Where  $T_w$  is the wire temperature

$T_\infty$  is the temperature of the fluid

$u$  is the fluid velocity

$a$  and  $b$  are calibration constants

$i$  is the electrical current

$R_0$  is the resistance of the wire at temperature  $T_0$

A small sized hot-wire anemometer was employed in the measurements in the current project in order to minimise the influence on the flow.

## 3.2. WIND TUNNEL

The wind tunnel used for the measurements is located at the Centre for Built Technology at the University of Gävle in Sweden. The wind tunnel

has a total length of 28 m and a working section of 11 m. In the working section the cross sectional area is  $3 \times 1.5$  m (Width  $\times$  Height). The sketch of the wind tunnel is shown in Figure 3.2.

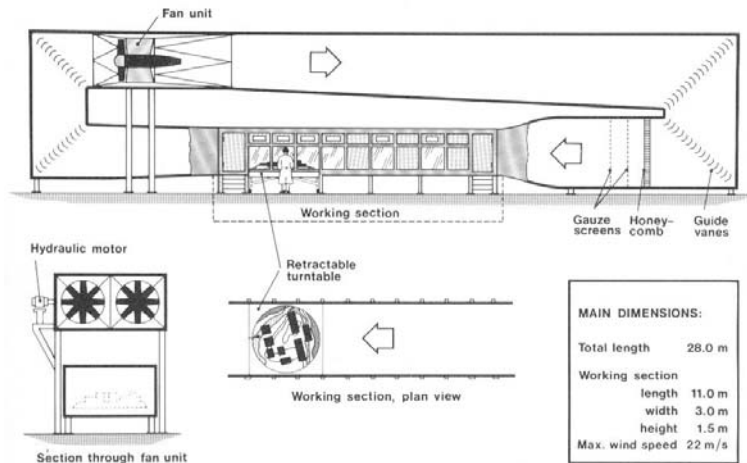


**Figure 3.2** The wind tunnel at the Centre for Built Technology at the University of Gävle.

The wind tunnel is equipped with a retractable turntable where the model can be placed and exposed to wind directions of chosen magnitude. In the remaining part of the working section upstream of the turntable roughness elements can be placed to create a wind profile.

## 4. COMPUTATIONAL FLUID DYNAMICS

Computational fluid dynamics, or CFD as it will be referred to in the following, is a computer based numerical solution method of the governing flow equations described in chapter 2. CFD has a wide spread use in industrial and research applications, and has been used for the study of complex flow phenomena for about 50 years. CFD has evolved to be an effective analysis tool, and can be a time and cost effective alternative to measurements. The validity and reliability of numerical simulations is however still dependent on measurements. Many researchers carry out measurements for comparative reasons, and when an approximate coincident solution has been obtained between the measurements and the similar computational model, then the predictions can be extended to other similar models for analysis purposes. Many sources of errors may lead to incorrect predictions, which is still one of the large hurdles for using CFD as an analysis or design tool. (Li, 1994) has summed up the possible sources of errors in predicting room airflow:

- *Assumptions in physical models*
- *Uncertainties in boundary and initial conditions*
- *Errors in geometry representation*
- *Discretisation errors*
- *Iteration errors*

### 4.1. NUMERICAL METHOD

The most commercial CFD codes use the so called finite volume method which is based upon the solution domain being divided into a number of smaller volumes for which the governing flow equations are solved.

#### 4.1.1. THE FINITE VOLUME METHOD

The following is a short description of the control volume method for one dimensional flow, based on a general form of the flow equations:

$$\frac{\partial(\rho \cdot u_i \cdot \phi)}{\partial x_i} = \frac{\partial}{\partial x_i} \left( \Gamma_\phi \cdot \frac{\partial \phi}{\partial x_i} \right) \quad (\text{Equation 4.1})$$

Where  $\phi$  is the general variable  
 $\Gamma_\phi$  is a diffusion coefficient

In order to solve the governing flow equations a control volume shown in Figure 4.1 is considered.

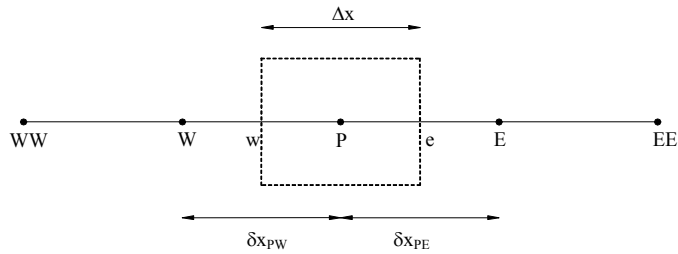


**Figure 4.1 Control volume portioning for 1D.**

By integrating Equation 1.1 we obtain:

$$\int_w^e \frac{\partial(\rho \cdot u \cdot \phi)}{\partial x} dx = \int_w^e \frac{\partial}{\partial x} \left( \Gamma_\phi \cdot \frac{\partial \phi}{\partial x} \right) dx \Leftrightarrow$$

$$(\rho \cdot u \cdot \phi)_e - (\rho \cdot u \cdot \phi)_w$$

$$= \left( \Gamma_\phi \cdot \frac{\partial \phi}{\partial x} \right)_e - \left( \Gamma_\phi \cdot \frac{\partial \phi}{\partial x} \right)_w \quad (\text{Equation 4.2})$$

In order to solve this expression the unknown variables ( $\phi$ ) need to be approximated. An exposition of the different approximation methods or differencing schemes for the finite volume method can be found in (Versteeg et al., 1995) or (Nielsen, 1994).

The most common differencing scheme used in commercial CFD is the “hybrid scheme” which consists of the central differencing scheme and the

1. order upwind differencing scheme. The central differencing leads to misleading results at high Peclet numbers ( $Pe = (\rho \cdot u) / (\Gamma / \delta x)$ ) and therefore a 1. order upwind scheme is used when  $|Pe| > 2$ .

The central differencing scheme consists of the variables being determined both from what is upstream as well as what is downstream. The variables are approximated by:

$$\phi_e = (\phi_P + \phi_E) / 2, \quad \phi_w = (\phi_W + \phi_P) / 2, \quad \left( \frac{\partial \phi}{\partial x} \right)_e = \frac{\phi_E - \phi_P}{\delta x_{PE}} \quad \text{and} \quad \left( \frac{\partial \phi}{\partial x} \right)_w = \frac{\phi_P - \phi_W}{\delta x_{PW}}$$

And hereby Equation 1.2 can be written as:

$$\begin{aligned} & \rho \cdot u_e \cdot \frac{\phi_P + \phi_E}{2} - \rho \cdot u_w \cdot \frac{\phi_W + \phi_P}{2} \\ & = \Gamma_{\phi_e} \left( \frac{\phi_E - \phi_P}{\delta x_{PE}} \right) - \Gamma_{\phi_w} \left( \frac{\phi_P - \phi_W}{\delta x_{PW}} \right) \end{aligned} \quad (\text{Equation 4.3})$$

The hybrid differencing scheme utilises the upwind scheme when the Peclet number is larger than 2 ( $|Pe| > 2$ ). This scheme is, as the name indicates, only dependent on what is upstream and is defined by the values ( $\phi_e$  and  $\phi_w$ ) being equal to the upstream value:

$$\phi_e = \phi_P \quad \text{and} \quad \phi_w = \phi_W, \quad \text{if } \rho \cdot u > 0 \quad \text{and} \quad \phi_e = \phi_E \quad \text{and} \quad \phi_w = \phi_P, \quad \text{if } \rho \cdot u < 0.$$

The diffusion terms in Equation 1.3 is still determined by the central differencing scheme.

In the present thesis the CFD code Fluent™ has been used and the available schemes are 1. and 2. order upwind, Power law scheme and the Quick scheme (Fluent, 1998). A description of the utility and sources of error for different differencing schemes can be found in (Versteeg, 1995) or (Patankar, 1995).

## 4.2. TURBULENCE MODELLING

The numerical simulation of turbulent flow can be carried out in three different ways: Direct numerical simulation (DNS), Large eddy simulation (LES) and Reynolds Average Navier Stokes simulation (RANS).

In DNS the instantaneous Navier Stokes equations are solved and the solution domain must be large enough to contain the largest eddies and the grid dense enough to resolve the smallest eddies. The ratio of the largest to the smallest scales in a turbulent flow is approximately proportional to  $Re^{3/4}$  in each direction, which means that the total number of grid points is proportional to  $Re^{9/4}$ , and the time step should approximately be the turnover time of the smallest eddy. These factors means that at the present the usefulness of DNS in engineering application is limited, and will remain so until the necessary computer power is available.

In LES only the large eddies are resolved directly whereas the smaller scales of turbulence are modelled. The use of LES for the determination of building airflow is becoming increasingly important. A comparison of various turbulence models (including LES) in the determination of the flow field around a building have been reported by (Murakami et al. 1992,1993a, 1993b). The airflow in a room has been simulated using LES by (Davidson and Nielsen, 1996) and (Zhang and Chen, 2000), and the application of LES in analysis of natural ventilation has been carried out by (Jiang et al., 2001, 2002, 2003).

In RANS simulation the whole turbulence spectrum is modelled, which means that the Reynolds stresses mentioned in chapter 2 are modelled in some way. All turbulence models in RANS are based on Boussinesq's *eddy viscosity* concept where the turbulent stresses are proportional to the mean velocity gradients (as stated in equation 2.13). The proportionality factor is called the *eddy viscosity*, since it in the same way as the molecular viscosity describes the proportionality between the shear stress (caused by the turbulent eddies) and the velocity gradients.



#### 4.2.1. MIXING LENGTH MODEL

The earliest turbulence model is the Prandtl mixing length theory developed by Prandtl in 1925. Prandtl's mixing length model is based on dimensional analysis, so that:

$$\nu_t \propto l \cdot \mathcal{G} \quad (\text{Equation 4.4})$$

Where  $\mathcal{G}$  is a velocity scale (m/s)  
 $l$  is a length scale (m)

$l$  is the characteristic length of the largest eddies and the velocity scale ( $\mathcal{G}$ ) is assumed to be  $\mathcal{G} = c \cdot l \cdot |\partial u / \partial y|$  and by combining this with equation 1.4 and absorbing the proportionality factors Prandtl's mixing length model is obtained:

$$\nu_t = l_m^2 \left| \frac{\partial u}{\partial y} \right| \quad (\text{Equation 4.5})$$

Where  $l_m$  is the Prandtl mixing length (m)

Values of mixing lengths for various 2-dimensional turbulent flows are given in (Rodi, 1985). Despite good correspondence between the mixing length model and flows like jets, wakes and boundary layers the model is incapable of describing flows with separation and recirculation which are common in flows in and around buildings.

#### 4.2.2. $k$ - $\varepsilon$ MODEL

Today the most commonly used RANS model is the  $k$ - $\varepsilon$  turbulence model which is based on the eddy viscosity being described by the turbulent kinetic energy ( $k$ ) and the dissipation of this ( $\varepsilon$ ):

$$\nu_t = C_\mu \cdot \frac{k^2}{\varepsilon} \quad (\text{Equation 4.6})$$

Two additional transport equations are defined in order to determine  $k$  and  $\varepsilon$  (Launder and Spalding, 1974):

$$\frac{\partial}{\partial x_i}(\rho \cdot u_i \cdot k) = \frac{\partial}{\partial x_i} \left( \frac{\mu + \mu_t}{\sigma_k} \cdot \frac{\partial k}{\partial x_i} \right) + P_k - \rho \cdot \varepsilon \quad (\text{Equation 4.7})$$

$$\begin{aligned} & \frac{\partial}{\partial x_i}(\rho \cdot u_i \cdot \varepsilon) \\ &= \frac{\partial}{\partial x_i} \left( \frac{\mu + \mu_t}{\sigma_\varepsilon} \cdot \frac{\partial \varepsilon}{\partial x_i} \right) + \frac{\varepsilon}{k} \cdot (c_1 \cdot P_k - c_2 \cdot \rho \cdot \varepsilon) \end{aligned} \quad (\text{Equation 4.8})$$

$$\text{Where } P_k = \mu_t \cdot \left( \frac{\partial u_j}{\partial x_i} + \frac{\partial u_i}{\partial x_j} \right) \cdot \frac{\partial u_j}{\partial x_i}$$

$$C_\mu = 0.09, \quad c_1 = 1.44, \quad c_2 = 1.92, \quad \sigma_k = 1.0 \text{ and } \sigma_\varepsilon = 1.3.$$

The above mentioned constants are based on a comparative evaluation with experiments of different free turbulent flows (see Launder et al., 1972).

The standard  $k$ - $\varepsilon$  model is the most widely validated turbulence model and has been shown to perform well for many flows (see Rodi, 1985). However the  $k$ - $\varepsilon$  model is based on the turbulence being isentropic (i.e. the eddy viscosity being the same for all Reynolds stresses) and the model shows a lack in determining the flow in unconfined flows. The spreading rate in axisymmetrical jets has also been found to be severely overpredicted (Versteeg and Malalasekera, 1995). Several additions or modifications have been made to the standard  $k$ - $\varepsilon$  model to improve the performance for different flows, e.g. (Shih et al., 1995) and (Yakhot and Orzag, 1986).

#### 4.2.3. REYNOLDS STRESS MODEL

One way of accounting for the non isentropic aspects of turbulence is to set up transport equations for each of the Reynolds stresses, which is the concept of the Reynolds stress turbulence model (RSM), (see Launder et

al., 1975). The transport equations for the Reynolds stresses are given in equation 1.9 and were first given in their exact form by (Chou, 1945).

$$\begin{aligned}
 & \underbrace{\frac{\partial}{\partial t}(\overline{\rho u_i u_j}) + \frac{\partial}{\partial x_k}(\overline{\rho U_k u_i u_j})}_{\text{Local time derivative}} = \\
 & \underbrace{-\frac{\partial}{\partial x_k} \left( \frac{\mu_t}{\sigma_k} \frac{\partial \overline{u_i u_j}}{\partial x_k} \right)}_{D_{ij}^T \equiv \text{Turbulent diffusion}} + \underbrace{\frac{\partial}{\partial x_k} \left[ \mu \frac{\partial}{\partial x_k} (\overline{u_i u_j}) \right]}_{D_{ij}^M \equiv \text{Molecular diffusion}} \\
 & \underbrace{-\rho \left( \overline{u_i u_k} \frac{\partial U_i}{\partial x_k} + \overline{u_j u_k} \frac{\partial U_i}{\partial x_k} \right)}_{P_{ij} \equiv \text{Stress production}} - \underbrace{\beta \frac{\mu_t}{Pr_t} \left( g_i \frac{\partial T}{\partial x_j} + g_j \frac{\partial T}{\partial x_i} \right)}_{G_{ij} \equiv \text{Buoyancy production}} \\
 & + \underbrace{\phi_{ij} - \frac{2}{3} \delta_{ij} \rho \varepsilon}_{\varepsilon_{ij} \equiv \text{Dissipation}} - \underbrace{2 \rho \Omega_k (\overline{u_j u_m} \varepsilon_{ikm} + \overline{u_i u_m} \varepsilon_{jkm})}_{F_{ij} \equiv \text{Production by system rotation}}
 \end{aligned} \tag{Equation 4.9}$$

Where

$$\begin{aligned}
 \phi_{ij} &= \phi_{ij,1} + \phi_{ij,2} + \phi_{ij}^W, \quad \phi_{ij,1} = \\
 & -C_1 \rho \frac{\varepsilon}{k} \left[ \overline{u_i u_j} - \frac{2}{3} \delta_{ij,k} \right] \\
 \phi_{ij,2} &= -C_2 \left[ \begin{aligned} & \left( P_{ij} + F_{ij} + G_{ij} - C_{ij} \right) \\ & - \frac{1}{3} \delta_{ij} (P_{kk} + G_{kk} - C_{kk}) \end{aligned} \right] \text{ and} \\
 \phi_{ij}^W &= C_1' \frac{\varepsilon}{k} \left[ \begin{aligned} & \left( \overline{u_k u_m} n_k n_m \delta_{ij} \right) \\ & - \frac{3}{2} \overline{u_i u_k} n_j n_k \\ & - \frac{3}{2} \overline{u_j u_k} n_i n_k \end{aligned} \right] \frac{k^{3/2}}{\left( C \frac{3}{4} / \kappa \right) \varepsilon d} \\
 & + C_2' \left[ \begin{aligned} & \left( \phi_{km,2} n_k n_m \delta_{ij} \right) \\ & - \frac{3}{2} \phi_{ik,2} n_j n_k \\ & - \frac{3}{2} \phi_{jk,2} n_i n_k \end{aligned} \right] \frac{k^{1.5}}{\left( C \frac{0.75}{\mu} / \kappa \right) \varepsilon d}
 \end{aligned}$$

In addition to these Reynolds stress transport equations there are still two equations for the turbulent kinetic energy ( $k$ ) and the dissipation of this ( $\varepsilon$ ). The turbulent kinetic energy is determined from the Reynolds stresses:

$$k = \frac{1}{2} \overline{u'_i u'_i} \quad (\text{Equation 4.10})$$

Equation 1.10 is the definition of  $k$ .

The dissipation of turbulent kinetic energy is still determined from a transport equation in the same way as in the  $k$ - $\varepsilon$  model:

$$\begin{aligned} \rho \frac{D\varepsilon}{Dt} = \frac{\partial}{\partial x_j} \left[ \left( \mu + \frac{\mu_t}{\sigma_\varepsilon} \right) \frac{\partial \varepsilon}{\partial x_j} \right] \\ + C_{1\varepsilon} \frac{1}{2} \frac{\varepsilon}{k} (P_{ii} + C_{3\varepsilon} G_{ii}) - C_{2\varepsilon} \rho \frac{\varepsilon^2}{k} \end{aligned} \quad (\text{Equation 4.11})$$

Where  $C_{3\varepsilon} = \text{Tanh}(v/u)$

The Reynolds stress turbulence model is still not as validated as the  $k$ - $\varepsilon$  model, but has shown to perform better for some flows (e.g. Wall effects in wall jets, turbulence driven secondary flows and the effects of extra strain rates caused by wall curvature see (Rodi,1985)).

(Murakami et al., 1996) has compared the flow around a cubic building for several turbulence including both the standard  $k$ - $\varepsilon$ , the Reynolds stress and large eddy simulation and has found that the velocity field is best modelled by LES, and the most deviant is the  $k$ - $\varepsilon$  model compared with measurements.

The present author (Jensen True et al., 2002) has found good correspondence between the Reynolds stress model and measurements of the pressure on a circular flat plate placed in a uniform flow, whereas the  $k$ - $\varepsilon$  model was found to overpredict the pressure.

#### 4.2.4. WALL FUNCTIONS

The wall is the most common boundary in confined fluid flow problems such as room airflow. The wall exerts a damping effect on the flow and the turbulent transport equations are not valid close to the wall. This problem is usually solved with the use of wall-functions which are used to connect the viscosity affected region to the fully turbulent region. The standard wall functions are based on a proposal by (Launder and Spalding, 1974) and consists of an expression for the laminar sublayer and an expression for the region affected by both viscosity and turbulent effects (called the log-law layer).

The laminar sublayer is described by:

$$u^+ = y^+ \quad \text{(Equation 4.12)}$$

$$\text{where } u^+ = u / \sqrt{\rho / \tau_w},$$

$$y^+ = y \sqrt{\tau_w \rho} / \mu$$

$\tau_w$  is the wall shear stress,

The log-law region is described by:

$$u^+ = \frac{1}{\kappa} \ln(Ey^+) \quad \text{(Equation 4.13)}$$

Where  $\kappa$  is the von Karmann constant ( $\approx 0.4$ )

$E$  is an empirical constant ( $\approx 9.8$ )

The laminar sublayer applies in the region  $y^+ < 11.63$  and the log law is valid in the region  $30 < y^+ < 60$ , but for calculation purpose is employed for  $y^+ < 11.63$  (Fluent, 1998).

In Fluent™ these factors are replaced by  $u^*$  and  $y^*$  described below, (Fluent, 1998):

$$u^* = (u_p C_\mu^{0.25} k_p^{0.5}) / (\tau_w / \rho) \text{ and}$$

$$y^* = (\rho C_\mu^{0.25} k_p^{0.5} y_p) / \mu$$

Where equation 1.2 applies to  $y^* < 11.225$  and equation 1.3 in the interval  $11.225 < y^* < 500$ .

### **4.3. QUALITY CONTROL OF CFD**

As mentioned earlier in this chapter there are many sources of error in connection to numerical prediction. Therefore quality control of CFD is a major aspect of numerical modelling.

#### *4.3.1. GRID DISTRIBUTION*

Grid sectioning is an important part of numerical modelling since the achievement of a grid independent solution naturally is decisive for the result.

The following will contain an analysis of the grid distribution or grid density of the scale model used in the wind tunnel in chapter 6. The analysis will be based on the  $k$ - $\varepsilon$  model and will not be compared to the measurements described in the later chapter, since the aim is to obtain a numerical grid independent solution. It is assumed that the grid independence will be approximately the same for other turbulence models. The measurements will however be included in the next section when the boundary conditions are analysed and different turbulence models are applied. The grid distribution will be compared by means of the length of the recirculation zone behind the building as well as the pressure built-up in front of the building. The building model is placed with a wind incident angle of 0 degrees and with no openings placed in the building. The geometrical set-up of the wind tunnel and the building is depicted in Figure 4.2.

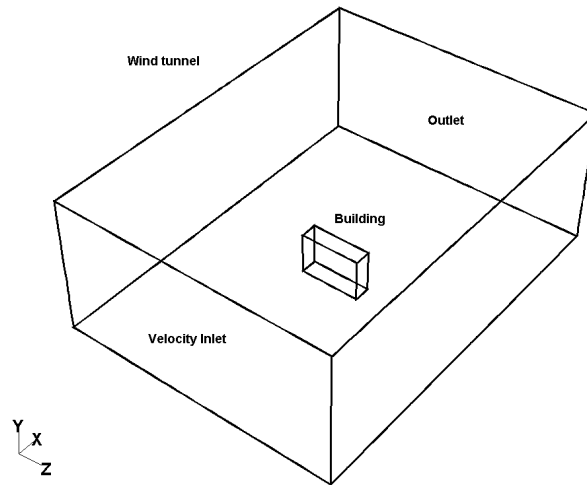


**Figure 4.2 Geometry of the wind tunnel and building used in the grid analysis.**

A length of 2 m have been used for the up- and downstream part of the wind tunnel, and the effect of the roughness elements used in the real wind tunnel have been replaced by a velocity profile placed at the inlet, see chapter 6.

Table 4.1 shows the number of grid points used in the analysis. One of the grids has been subjected to a solution adaptive procedure to see if this results in a better correspondence with the densest grid.

Grid no.	Number of grid
1	3250
2	24500
3	86625
4	212000
4 – Solution adapted	239608
5	630000

**Table 4.1 Grid sizes used in the analysis of grid dependency.**

The grid used in all cases is a structured hexahedral mesh generated in the pre-processing programme Gambit™ which is a part of the Fluent package. The grid named “4 – solution adapted” has been adapted to the pressure gradient ( $DP > 0.005$ ) which means that the grid is refined wherever the pressure gradient is higher than this value.

The grid dependency should be controlled by comparing the whole airflow pattern, i.e. the velocity direction and magnitude of each control volume in the whole solution domain. This seems however unnecessary since only the flow around the building is of interest. Therefore a few factors are extruded and analysed. Figure 4.3 shows the pressure along a straight line through the centre of the building for the various grid sizes.

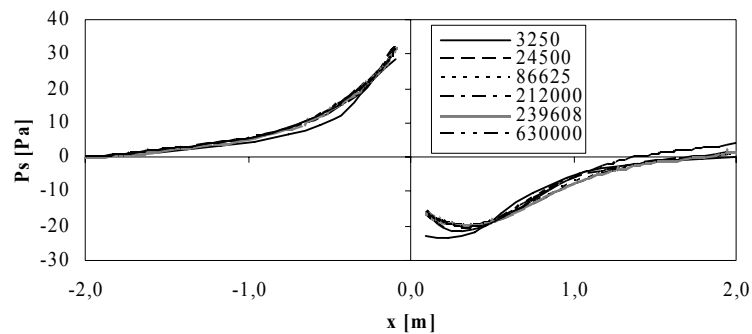


**Figure 4.3 Pressure along a straight line going through the centre of the building.**

The pressure distribution along the "centreline" is almost identical for all grid sizes except maybe for the coarsest grid. The same pattern has been found for the velocity distribution along the same line. Instead of comparing values directly the deviance of chosen factors have been depicted in Figure 4.4 which shows the deviance of the windward, leeward and parallel side pressures and the deviance in the maximum velocities in the secondary directions (y and z, see Figure 4.2).



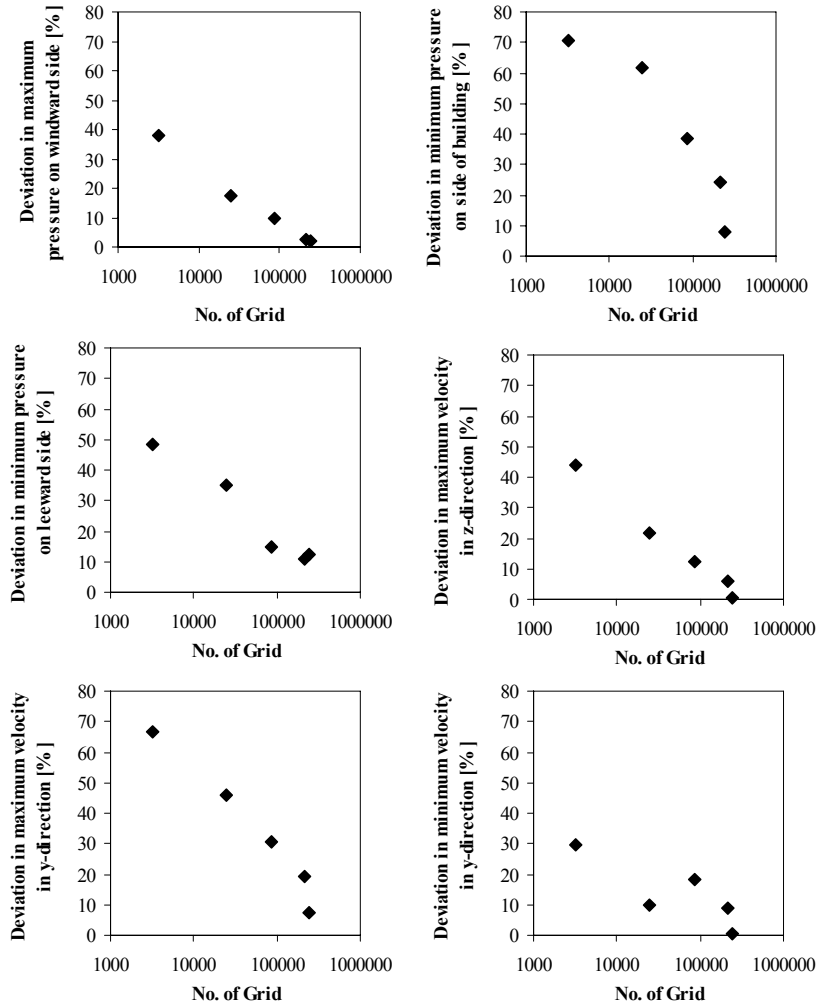


**Figure 4.4 Comparison of the deviance of different factors vs. the number of grid. All values are compared to the value found from the simulation using 630000 grid points (and from this the deviance is found).**

All factors are approaching a constant value at high grid numbers, however the solution seems not to be completely grid independent even at large grid numbers. The grid which has been adapted to the pressure gradient show

however only a deviance of a few percent for most of the factors, and a denser grid close to the leeward and parallel sides of the building could compensate for the pressure deviance being too high in these areas, therefore a grid of approximately 600000 cells is used for the domain surrounding the building in combination with a solution adaptive grid refinement.

#### *4.3.2. BOUNDARY CONDITIONS*

A complete numerical description of the wind tunnel (see chapter 3) used for the measurements described in chapter 5 and 6 will require a too high computational cost compared to what is gained. However a numerical description of some part of the wind tunnel upstream as well as downstream is required. As mentioned in chapter 2 the pressure has a built-up region which is approximately 5 times the height of the building. In this section the length of the modelled wind tunnel up- and downstream of the model described in chapter 6 will be analysed. The results are compared to the measurements of the surface pressure distribution on the building and the obtained velocity profile at a distance upstream of the building. In all cases the approximated velocity profile is applied at the inlet and a roughness height of 0.07 m is used. This value corresponds to the height of the roughness elements in the real wind tunnel. Figure 4.5 shows the pressure distribution in the flow direction on a centreline compared to the building for 4 different representations of the wind tunnel.

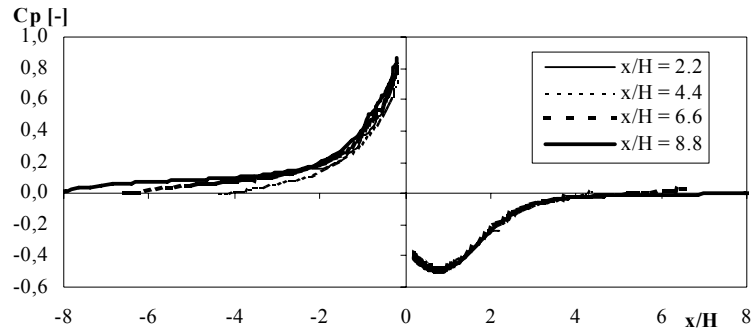


**Figure 4.5 Pressure distribution on centreline for different modelled wind tunnel lengths.**

The found pressure distribution is approximately the same for all representations of the wind tunnel, however small differences are found upstream of the building. The stagnation pressure is highest for the longest modelled wind tunnel, this may however be due to an altered representation of the velocity profile due to an incorrect roughness. The three larger cases show a pressure distribution starting and ending in 0 and therefore the modelled length is chosen to be  $x/H = 4.4$ .

Figure 4.6 shows that none of the simulations agree with the pressure distribution on the windward side of the building, which may be due to the chosen turbulence model. This will be analysed in the following section.

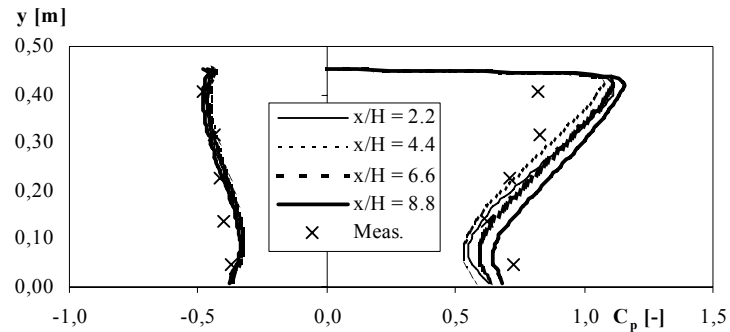


**Figure 4.6 Vertical surface pressure distribution in the middle of the building.**

#### 4.3.3. TURBULENCE MODELS

The previous part of the analysis have been carried out using the standard  $k-\epsilon$  model, but the grid dependency may very well also depend on the choice of turbulence model. The grid dependency of different turbulence models has not been investigated, but a solution adaptive grid has been used in the following analysis (using grid no. 3 mentioned in section 4.3.1 as the initial mesh).

The simulations are compared to the measured surface pressure distribution on the model building in the same way as in the previous section. Four different turbulence models have been applied; the standard  $k-\epsilon$ , the “realizable”  $k-\epsilon$  model, the RNG based  $k-\epsilon$  and the Reynolds stress model. Figure 4.7 and Figure 4.8 shows the predicted surface pressure distribution compared to corresponding measured values. Figure 4.7 shows that all models deviate from the measured pressure distribution on the windward side of the building, but while the Realisable and the RNG based  $k-\epsilon$  models and the Reynolds stress model show similar patterns compared to the measured values the standard  $k-\epsilon$  model show a large deviation. None of the turbulence models seem to be able to give a completely accurate description of the wind side pressure, this may however be due to an incorrect description of the boundary conditions.

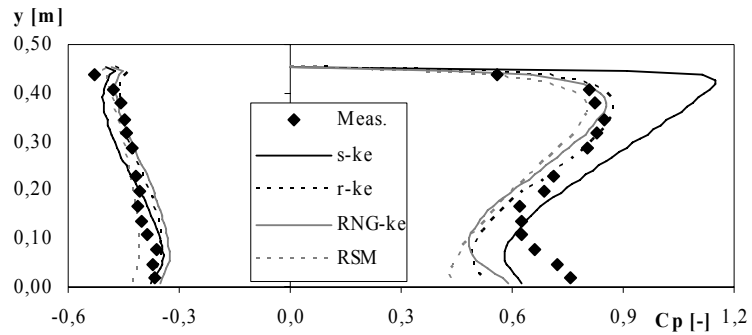


**Figure 4.7 Vertical surface pressure distribution in the middle of the building.**

Apart from the standard  $k-\varepsilon$  model the turbulence models seem to predict the pressure distribution with an almost equal accuracy and the choice of turbulence model is therefore not as evident as could have been hoped for. However since the Reynolds stress model is more expensive (7 more partial differential equations needs to be solved) than the other two it is disregarded. The RNG based  $k-\varepsilon$  model is chosen since it shows the best general correspondence and the horizontal pressure distribution in  $y = 0.4075$  m does not deviate at the sides, which is the case for the realisable  $k-\varepsilon$  model.

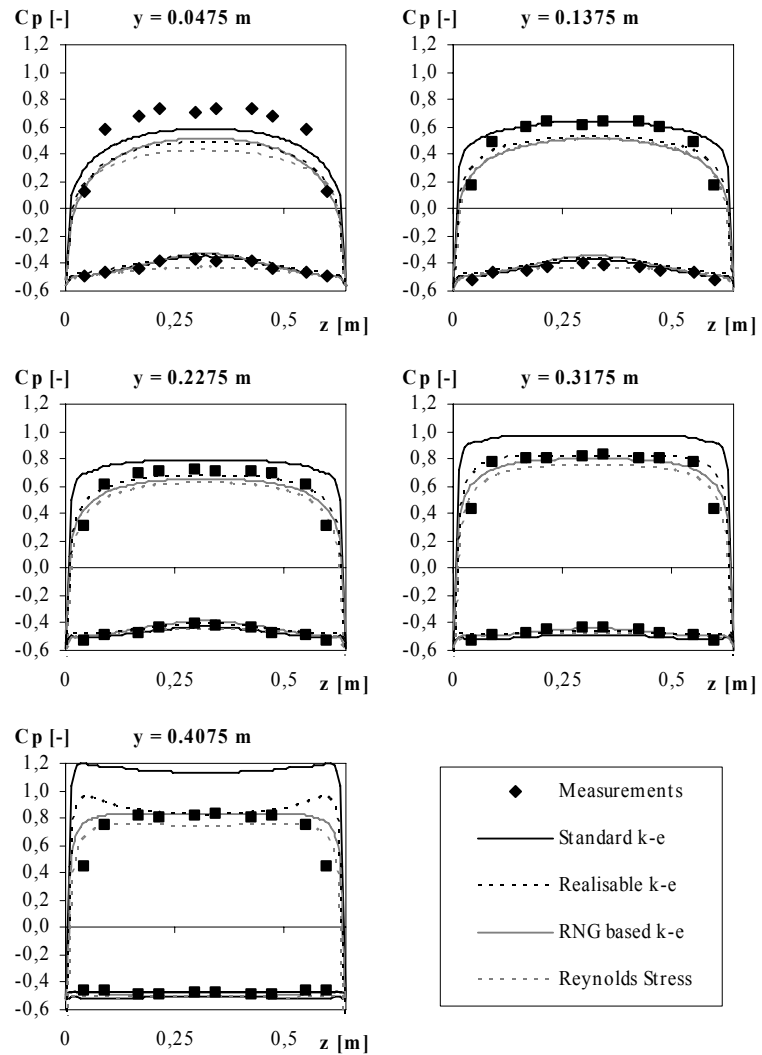


Figure 4.8 Horizontal pressure distribution in five different heights. Predictions and measurements

## **5. EXPERIMENTAL AND NUMERICAL ANALYSIS OF SIMPLIFIED CROSS-FLOW BUILDING MODEL**

As previously mentioned the airflow through building envelope openings is a complex topic and difficult to give a complete description of. Many variables influence the airflow through building openings and therefore some simple geometrical models have been analysed. In order to eliminate some of the complexity an analysis is carried out using well-defined geometrical shapes in an isothermal uniform free flow.

The analysis take a starting point in a circular disk placed in a free stream with or without an opening placed in the centre of the disk. The analysis is subsequently extended with openings placed eccentrically in the disk, as well as expanding the disk to form a cylinder in the downstream direction.

The analysis includes measurements of the surface pressure and velocity measurements in the openings, as well as predictions using CFD. The CFD results were also used as a mean of comparison.

The measurements have been conducted in a wind tunnel where the models were placed on wires in the free stream. The first series of measurements were carried out by L. Claesson and M. Sandberg at the University of Gävle and are reported in (Sandberg, 2001), and the second part were conducted by the present author in association with Claesson and Sandberg also in Gävle.

Sandberg stated the initial problem of the analysis:

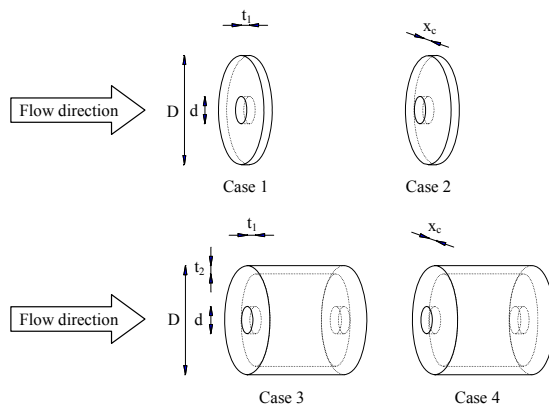
When can the recorded pressure distribution (surface pressure coefficients) obtained from a sealed object be used to predict the airflow rate through openings placed in the same object?

The objective of the analysis is to explore the pressure distribution on geometrically simple objects in order to obtain understanding of the parameters, which govern the pressure distribution.

The analysis of these simple models were also a part of the IEA Annex 35 programme on "Airflow through large openings", and is reported in (Sandberg 2001, 2002a), (Jensen True et al., 2001, 2002), (Rösler, 2001) and (Fracastoro and Perino, 2001).

### 5.1. GEOMETRY OF THE MODELS

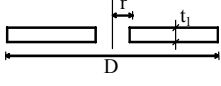
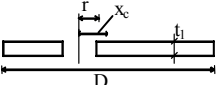
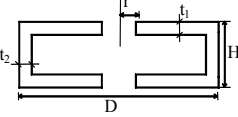
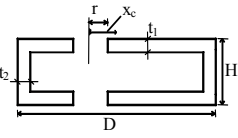
The geometrical shapes used in the analysis are depicted in Figure 5.1. The models are numbered cases 1-4. Case 1 is a flat circular disk with or without an opening placed in the centre. Case 2 is the same except the openings are placed off centre. Cases 3 and 4 are similar to cases 1 and 2 except cylinders replace the disks.



**Figure 5.1** Illustration of the models used in the wind tunnel investigation.

The dimensions of the geometrical shapes analysed in the wind tunnel investigation are shown in Table 5.1.



Name	Sketch	$t_1/t_2$ [mm]	$r$ [mm]	$H$ [mm]	$x_c$	$v_w$ [m/s]
Case 1		10	0, 3.75, 5, 8, 17.5, 27.5 and 37.5	-	0	18,5
Case 2		10	3.75, 5, 8 and 17.5	-	15	17,5
Case 3		8/10	0, 3.75, 5, 8, 17.5, 27.5 and 37.5	160	0	17,5
Case 4		8/10	3.75, 5, 8 and 17.5	160	15	17,5

**Table 5.1 Dimensions of the models used in the analysis.**

Six different opening sizes are used, with a porosity varying from 0.25 % to 25 %. Regarding case 3 the first series of measurements were carried out using equal upstream and downstream opening sizes (or in- and outlet sizes). The experiments were subsequently expanded with measurements of different up- and downstream opening sizes.

Table 5.2 shows some parameters related to the size of the opening.

<i>Radius of hole [mm]</i>	<i>Porosity [%]</i>	<i>t/D<sub>h</sub> [-]</i>	<i>Re<sub>D</sub> [-]</i>	<i>Friction parameter [-]</i>
0	0.00	-	-	-
3.75	0.25	1.33	8675	0.043
5	0.44	1	11566	0.029
8	1.14	0.63	18506	0.016
17.5	5.44	0.29	40493	0.00626
27.5	13.4	0.18	63615	0.00360
37.5	25.0	0.13	1. 6748	0.00247

**Table 5.2 Parameters related to the size of the holes.**

The friction parameter is the friction against the sides of the hole, and has been calculated as:

$$f = \frac{0.316}{Re^{0.25}} \frac{t}{D} \quad (\text{Equation 5.1})$$

The friction parameter is much less than one and it is therefore concluded that the effect of the surface friction can be neglected.

## 5.2. EXPERIMENTAL SET-UP

The models were firmly stretched out on wires in the middle of the wind tunnel as to be hanging in the uniform free flow and not be influenced by any near-wall effects.

The location of the pressure tabs in the circular disk is shown in the small inset in Figure 5.2. The pressure tubes were 1.5 mm thick, and placed so that they would have as little an influence on the flow as possible.

Figure 5.2 and Figure 5.3 shows the disk and the cylinder placed in the wind tunnel.



**Figure 5.2** Wind tunnel and the circular disk.

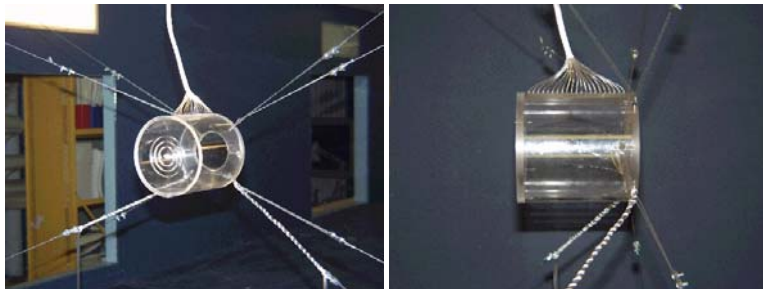


**Figure 5.3** The cylinder (case 3) with the pressure tubes measuring the inside pressure.

In order to obtain knowledge of the airflow through the objects the velocity was measured in the vicinity of the openings. This was done with a hot wire anemometer placed in multiple locations in order to retrieve the velocity profile in the openings.

### 5.2.1. MEASUREMENT SERIES

A graphical description of the opening configurations is depicted in Figure 5.4 for the cylinder (case 3) and with indication of the used configuration for cases 1, 2 and 4. The indication of both an inlet and outlet porosity for the disks (case 1 and 2) may be misleading since there is only one opening.

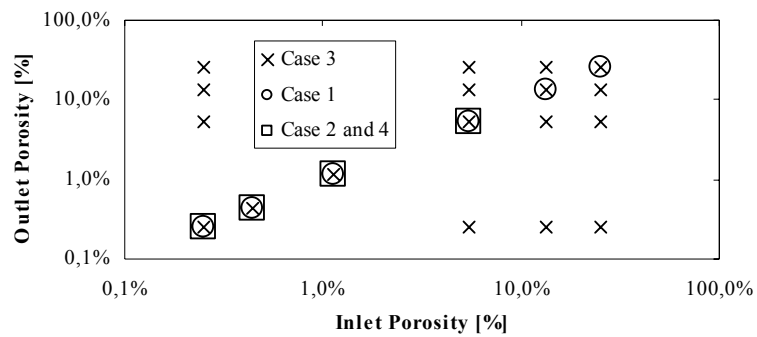


**Figure 5.4 Graphical description of the configurations used in the measurements.**

The pressure is measured on both front and rear sides (see Figure 5.3) of all cases for all configurations and the internal pressure is measured for all configurations using case 3. The velocity distribution is only measured for cases 1 and 3.

### 5.3. COMPUTATIONAL FLUID DYNAMICS

In the analysis the CFD code Fluent™ 5.4 was used for all predictions, and the grid was generated in the parallel pre-processing programme Gambit 1.3.

For all situations the flow was 3 dimensional, steady state and turbulent. A Reynolds stress turbulence model was used for the predictions since the standard k-ε was found to lead to physically unrealistic results (Jensen et al 2002), which will also be shown in the next section.

Symmetry planes have been used where possible e.g. 2 symmetry planes have been used for both Case 1 and 3, while only 1 has been used for Case 2 and 4, see Figure 5.5. For the sake of simplicity the modelled disk is placed in the middle of a round channel despite of the rectangular wind tunnel. The modelled channel is 2 m long and has a diameter of 3 m (equal to the width of the wind tunnel), see Figure 5.5.

A structured hexahedral grid was used in the predictions. The number of grid points were adjusted to fit the specific case but all prediction had approximately 140 cells in the x direction, 70 cells in both the y- and the z-direction and 30 cells on the round boundary.

A first order upwind discretisation scheme was used in combination with the SIMPLE pressure-velocity-coupling algorithm.

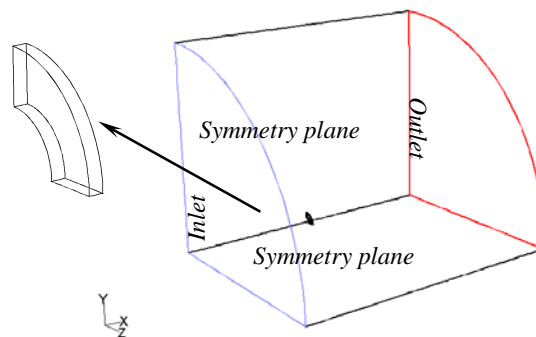


**Figure 5.5 Geometrical layout of the modelled disk (Case 1 with a hole radius of 37.5 mm).**

## 5.4. RESULTS

Results have been obtained from both measurements and predictions and these will be compared simultaneously (where available) in the following analysis.

As mentioned earlier the standard  $k-\epsilon$  model has been found to lead to physically unrealistic surface pressures. Figure 5.6 shows the distribution of the surface pressure coefficients of Case 1 (see Table 5.1) found from measurements as well as predictions using both the standard  $k-\epsilon$  model and the Reynolds stress model. The depiction shows case 1 both with and without an opening placed in the disk.

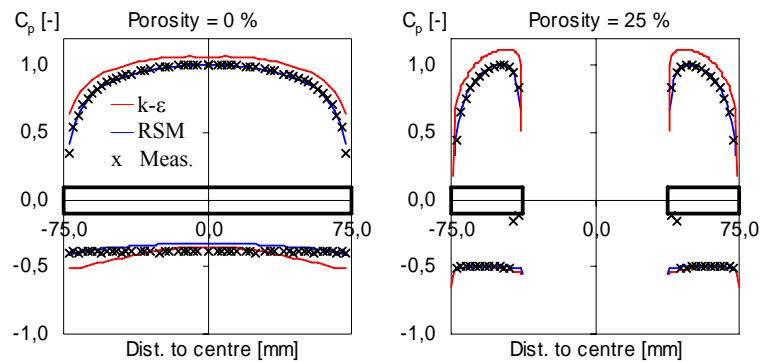


**Figure 5.6 Surface pressure distribution shown for measurements and predictions using the standard  $k-\epsilon$  model and the Reynolds stress model.**

The  $k-\epsilon$  model overestimates the surface pressure on the windward side by a factor of approximately 1.1, whereas the pressures on the leeward side are approximately identical. This discrepancy is caused by the isotropic description of turbulence in the standard  $k-\epsilon$  model. This can be compensated by using an anisotropic version of the  $k-\epsilon$  turbulence model. Fluent contains the option of using a so called “Realisable”  $k-\epsilon$  model (see Shih et al., 1995 and Fluent, 1998), which includes a different model equation for  $\epsilon$ , based upon the dynamic equation of the mean square vorticity fluctuation, taking the anisotropy of the vorticity into account. Another way of compensating for the anisotropy is to use a Reynolds stress model which has been chosen in the following.

#### 5.4.1. VELOCITY DISTRIBUTION AND AIRFLOW PATTERN

The airflow pattern in and around the objects will mainly be discussed based upon the numerical predictions since only the velocity distribution in one opening was determined in the measurements. Terms such as the *Retardment area* and *Catchment area* introduced by Sandberg (see Sandberg, 2002b) will be used in the analysis of the airflow pattern.

Figure 5.7 shows the dividing streamlines and the velocity distribution in the openings of cases 1 and 3 with a porosity of 13,4 %.

The *catchment area* ( $A_c$ ), the *retardment area* ( $A_r$ ) and the *vena contracta* ( $A_{vc}$ ) are shown in Figure 7. The catchment area contains the streamlines in the undisturbed flow upwind passing through the opening.

By using the catchment area the flow rate can be expressed as

$$q = A_c U_0 \quad (\text{Equation 5.2})$$

The retardment area is the area corresponding to the circle of radius  $r_s$  containing points on the front plate with stagnation pressure, see the inset in the upper figure (see also the surface pressure distribution in Figure 5.7).

The disk (case 1) seems to have a larger impact on the flow since the diversion of the outer streamline is bigger. This corresponds with the fact that the drag caused by a cylinder is less than the drag caused by a disk of the same diameter or as in this case a ring (Hoerner 1965).

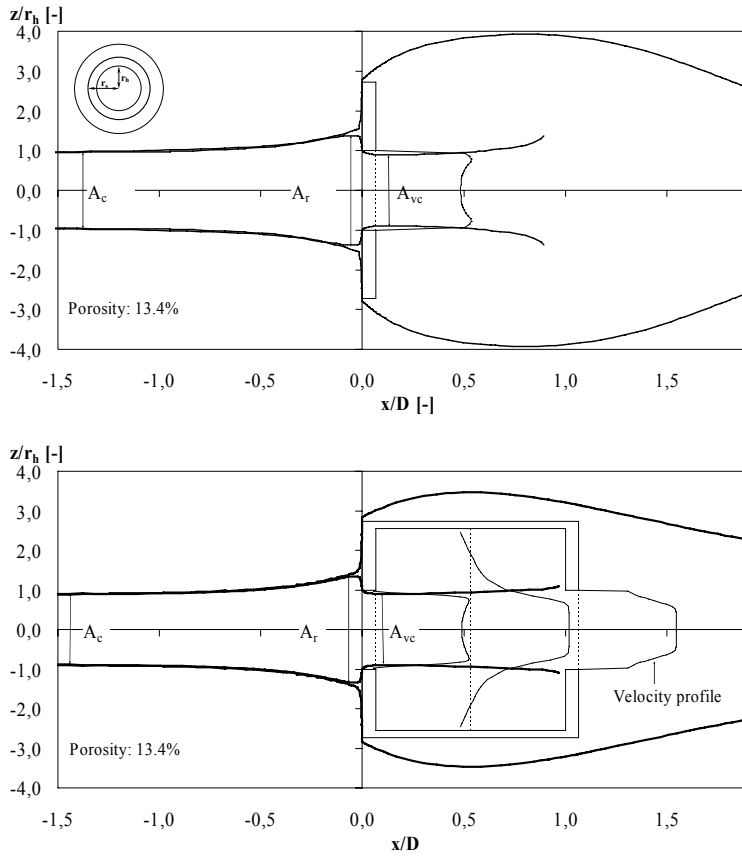


**Figure 5.7** Dividing streamlines and velocity distribution for cases 1 and 3. The velocity profiles for case 3 are depicted in the openings and in the middle of the cylinder.

Similar airflow patterns can be found for other opening sizes, and in order to compare these, relative values of the catchment and retardment areas will be used as well as relative velocity profiles in the openings.

The corresponding streamline distribution is shown for cases 2 and 4 in Figure 5.8.



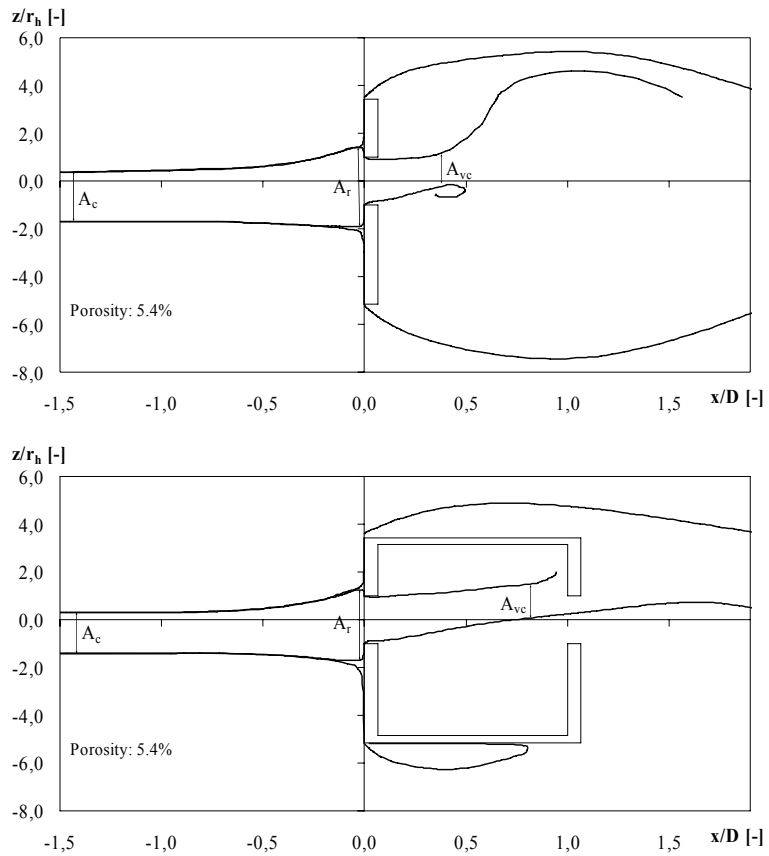


**Figure 5.8** Dividing streamlines for cases 2 and 4 with a porosity of 5.4%.

Figure 5.8 clearly shows the influence of the eccentrically placed opening on the streamline distribution. The streamlines downstream are distorted in the direction in which the opening is placed. The figure also shows that the contraction is moved further downstream of the opening.

Figure 5.9 shows the relative velocity profile in the opening on the rear side of the disk (case 1). Only the predictions of the cases where measurements have been carried out are depicted. The depiction shows a good

correspondence between the measurements and the simulations, and velocity profiles for the three larger openings which have a similar pattern.

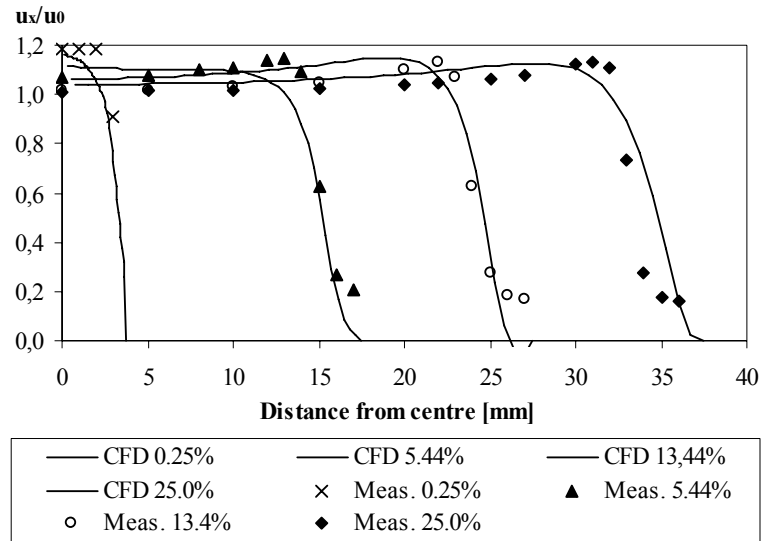
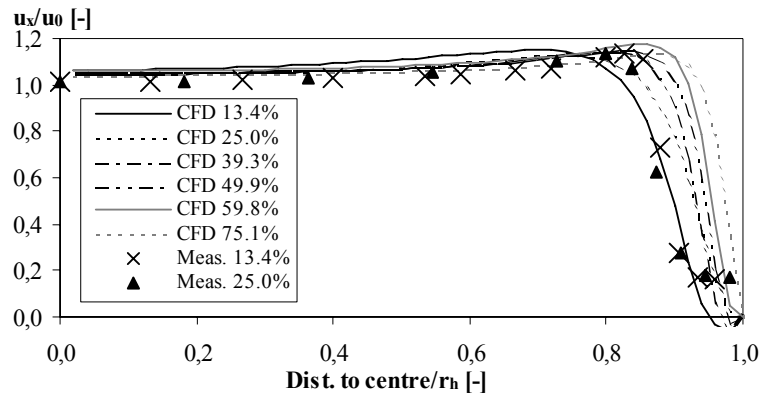


Figure 5.9 Velocity distribution on the rear side of the disk (Case 1).

This similarity in the velocity profile can be illustrated by depicting the relative velocities as a function of the relative distance to the centre (related to the opening size). Figure 5.10 shows this relation for predictions of case 1 with porosities between 13.4% and 75.0%.



**Figure 5.10** Relative velocity profile on the rear side of the disk (case 1) vs. relative distance to the centre.

In the same way cases 2, 3 and 4 can be shown to have almost self-similar velocity profiles.

Figure 5.11 shows the velocity profiles for all 4 cases with a porosity of 25%.

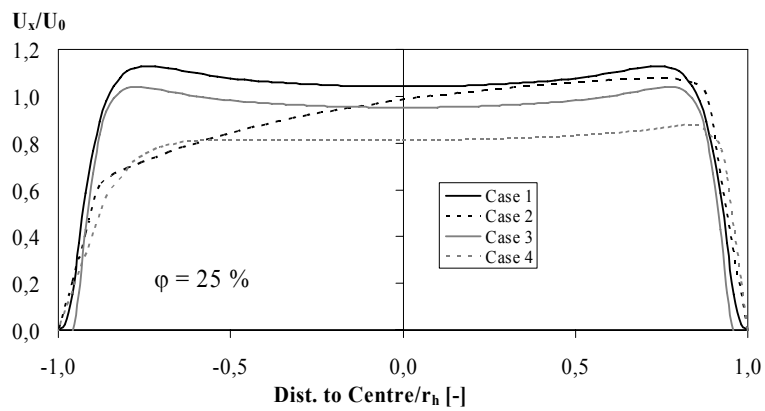


**Figure 5.11** Average velocity profiles for the 4 cases. Found on the rear side of case 1 and 2, and on the rear side of the first plate of case 3 and 4.

Comparing the velocity profiles it is clear that the velocity level is higher in the case of the disk than it is in the cylinder. Also the eccentricity has an impact on the velocity, for the disk (case 2) the profile is “distorted” and in both case 2 and 4 the velocity is lower than for the corresponding symmetrical cases 1 and 3.

Figure 5.12 shows the catchment area as described in (Sandberg, 2002) as well as shown in Figure 5.7.

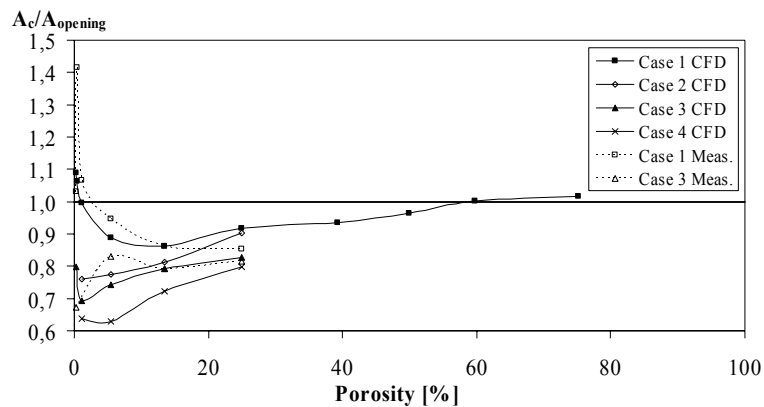


**Figure 5.12 Relative catchment area vs. porosity for cases 1 – 4 (CFD) and 1 and 3 (measurements).**

The catchment area is clearly dependent upon the porosity. The ratio ( $A_c/A_{opening}$ ) should reach a value of 1 at a porosity of 100%, but for case 1 it obtains a value of 1 at a porosity of 60%, this can be due to the constricted domain area in the prediction.

The catchment area ratio exceeds 1 at small porosities and reaches a minimum at porosity of 5-15%.

Figure 5.13 shows the ratio between the retardment area and the opening area as a function of the porosity. In the next section the pressure distributions on the windward side will be shown to have approximately

identical curves independently of the opening size if depicted as functions of a relative distance  $((r-r_h)/(R-r_h))$ . Therefore the relative point of stagnation pressure should be approximately constant and the retardment area can be substituted by a function of the opening size:

$$A_r = \pi \cdot r_s^2 = \pi \cdot (c(R - r_h) + r_h)^2 \quad (\text{Equation 5.3})$$

Despite the collapse of the pressure distribution curves (see Figure 5.15), the relative location of stagnation pressure seems not to be constant. The best approximation is  $c = 1.5 \cdot (r_h)^{0.5}$  which has been included in Figure 5.13. The values of case 1 seem asymptotically to go towards 1, which again is the value that should be reached at a porosity of 100%. At porosities below 10% the retardment area ratio (for case 1 and 2) becomes very large. Except for differences for the smaller openings all 4 cases approximately follow the same pattern having high values at small openings and going towards 1 for the higher porosities.

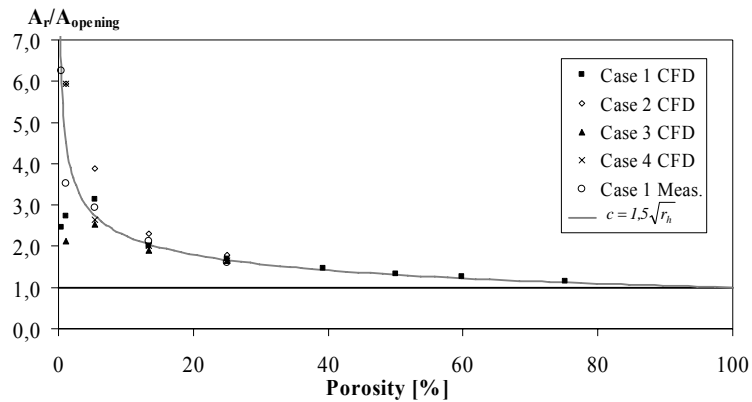
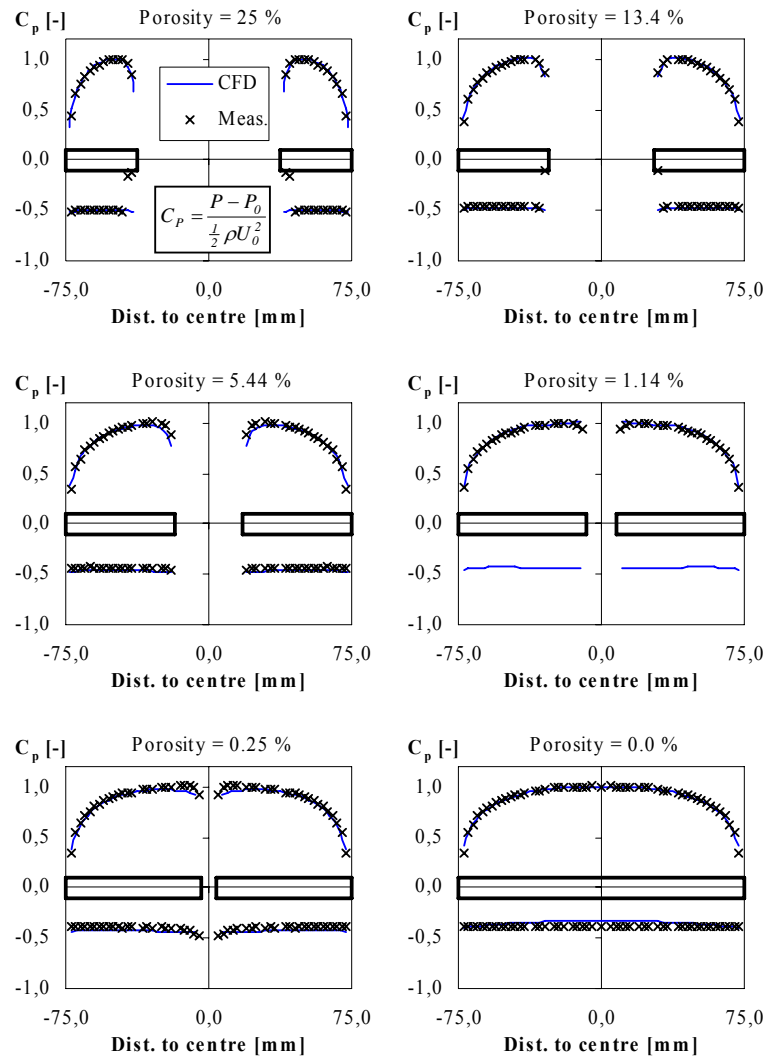


Figure 5.13 Retardment area vs. porosity for cases 1-4 (CFD).

#### 5.4.2. *PRESSURE DISTRIBUTION*

##### **Surface pressure distribution**

Figure 5.14 shows the measured and the predicted pressure distribution on the wind- and leeward side of the disk (case 1). The pressure reaches a maximum at the *stagnation point* on the front side of the disk, which is equal to the radius of the *retardment area*. For all cases a good correspondence is found between the measurements and the predictions.



**Figure 5.14 Pressure distribution on windward and leeward side of disk (case 1) for predictions and measurements.**

The pressure distribution on the windward side seems to be independent of the downstream conditions, since the pressure distribution of the cylinder

(Case 3) is identical to that of the disk (case 1), and likewise with case 2 and 4. By depicting the pressure distribution as a function of the non-dimensional distance  $(r-r_h)/(R-r_h)$  the pressure distributions on the windward side coincides regardless of the porosity, see Figure 5.15. Only measured values are included in the figure since the predictions show values that are almost identical. In the same way the pressure distributions on the windward side for the cases 3 and 4 will coincide.

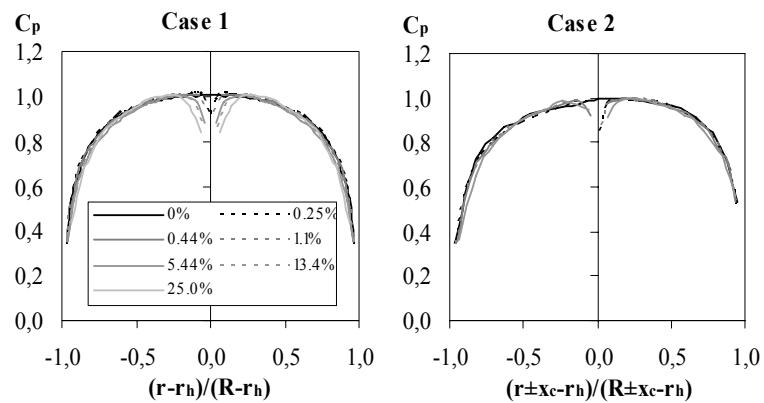


**Figure 5.15 Measured pressure distribution on windward side of Case 1 and 2 vs. the non-dimensional distance.**

The pressure distribution on the leeward side is more uniform than it is on the windward side for case 1 and 3 (see Figure 5.16 and Figure 5.14). However the magnitude of the pressure is not completely independent of the porosity as is the case on the windward side. In addition to this the pressure distribution on the leeward side is not identical for case 1 and 3 (as well as 2 and 4), which can also be deduced from Figure 5.17, which shows the maximum surface pressure difference for case 1 and 3.



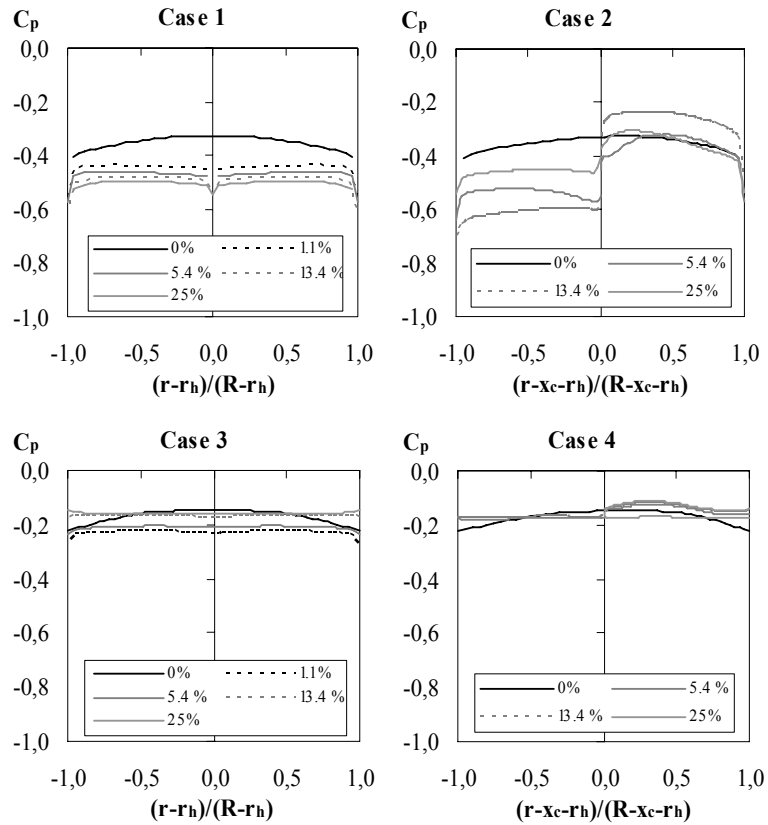


**Figure 5.16 Predicted pressure distribution on the leeward side for cases 1-4 as functions of the relative distance.**

The pressure on the leeward side for case 2 is clearly influenced by the eccentrically placed opening, the same can only to a very small extent be said about case 4. It is clear that the cylinder dampens the influence of the eccentricity.

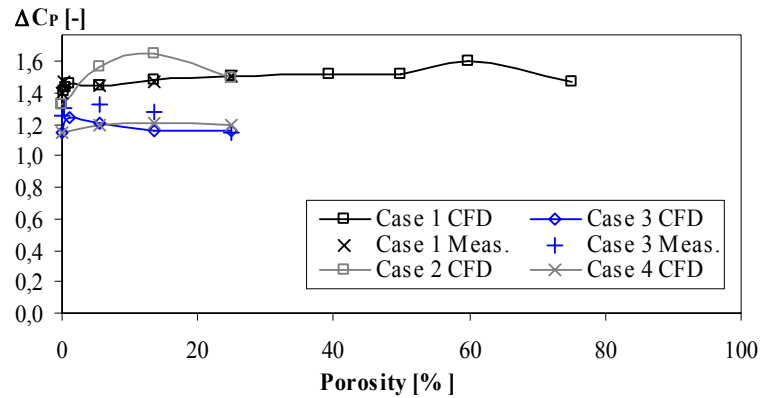


**Figure 5.17 Maximum surface pressure difference between front and back of the disk (Case 1) and the cylinder (Case 3).**

The measured and the predicted values of case 1 are almost identical, however differences can be observed for case 3. The pressure difference is approximately constant for the two cases. The influence of the eccentrically placed opening is diminished in the cylinder case since case 3 and 4 are almost identical. The influence is however obvious in the disk case where the distorted flow in the cylinder causes a non-uniform pressure distribution on the leeward side and hereby a higher maximum pressure difference across the disk. At the highest porosity the maximum pressure difference across case 2 is the same as case 1 since the larger opening reduces the influence of the eccentricity.

The driving pressure is, as expected, smaller for the cylinders compared to the disks.

### Centre line pressure

The CFD predictions give an opportunity to investigate pressures that are difficult to measure. Figure 5.18 shows the pressure on the centreline through the disk (Case 1) for different porosities. The pressure peak in front

of the disk corresponds to the position of the retardment area. For the smallest openings the stagnation pressure is almost obtained in this position.

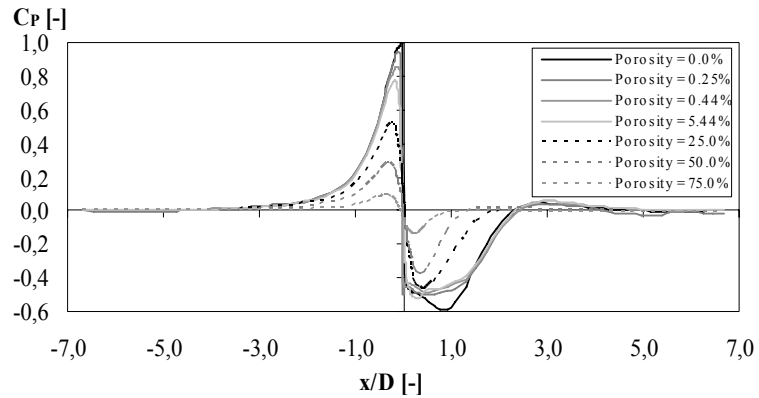


**Figure 5.18 Pressure on centre line for various porosities (case 1).**

The pressure decreases with increasing opening size. Especially on the windward side of the object the pressure seem to be falling rapidly with the porosity. The decreasing pressure can be seen in Figure 5.19, which shows the maximum pressure difference

( $\Delta P = P_r - P_{vc}$ ) across the centreline as a function of the porosity.

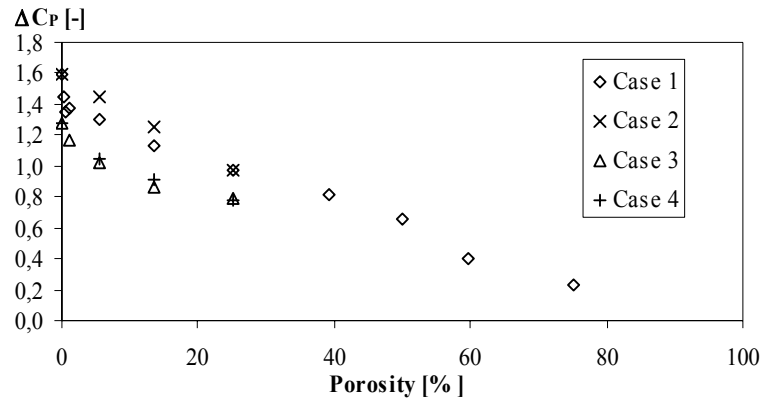


**Figure 5.19 Maximum pressure difference on the centreline for cases 1-4.**

The maximum pressure difference on the centreline for the disk (case 1) is approximately a linear function of the porosity within the range 10-80 %. The eccentricity does not have any significant influence on the maximum pressure difference on the centreline. It should be mentioned that for cases 2 and 4 the centreline does not pass through the centre of the opening but the centre of the disk/cylinder.

### Internal pressure

Complementing the surface pressure measurements on the outside of the cylinder additional measurements have been carried out on the inside, see Figure 5.3.

Figure 5.20 shows the pressure drop through the cylinder (Case 3) for different inlet and outlet opening area ratios.

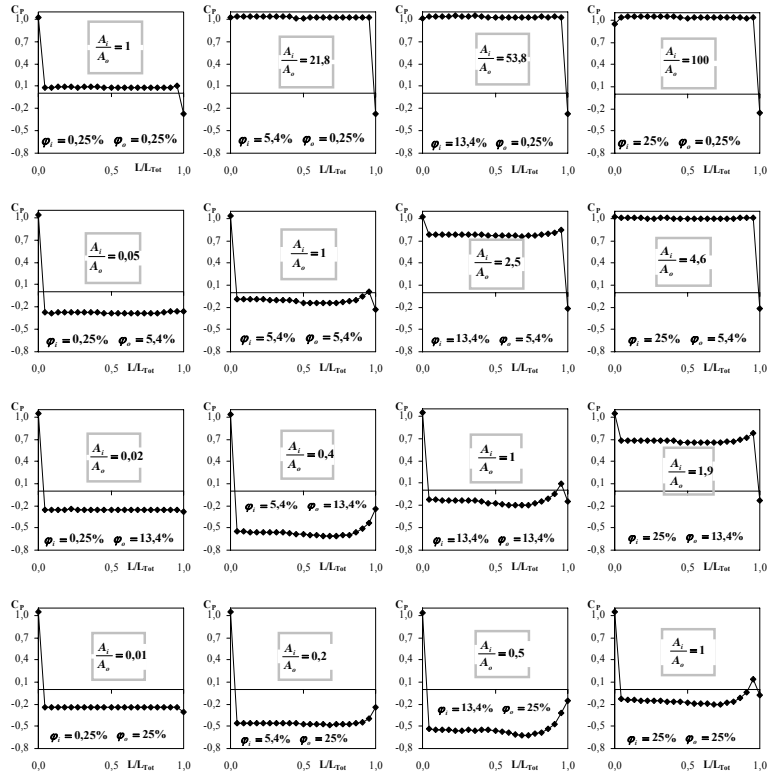


Figure 5.20 Pressure drop through cylinder (Case 3) for 16 different opening area relations.

The top-left depiction in Figure 5.20 shows the pressure drop through the cylinder with small and equal inlet and outlet opening areas. The pressure drop over the outlet opening is half of the difference over the inlet opening. Therefore this is not strictly a crack. The deviation can probably be attributed to there being flow contact between the openings. This is further emphasised by the other three depictions with  $A_i/A_o = 1$  shown diagonally from top left. For these cases almost the whole pressure drop happens across the upwind opening. Depictions of area ratios just above 1 results in the most of the pressure drop happening in the outlet opening. At even

higher area ratios the whole pressure drop happens across the outlet opening. Similarly the opposite is the case for a very small opening area ratio ( $A_{\text{inlet}}/A_{\text{outlet}} \ll 1$ ). Some depictions show a pressure rise across the outlet opening, this is due to a decrease in the velocity across the opening and therefore a rise in the static pressure (since the velocity pressure or dynamic pressure is decreasing).

Figure 5.21 shows the pressure difference across the cylinder and its openings as a function of the opening area ratio. The measured values are compared to approximated curves showing the assumed pattern of the present flow.

The depiction of the pressure difference gives a clear indication of one opening being dominant and only in the vicinity of  $A_{\text{inlet}}/A_{\text{outlet}} = 1$  is there large differences in the pressure drop across the openings. The variation in the values for  $A_{\text{Inlet}}/A_{\text{Outlet}} \approx 1$  is due to the size of the openings and not the relation between them.

At  $A_{\text{inlet}}/A_{\text{outlet}} = 1$  the pressure difference is higher for the inlet opening than it is for the outlet even for the smallest opening size. An explanation for this can be the “shaping” of the flow as it approaches the inlet opening whereas the flow has the “right shape” when it approaches the outlet opening. This also explains that the lines (in the bottom figure) cross at  $A_{\text{inlet}}/A_{\text{outlet}} > 1$ .

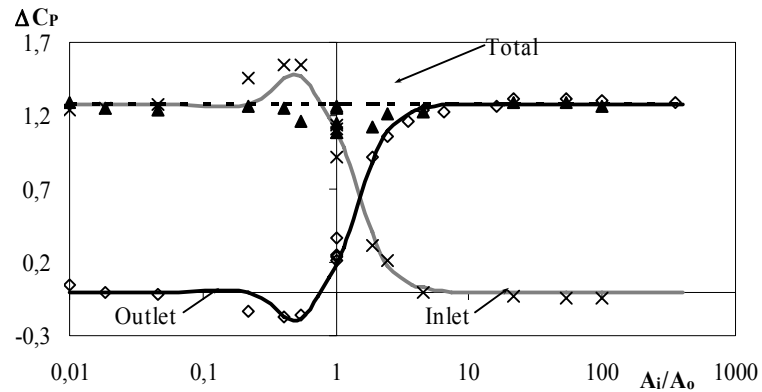


**Figure 5.21** Pressure difference as a function of the inlet and outlet opening area ratio (Case 3).

#### 5.4.3. AIRFLOW RATE

The airflow rate is compared by means of a traditional discharge coefficient based on the surface pressures (see equation 1.2). This is shown in Figure 5.22 for cases 1 and 2 (left depiction) as well as 3 and 4 (right depiction). The depicted  $C_D$  values for the cylinder cases are the total discharge coefficients. The individual values for the upstream and downstream openings are depicted in Figure 5.23 for the 2 cylinder cases.

The discharge coefficient for case 1 and 2 are almost identical, whereas there is a large difference between the obtained values for cases 3 and 4. Apart from a small rise when the porosity approaches 100 % the discharge coefficient for Case 1 seems to obtain a constant value of  $C_D = 0.7$  at high porosities. The same value is obtained for case 3 at high porosities.

The measured  $C_D$  value for case 1 exceeds 1, this can however be due to inaccuracies in the measurements, since it does not exceed 1 in the predictions. Generally the correspondence between measurements and predictions is found to be acceptable.

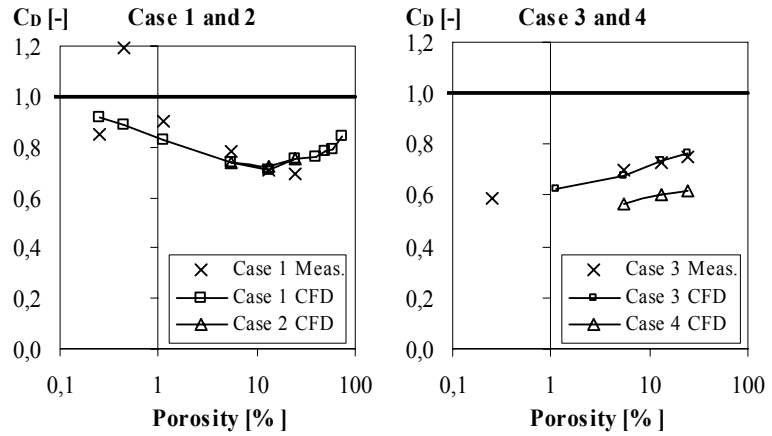


Figure 5.22 Discharge coefficient based on the measurements and predictions as a function of the porosity.

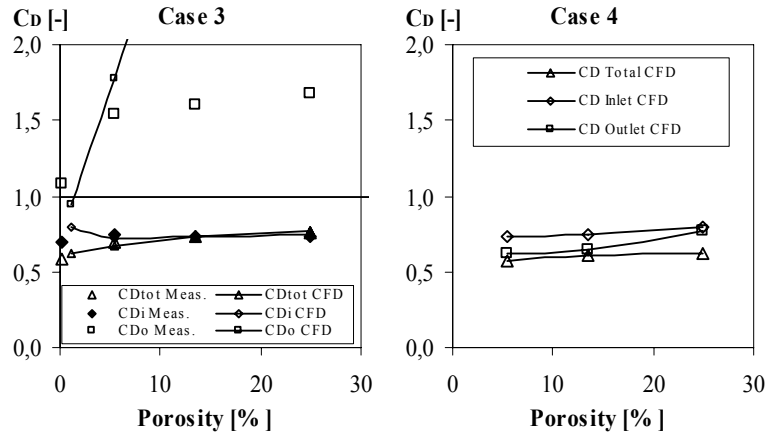


Figure 5.23 Discharge coefficients for case 3 and case 4 from measurements and predictions as a function of the porosity.

The outlet opening of case 3 show values that are much higher than the others, which is due to the much lower pressure difference. Even the smallest opening size obtains a  $C_D$  value that is above 1 (for the



measurements). The corresponding pressure difference across this opening is shown in the top-left depiction of Figure 5.20 and is less than half the value of the inlet opening.

The downstream opening of case 4 is not found to lead to coefficients of the same magnitude as for case 3, this is due to the fact that the jet from the upstream opening impinges on the surface inside the cylinder which influences the pressure inside the cylinder.

If the average pressures found from the sealed objects are applied to the calculation of the discharge coefficient the values depicted in Figure 5.24 are found.

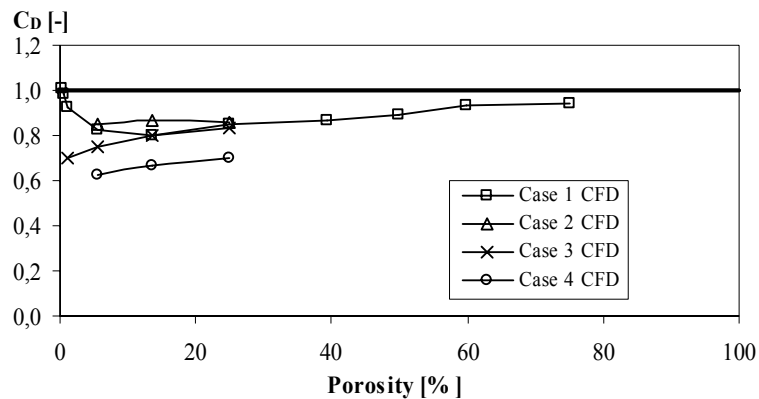


**Figure 5.24 Discharge coefficient based on the average surface pressures found from the sealed objects.**

The difference between the discharge coefficients found from the average values and the ones depicted in Figure 5.22 based on the maximum pressure difference across the objects is 10 – 20 %. The largest difference will occur in the cylinder cases if the pressure difference across the individual opening is assumed to be half the total pressure difference. Applying half the pressure difference to the calculation of the discharge coefficient for the individual openings leads to values that are close to or above 1.

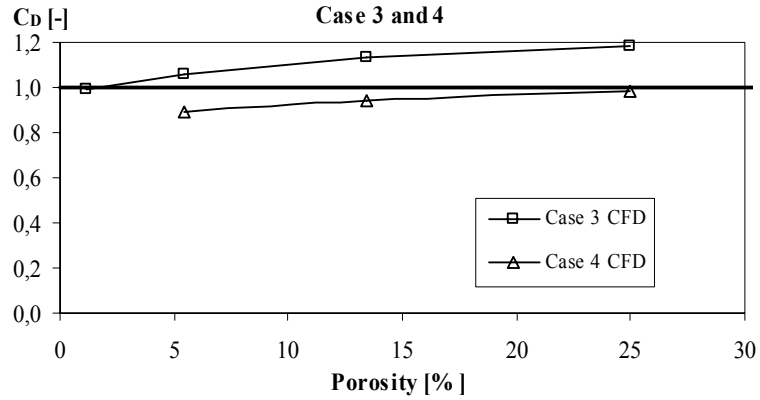


**Figure 5.25 Discharge coefficient for the individual opening in the cylinder cases (3 and 4) based on the pressure difference being identical across the two openings.**

The flow equation (see eq. 1.2) is based on the Bernoulli equation applied to the streamlines of the flow. And by applying the Bernoulli equation on the streamlines between the *retardment area* and the contracted area (the *Vena Contracta*) yields:

$$q = C_D^* \frac{\mu}{\sqrt{1 - \mu^2 (A/A_r)^2}} A \sqrt{\frac{2\Delta P}{\rho}} \quad (\text{Equation 5.4})$$

Where  $\Delta P = (P_r - P_{vc})$

Alternatively we can write

$$q = C_D^* \frac{\mu}{\sqrt{1 - \mu^2 (A/A_c)^2}} A \sqrt{\frac{2\Delta P}{\rho}} \quad (\text{Equation 5.5})$$

Where  $\Delta P = (P_\sigma - P_{vc})$

The above equations are only showing the relations between involved quantities. The presence of the retardment area in the Equation 1.4 and the catchment area in the Equation 1.5 are expressions of the selection procedure. But at present we have no simple independent method of predicting these quantities. By letting the retardement area or the catchment area go to infinity the common flow equation is retrieved (Equation 1.2).

Figure 5.26 shows the flow coefficient  $C_D^*$  as a function of the porosity based on equation 5.4 (Case 1 and 3) and equation 5.5 (Case 1). The calculation of  $C_D^*$  for case 3 has not been included for equation 5.5 since the part  $1 - \mu^2(A/A_c)^2$  becomes negative or close to zero.

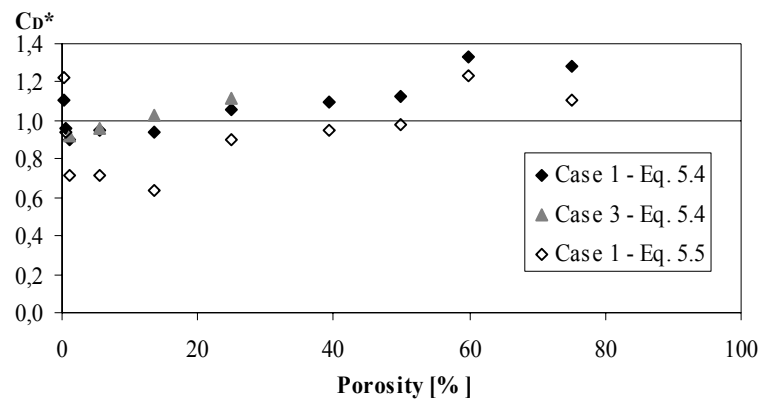


**Figure 5.26 Flow coefficient  $C_D^*$  as a function of the porosity**

The expression mentioned in Figure 5.26 is based on the Bernoulli equation and in an inviscid fluid the only loss is due to the contraction and a value of  $C_D^* = 1$  should be obtained. Therefore there seems to be an error in both expressions since  $C_D^*$  exceeds 1 for most of the points for equation 5.4 and are very deviant for equation 5.5. Many of the values are however close to 1, but there seems to be some discrepancy especially at high porosities. It should be mentioned that the pressures used are the ones found on the centreline and that these may deviate from pressures representing the whole flow tube.

In connection to Figure 5.26 it should also be noted that the contraction coefficients ( $\mu$ ) are found from streamlines in the CFD code and are therefore to some extent questionable.

Another way of determining the contraction coefficients ( $\mu$ ) is to use the maximum velocity on the centreline which should be located in the contracted area and according to theory be of the same magnitude across the contracted area. Therefore it should be possible to calculate the contraction coefficient as:

$$\mu = \frac{A_{vc}}{A} = \frac{q/u_{max}}{A}$$

Using the above mentioned definition leads to the  $C_D^*$  values shown in Figure 5.27.

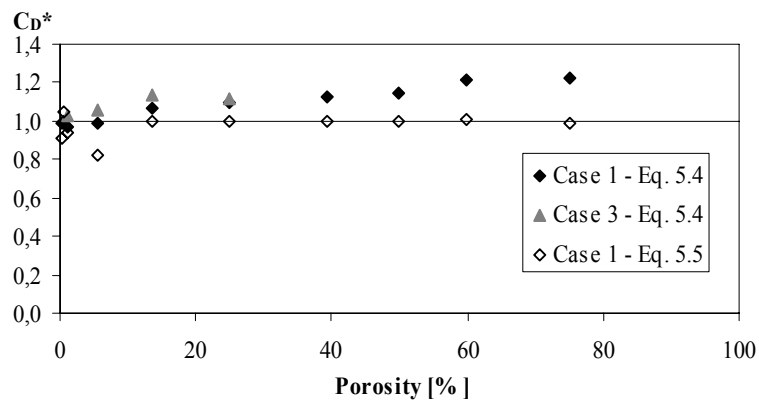


**Figure 5.27 Coefficient  $C_D^*$  as a function of the porosity and calculated based on alternative definition of the contraction coefficient.**

Apart from the values at lower porosities equation 5.5 leads to values that are approximately equal to 1. Equation 5.4 however still show a deviation that seems to increase with the porosity, this indicates that the pressure used for the retardment area is incorrect. This can be adjusted by calculating the pressure as an area weighted average of maximum pressure on the centreline (representing the opening area) and the stagnation pressure (representing the retardment area subtracted the opening area). This leads to the  $C_D^*$  values shown in Figure 5.28.

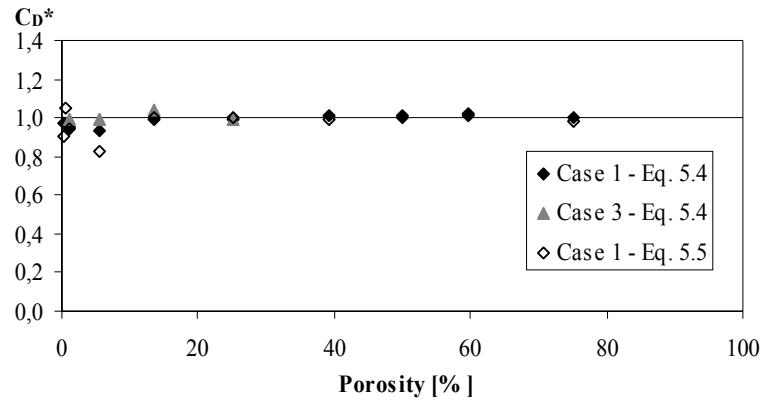


**Figure 5.28**  $C_D^*$  as a function of the porosity and based on an averaged value of the retardment area pressure.

The values shown in Figure 5.28 are apart from slight deviations equal to 1, and it seems that it is possible to calculate the airflow even through large openings with the use of a flow equation based on the Bernoulli equation. It should be emphasized that the approach of using values that fit the specific case is to a certain extent questionable.

If the different contraction coefficients used in the calculations of  $C_D^*$  are compared the deviance can be found. Figure 5.29 shows the used contraction coefficients used in calculation of  $C_D^*$ , as a means of comparison the theoretical contraction coefficients found from pipe flow based on potential flow theory are depicted in the figure (see chapter 2).

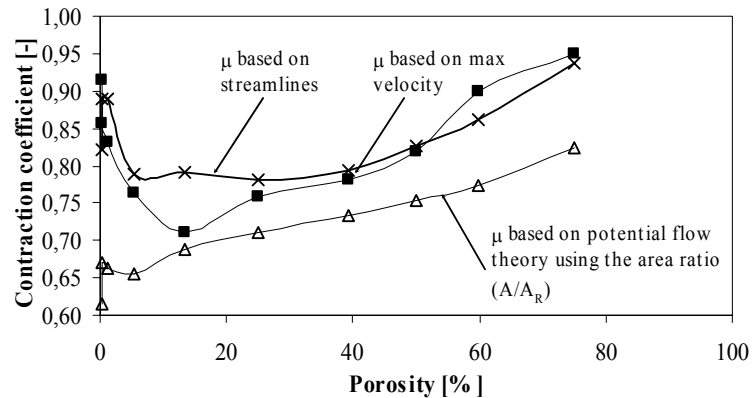


**Figure 5.29** Contraction coefficients used for the calculation of  $C_D^*$  compared to the contraction coefficients found from an orifice placed in a confined flow based on potential flow theory (based on the area ratio of the opening and the retardment area).

From Figure 5.29 it is clear that a small change in the contraction coefficient may result in a large change in  $C_D^*$  since the values of  $\mu$  used in the calculations are (apart from one point) almost identical. The depiction also contains the contraction coefficient calculated as a function of the opening to retardment area ratio (based on potential theory), which results in values that are lower than the used coefficients. This is due to the fact that the values apply to an orifice placed in a confined flow and are based on  $A_{\text{opening}}/A_{\text{pipe}}$  instead of  $A_{\text{opening}}/A_{\text{retardment}}$ . However since the contraction is due to the change in flow direction the correct area may not be the retardment area since the area of the flowtube is smaller ( $A_{\text{catchment}}$ ).

### Unequal opening sizes

The airflow rate has also through the simulations been found for case 3 using different upstream and downstream opening sizes. Figure 5.30 shows the traditional discharge coefficient depicted as a function of the opening area ratio. The figure shows the discharge coefficient for the whole object, the upstream opening as well as the downstream opening.

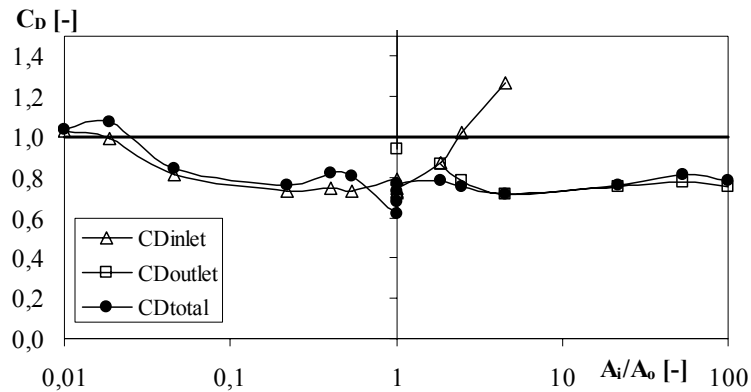


**Figure 5.30 Discharge coefficients for the whole object (total), the upstream opening (inlet) and the downstream opening (outlet) for case 3.**

Figure 5.30 shows that the airflow rate is higher when the upstream opening is smaller than the downstream one (the total pressure difference is almost constant, see Figure 5.21). The reason for this difference is that the smallest opening size is decisive for the airflow rate and when the smaller opening is placed upstream the air will enter the object freely and the generated jet will pass unimpeded through the object, whereas if the smaller opening is placed downstream the flow will be influenced by the limitation of the object (and the upstream opening). The total discharge coefficient is found to be in the interval 0,7 – 1,0 and exceeds 1 at very low  $A_{inlet}/A_{outlet}$  ratios.

The discharge coefficient for the individual opening has not been calculated in a large part of the domain since the surface pressure difference becomes zero or even negative, this seems especially to be a problem for the downstream opening when the upstream opening is smaller ( $A_i/A_o < 1$ ). When  $A_i/A_o > 1$  the discharge coefficient for the downstream opening is calculated for three of the cases where it experiences an increase with increasing area ratio due to the decreasing pressure difference.

As mentioned earlier the airflow rate could be calculated using the catchment area. Figure 5.31 shows the relative catchment area as a function of the opening area ratio.

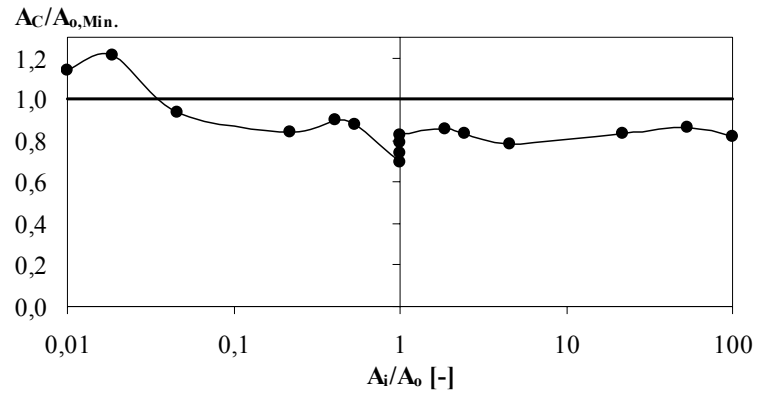


**Figure 5.31 Relative catchment area vs. the opening area ratio.**

The found values of the catchment area experiences a similar pattern as the one found for the total discharge coefficient, which is due to the pressure difference being approximately constant (both are directly proportional to the airflow rate).

Instead of depicting  $C_D^*$  as described by equation 5.4 and 5.5 this is set equal to 1 and the contraction coefficients are retrieved, the found coefficients are shown in Figure 5.32. It should be noted that it is the contraction of the dominant opening (i.e. the smallest opening) that is depicted.

The contraction coefficient is approximately constant except at the two lowest area ratios where it is very close to 1.



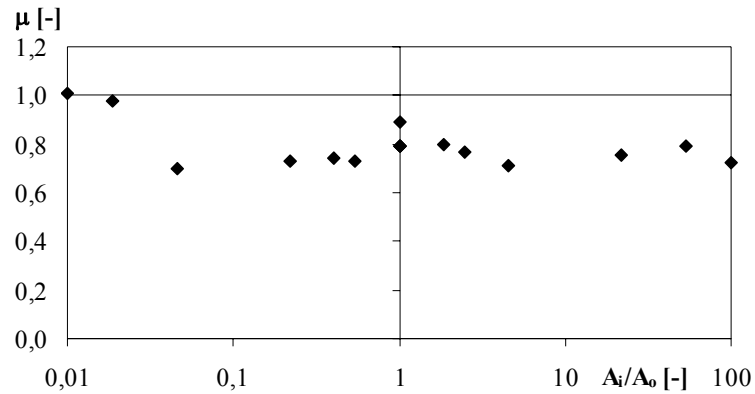


Figure 5.32 Contraction coefficients calculated from equation 5.5 and  $C_D^* = 1$ .

### 5.5. DISCUSSION

The traditional approach of determining the wind driven airflow through building envelope openings is to measure or predict the pressure distribution on the sealed building. In order to calculate the airflow rate through an opening the pressures are applied in the common flow equation (equation 1.2). This approach seems questionable especially when large openings are applied since the pressure distribution can be altered dramatically. The maximum surface pressure difference across the object/building is however found to be approximately of the same magnitude regardless of the porosity. The corresponding discharge coefficients based on the average surface pressures from the sealed objects are also approximately in the expected interval of 0.6 – 1.0.

Another matter of interest is the flow contact that can exist between openings which the traditional flow equation cannot account for since it will lead to unrealistic values of the discharge coefficient.

It is found that the Bernoulli equation is still valid for flow through building openings but that leaving out the opening area to flow tube area ratio may be misleading, and that the preservation of kinetic energy (when flow contact is present) should be included.

Flow through openings is a flow process consisting of a whole sequence of elements; separation from the external flow (selection procedure) – inflow – internal flow – outflow and reuniting with the external flow. Therefore it should be dealt with as a flow problem.

The catchment area is the cross section perpendicular to the wind containing the streamlines in the undisturbed air stream upwind which pass through the building. This area quantifies the selection procedure. The standard equations used for calculating the flow through cracks as a function of a pressure drop is based on the assumption that the catchment area is infinite. The catchment area is dependent on the resistance to the wind offered by the building. The more streamlined the building is the lesser is the flow through the openings.

When one has small openings in a building offering a large resistance to the wind (large drag) the catchment area may be larger than the area of the opening.

If the opening areas are equal then the largest pressure drop occur in the windward opening. With unequal opening areas, the largest pressure occurs across the smallest opening as expected. However, the flow rate is dependent on the order between the openings.

The standard approach is to relate the flow to a pressure difference across the building envelope. A better approach might be to regard the flow through openings as a flow catchment problem. The flow rate is expressed as a reference velocity times the catchment area. Then the result may be conveniently expressed as catchment area divided by the opening area.

## **6. EXPERIMENTAL AND NUMERICAL ANALYSIS OF BUILDING SCALE MODEL**

The pressure distribution on a building surface is subjected to a large variation due to the airflow around the building caused by the wind. The distribution of pressure on a building surface is dependent on the surrounding microclimate as well as the wind direction. The variation of pressure upon a building surface will have an influence on the airflow through an opening placed in the building. The airflow will be dependent on the location of the opening. This can be emphasised by considering the airflow around the sealed building which if the angle of incidence is 0 (the wind being perpendicular to the building surface) will be diverted from the centre and to the sides as well as over the building. This means that placing an opening off centre will cause the airflow through the opening to be non-uniform and hereby the airflow will be influenced.

This chapter contains an analysis of the influence on the airflow through building openings caused by the location of the opening and the wind direction. In addition to these the influence of the opening size and shape is considered.

A building scale model was constructed from plexiglas for analysis purposes in a wind tunnel. The wind tunnel is described in chapter 3. The building was in scale 1:40 and exposed to a wind profile created by roughness elements placed upstream of the building model. Pressure and velocity measurements were carried out on the model for different opening locations and sizes. All measurements were carried out for different wind directions with an interval of 30 degrees.

### **6.1. GEOMETRY OF BUILDING SCALE MODEL**

The building is not a scale model of a real building but a scale model of an idealised building consisting of 5 times 5 identical rooms. The "real" dimensions of the rooms are  $H_{\text{Room}} \times W_{\text{Room}} \times L_{\text{Room}} = 3 \text{ m} \times 4.5 \text{ m} \times 6.75 \text{ m}$  and are scaled 1:40 in the model used in the wind tunnel investigation.

Figure 6.1 shows a sketch of the building model used in the analysis. The total outer dimensions of the model are  $H_{\text{Building}} \times W_{\text{Building}} \times H_{\text{Building}} = 455 \text{ mm} \times 642.5 \text{ mm} \times 189 \text{ mm}$ . The model was constructed as a "shelve" system where the observed room or opening can be moved around in the model while the rest of the front and back of the model is covered with sealed plexiglas plates.

Figure 6.1 shows an outline of the geometry of the building model used in the wind tunnel analysis.

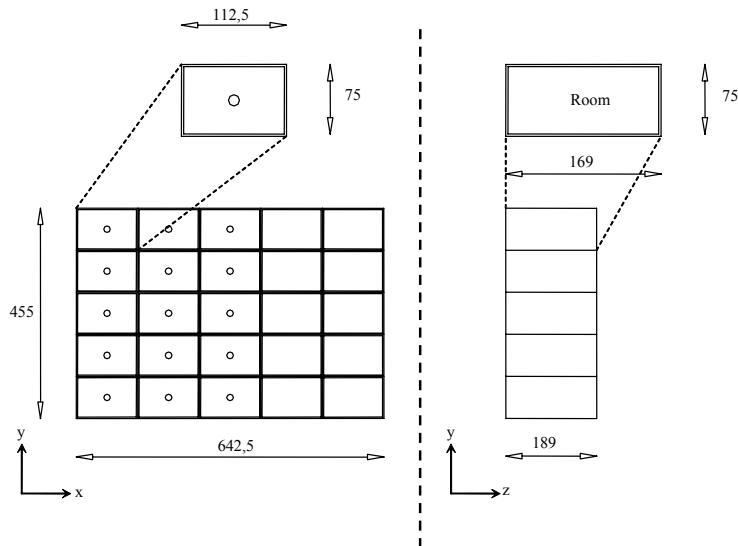


**Figure 6.1 Schematic outline of the building model used in the analysis. All measures in mm's. Measures regarding the whole building are outer dimensions and the measures regarding the room are inner dimensions.**

The investigated opening sizes are shown in the following table, which describes the shape and area of the openings.

Type of opening	Diameter/side [mm]	Area of opening [mm <sup>2</sup> ]
Circular	7.5	44
Circular	10.0	79
Circular	15.0	177
Circular	20.0	314
Quadratic	6.5	42
Quadratic	9.0	81
Quadratic	13.5	182
Quadratic	17.5	306

**Table 6.1 Opening shapes and sizes used in the present analysis.**

The quadratic openings have approximately the same area as the circular ones in order to investigate whether differences are obtained between the shapes. All openings were placed in the centre of the room.

## 6.2. EXPERIMENTAL SET-UP

The measurements were carried out in a tunnel located at the university of Gävle in Sweden. A description of the wind tunnel can be found in chapter 3.

Figure 6.2 shows a picture of the model placed in the wind tunnel as well as the roughness elements creating the wind profile. As mentioned earlier the scale model was constructed as a “shelve” system where the observed room could be moved around in the model in order to investigate the influence of the location of the opening in the building. The rest of the front and back of the building model were covered with Plexiglas plates in order to seal the building, see Figure 6.2.

The model was placed in the centre of a retractable turntable and measurements were conducted for wind incident angles with an interval of 30 degrees (0, 30, 60 ...).



**Figure 6.2** The building model placed in the wind tunnel in Gävle, Sweden.

The wind profile was generated by roughness elements placed upstream of the model in the wind tunnel. The roughness elements consisted of 7 cm times 7 cm cubes placed with a mutual distance of 20 cm.

The experiments included measurements of the surface pressure both on the windward side as well as on the leeward side. Because of the necessity of pressure tubes in connections with these pressure measurements, holes were made on both sides of the observed room. Because the pressure tubes went out the back of the room and down the back of the model it had an influence on the airflow and the pressure distribution. This is however regarded as being small since the pressure tubes were 0.5 mm in width and secured to the model. The pressure was measured in a number of locations vertically and horizontally from the opening. An example of the location of the measuring points is shown in Figure 6.3.

The number of pressure measuring points are more dense closer to the opening since the pressure gradient is expected to be larger in this area.

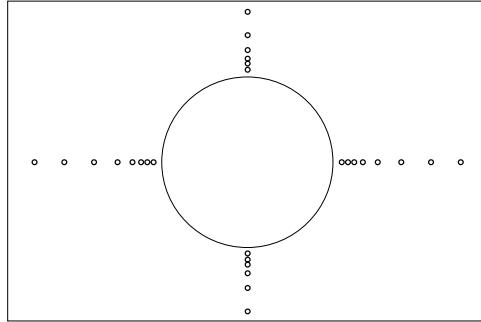


**Figure 6.3 Location of pressure measuring points, shown for an opening size of 314 mm.**

A measuring frequency of 15 Hz for a period of 30 s was used for the pressure measurements.

The reference pressure was measured approximately 1 m upstream and 1 m to the side of the model. However before the model was placed in the wind tunnel the pressure was measured in the middle of the wind tunnel in the height of the building in order to find the correct reference pressure. The used reference could then be compared to the magnitude of this value. Because of the location and the relatively large model compared to the cross sectional area of the wind tunnel the used reference pressure was as high as 30 % higher than the correct reference value. The correctional factor was not constant due to the blockage of the model and the airflow around it was dependent on the angle at which the model was placed in the wind tunnel. The correctional factor varied from 0.76 to 0.83.

Measurements of the velocity were carried out on the leeward side in the immediate vicinity of the opening in order to determine the airflow rate through the openings. The velocity was measured using small hot-wire anemometers in multiple locations in each opening. The number of measured points was dependent on the size of the opening and varied from 5 points for the smallest opening to 13 points for the largest. The sampling frequency was 100 Hz and each measurement were carried out over a period of 30 seconds.

The airflow rates were subsequently calculated by multiplying the velocity measurements with the part of the opening area that these were assumed to represent. Figure 6.4 shows an example of the representative areas used in the calculation of the airflow rates. It should also be noted that a velocity of 0 was assumed at the edge and therefore the outer area was multiplied by 0.

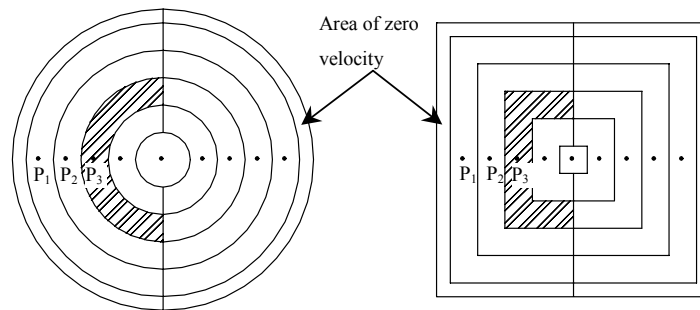


**Figure 6.4 Schematic layout of the representative areas used in the calculation of the airflow rate through the openings.**

This approach may give misleading results since the velocity may be varying with the height and since the location of the measurement points closest to the edges will determine the magnitude of the area of zero velocity.

### 6.3. COMPUTATIONAL FLUID DYNAMICS

The CFD code Fluent™ has been used for the simulations and the grid was generated by the pre processing programme Gambit. A structured hexahedral grid of 600000 cells was applied to all predictions and subsequently the grid was adapted to the pressure gradient ending with a total number of cells of approximately 700000. This value is higher than the necessary grid size found in chapter 4, which is due to the placing of an opening and the room in the model.



For all situations the flow was 3 dimensional, steady state and turbulent. According to chapter 4 the RNG k-e turbulence model was applied due to the lower cost compared to the Reynolds stress model.

Not all the measurements have been reproduced by CFD, only certain situations. Only a square opening of 306 mm<sup>2</sup> has been used in the predictions and it has been limited to 6 predictions with a wind direction of 0 degrees and 9 predictions for the wind directions of 30 and 60 degrees.

## 6.4. RESULTS AND DISCUSSION

The results are analysed from a combination of measurements as well as predictions.

### 6.4.1. WIND PROFILE

The wind profile is depicted in the following Figure 6.5. The velocities have been related to the velocity in the height of the building (Reference velocity) and the height above ground has been related to the height of the building.

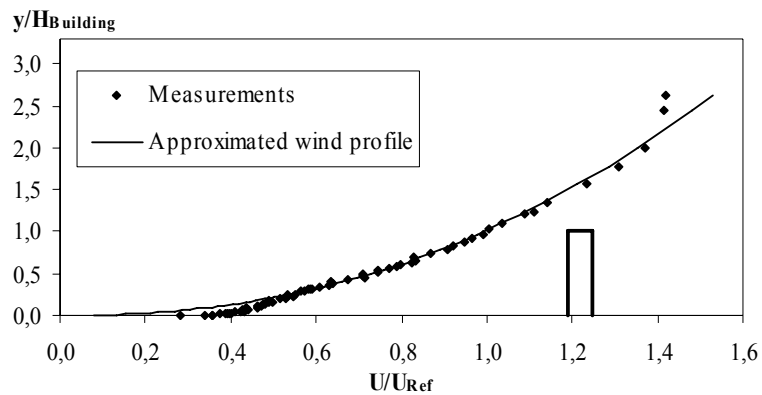


**Figure 6.5** The measured wind profile found by measurements in the wind tunnel.

The wind profile has been approximated by an exponential expression of the form (Andersen et al., 2002):

$$U_h = U_{Ref} \cdot k \cdot h^\alpha \Rightarrow \frac{U_h}{U_{Ref}} = 1.41 \cdot h^{0.445} \quad (\text{Equation 6.1})$$

Figure 6.6 shows the corresponding turbulence intensity in the wind profile found from the velocity measurements. The turbulence intensity is defined as the ratio between the standard deviation (the “root mean square” value) and the mean value.

The turbulence intensity is highest near the ground where it obtains a value of approximately 30%. The influence of the roughness elements is decreasing upwards and the turbulence intensity level is lowered to approximately 5% at the top (it should be mentioned that the ceiling of the wind tunnel is located in  $y/H_{\text{Building}} = 3.3$  and there are no measurements at this level).

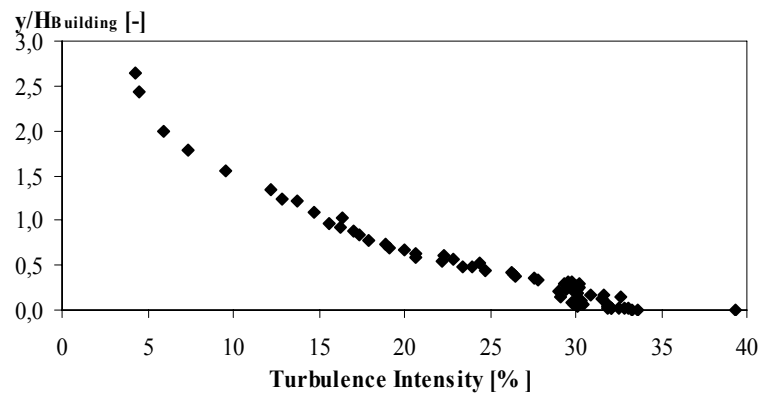


**Figure 6.6** The turbulence intensity of the wind profile in the wind tunnel.

#### 6.4.2. AIRFLOW PATTERN

The airflow pattern will mainly be discussed based on the numerical simulations since the measurements only included surface pressures and

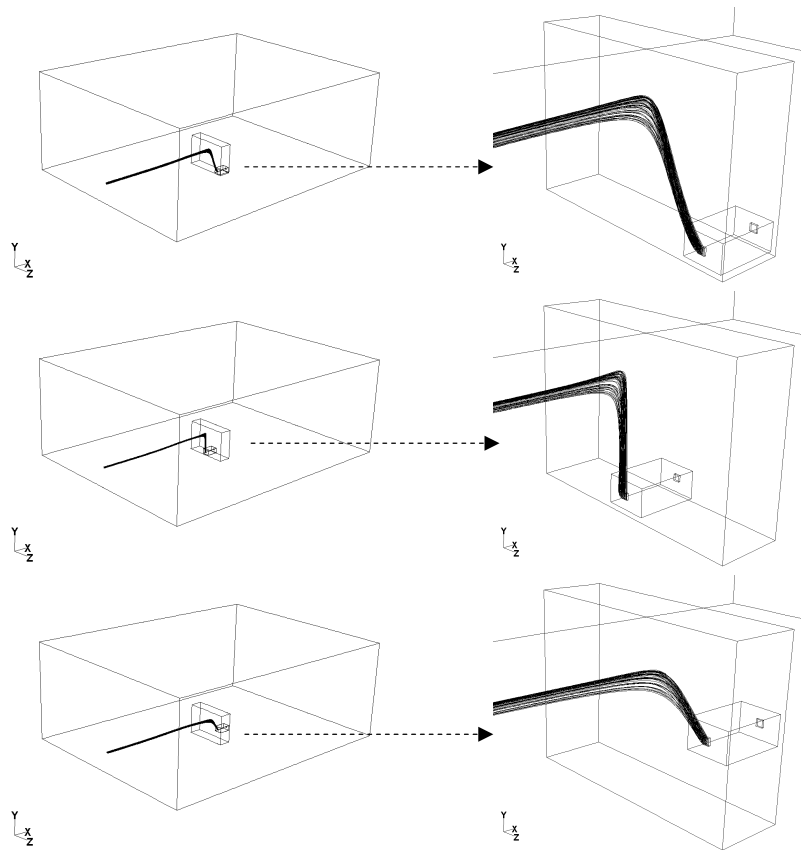
---

Experimental and numerical analysis of Building scale model

---

velocity distribution in the openings. The measured pressure distribution can however to some extent be used to clarify the flow around the building as well as the measured velocities can be used to analyse the airflow going into the rooms.

Figure 6.7 shows the streamlines upwind of the building that goes through the opening for 6 different opening locations, two at the bottom, two in middle and two placed at the top of the building.



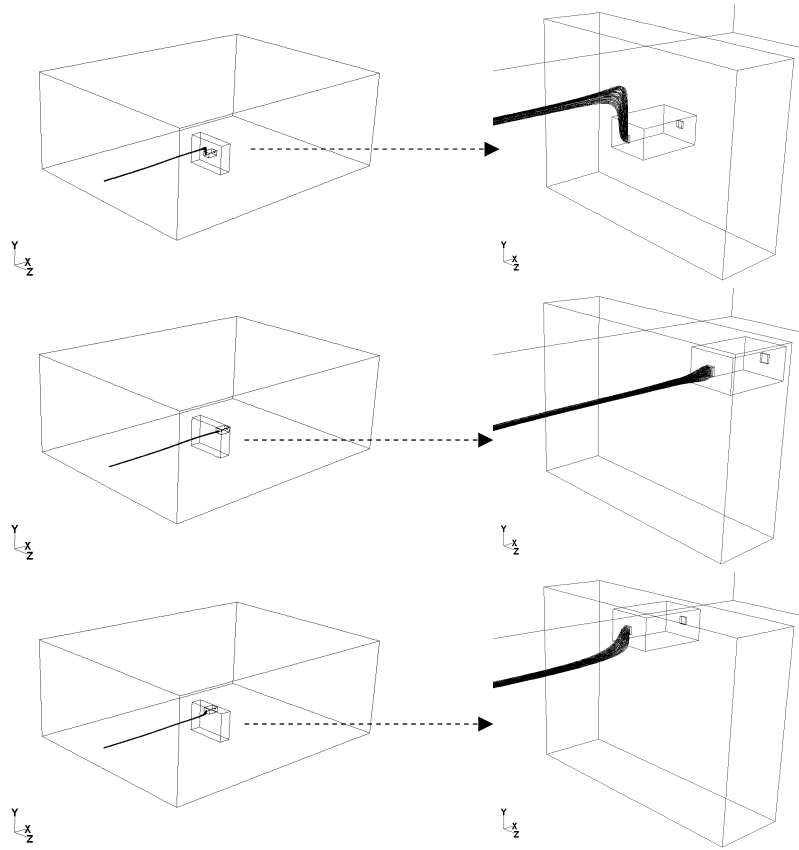


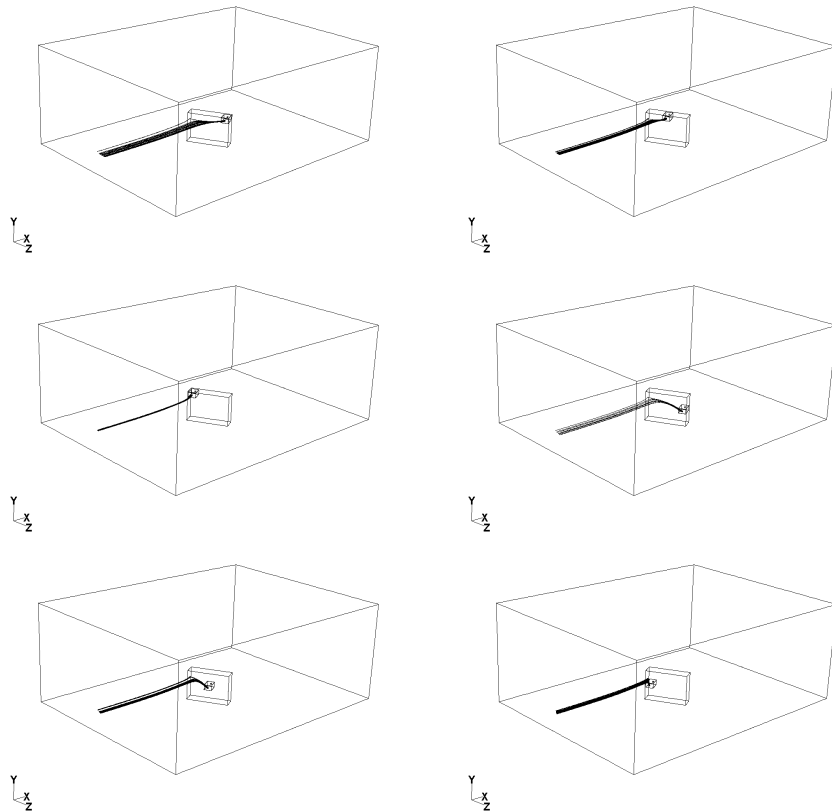
**Figure 6.7 Airflow pattern for streamlines going into the opening. Depicted for 6 different locations at a wind direction perpendicular to the building.**

The streamlines going through the openings originates approximately from the same area in the undisturbed boundary layer. The flow seems to be diverted from the stagnation point (or area) placed at upper-middle part of the building towards the respective openings. This diversion of the flow has a great impact on the direction of the flow going into the opening.

In the same way it can be shown that when the building is placed at an angle towards the flow the streamlines originate from approximately the same area, see Figure 6.8 and Figure 6.9. When the building is placed at an

angle towards the flow the streamlines are diverted towards the opening from an area placed in the upwind part of the building, i.e. the location of highest pressure.

When a wind incident angle of 60 degrees is applied the area of highest pressure is located at the end of the building and not on the façade, this causes the mentioned diversion of the airflow to happen somewhere near the upwind edge of the building.



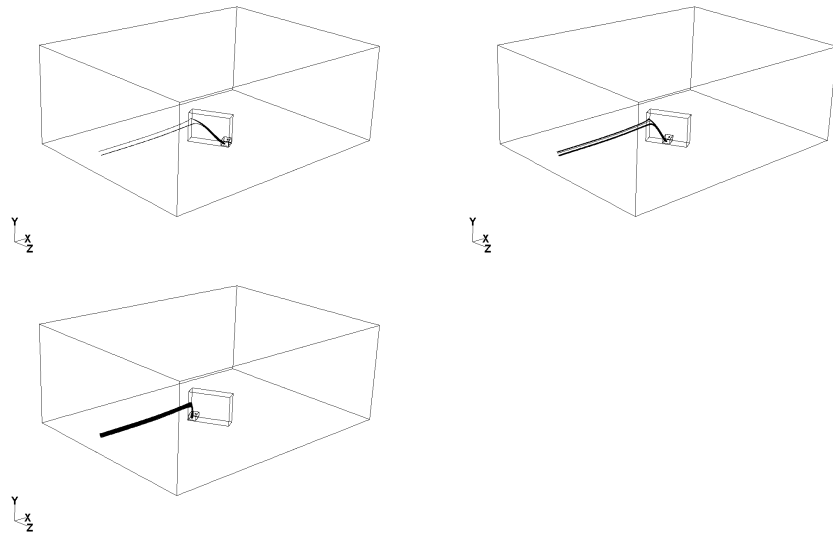


**Figure 6.8 Upwind streamlines going into the opening at a wind direction of 30 degrees. Depicted for 9 different location of the opening.**

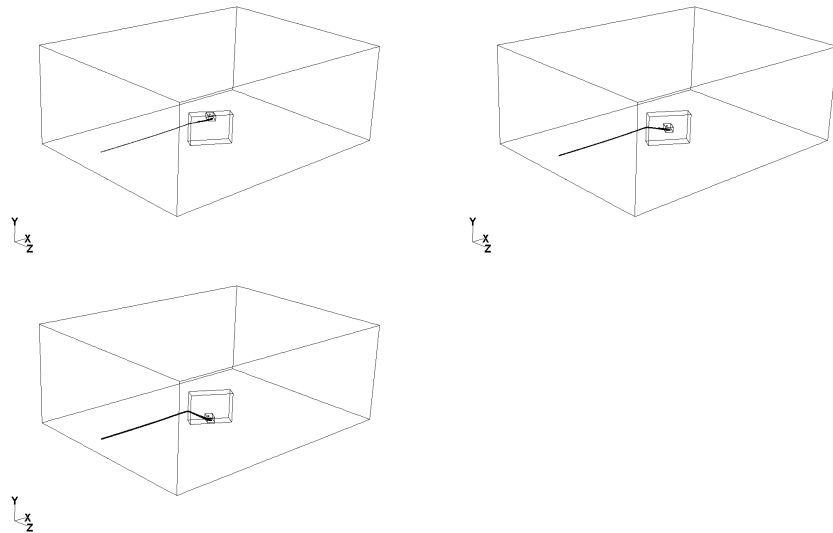


**Figure 6.9 Upwind streamlines going into the opening at a wind direction of 60 degrees. Depicted for three opening location in the middle of the building.**

As mentioned the direction of the air flowing into the room is dependent on the location of the room in the building. Figure 6.10 shows the directional vector of the flow going into the rooms for a wind direction of 0 degrees. Despite the wind direction being perpendicular to the opening the direction of the flow into the room is completely dependent on the location in the building. All velocity vectors are pointing away from the area of stagnation.

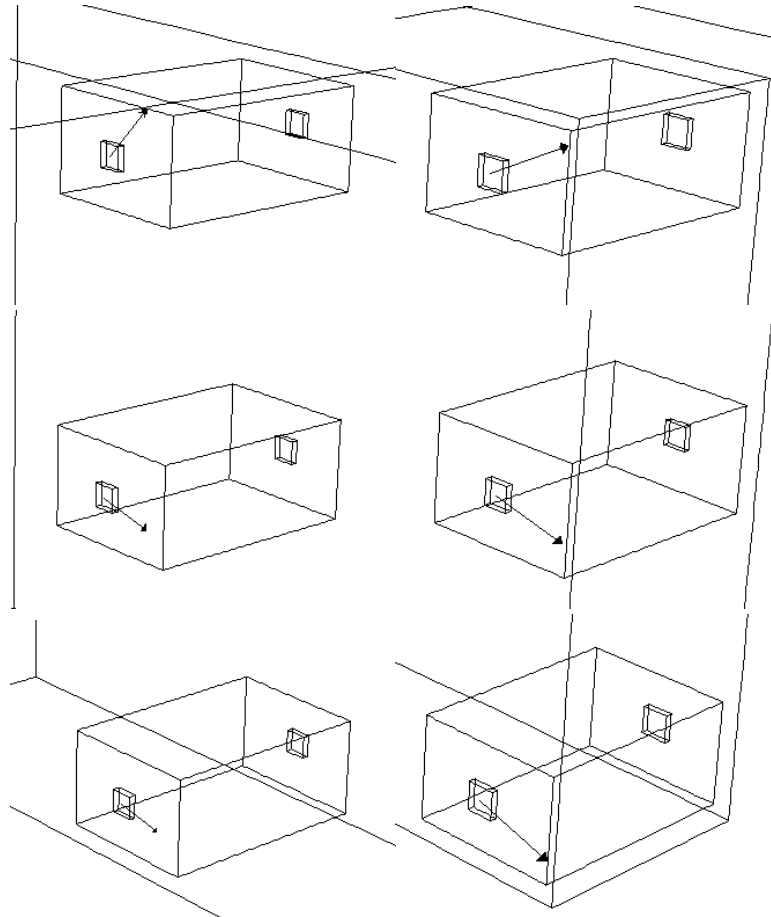


**Figure 6.10** Direction of flow entering the room. Depicted for 6 different opening location and at a wind direction of 0 degrees.

Similar results are found for the other wind directions.

#### **Velocity distribution in openings**

The influence of the location of the opening in combination with the wind direction on the airflow can be discussed graphically by considering the velocity distribution in the openings at different wind incident angles. Figure 6.11 shows the velocity distribution for different opening locations



as well as different wind directions. The comparison is shown for an opening size of 316 mm<sup>2</sup> since it is the most detailed (most measured points) and for wind directions of 0, 30 and 60 degrees. It should be emphasised that the small x-values represent openings placed downstream when the building is placed at an angle towards the flow.

There is a large variation in the velocity distribution in the openings when comparing it in regards to the location and wind direction. For a wind direction of 0 degrees the velocities are highest at the top and in the horizontal middle of the building. For the openings placed at the sides of the building the velocity distribution is higher in the part of the opening placed close to the edge, this seems to be an effect of the airflow surrounding the building. When the building is placed at an angle compared to the flow the velocities are highest in the openings placed in the upwind part of the building, here the velocities are also almost uniformly distributed across the opening. For the openings placed in the middle and further downstream the velocities are highest in the part of the opening placed upstream again due to the surrounding airflow.

Experimental and numerical analysis of Building scale model

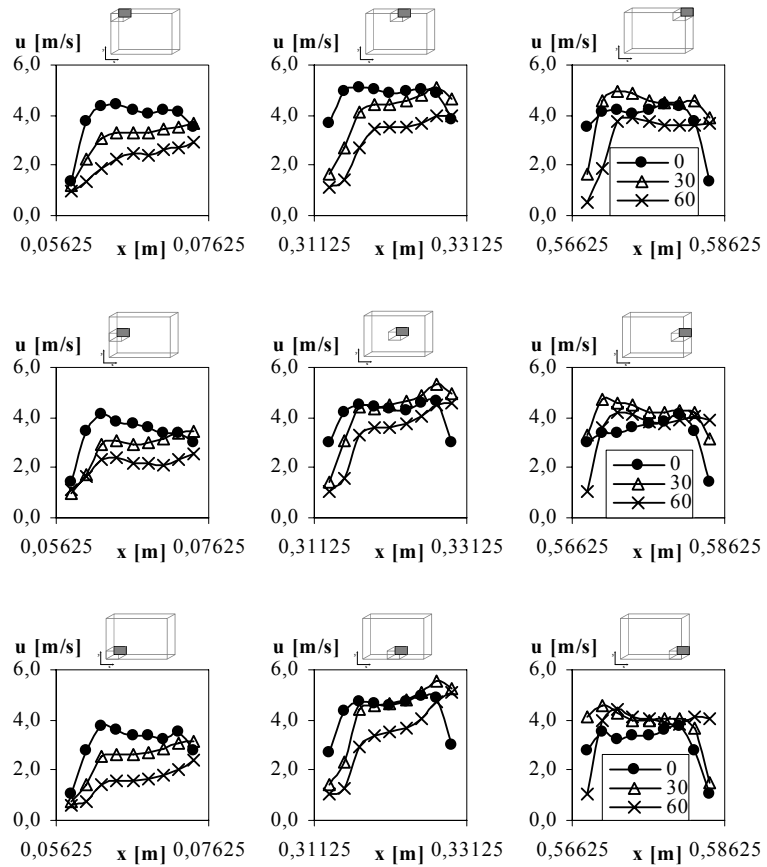


**Figure 6.11** Velocity distribution in leeward side opening for different wind directions and chosen locations. Depiction shows values found for a circular opening of 314 mm<sup>2</sup>.

Figure 6.12 shows the velocity distribution in the openings for a square opening of 306 mm<sup>2</sup> for different locations in the building at a wind direction perpendicular to the building. The depiction shows both the velocity measurements in the leeward side opening as well as the predicted velocities in the windward and leeward side opening.

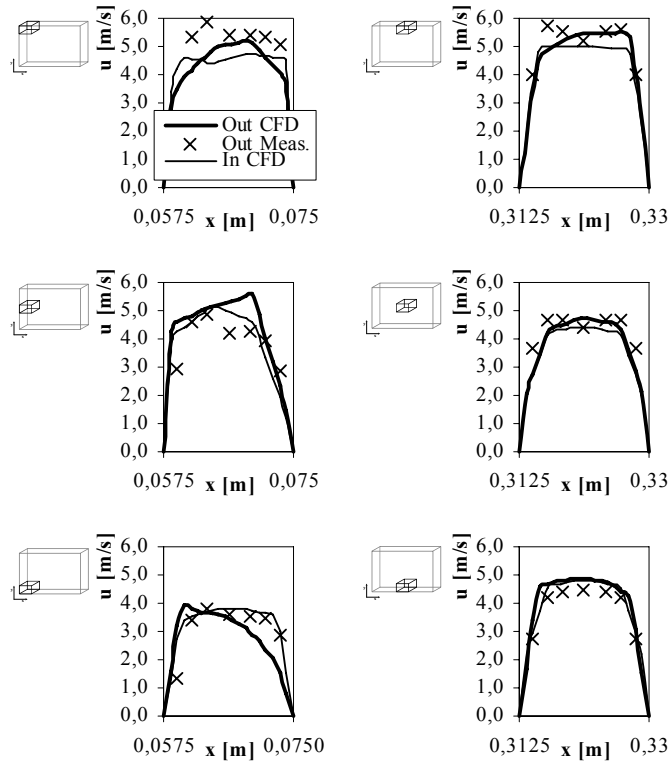
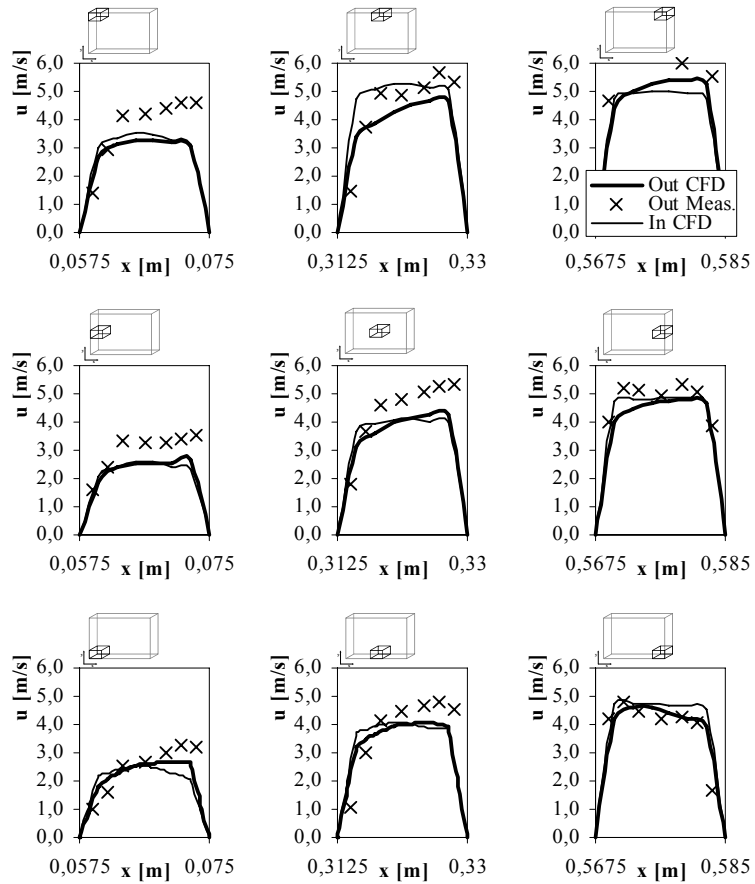


**Figure 6.12 Velocity distribution in the openings for different locations in the building and a wind direction of 0 degrees. Both CFD and measurements are included in the depiction.**

In the horizontal middle of the building (depictions to the right) the velocity distribution is uniform and there is an good correspondence between the measurements and the predictions. At the side of the building the correspondence is acceptable but deviancies are present. The measurements show only to some extent the same tendency to be diverted towards the edge of the building as was the case in Figure 6.11, this is however the case for the prediction placed at the bottom. In connection to the predictions it should be mentioned that it is the resultant velocity that has been depicted

and not the velocity in a given direction. Also here the velocities are highest at the top of the building.

Figure 6.13 shows the corresponding depiction as Figure 6.12 but here with a wind direction of 30 degrees. The velocities from the measurements seems to obtain a higher level than is the case for the predictions. The pattern of the velocity distribution is however similar despite the lower order of magnitude of the predictions. In the same way as was the case in Figure 6.11 the flow (from the leeward side openings) is directed upstream for the openings located in the downstream part of the building.



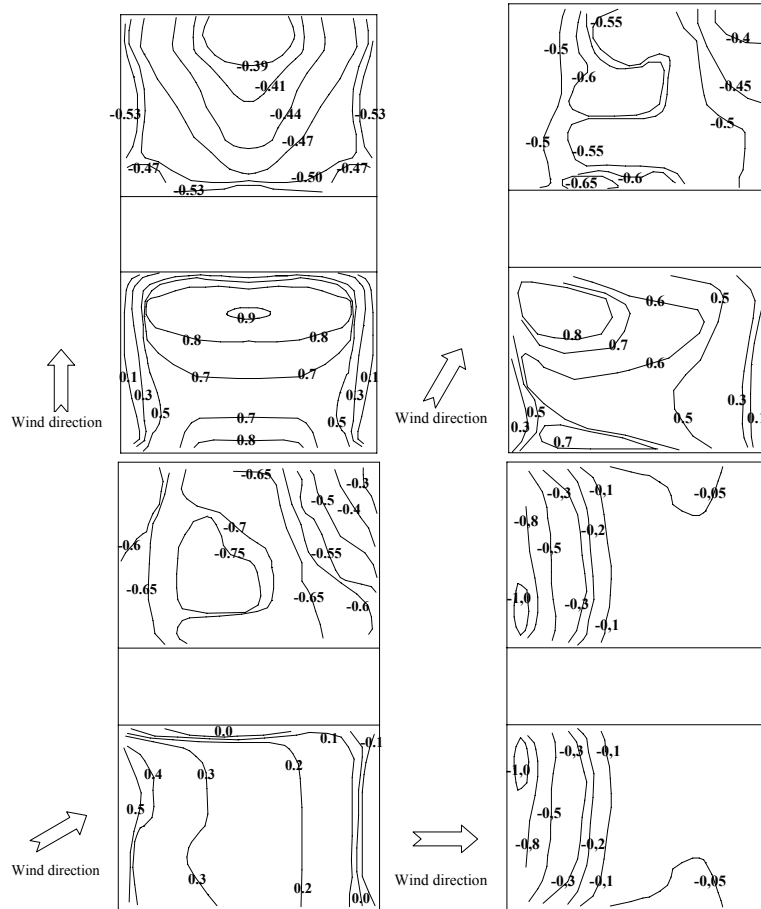
**Figure 6.13 Velocity distribution in the openings for different locations in the building and a wind direction of 30 degrees. Both CFD and measurements are included in the depiction.**

Figure 6.13 shows a velocity level that is higher at the top of the building as well as in the openings placed in the upstream part. A similar pattern is found for a wind direction of 60 degrees (see values in spreadsheet on the attached CD-rom).

#### *6.4.3. PRESSURE DISTRIBUTION*

The pressure distribution will be analysed by comparing the pressure on the sealed building with the pressure when an opening is placed in this building.

The measured pressure distribution on the sealed building is depicted in Figure 6.14. The figure shows a “fold out” of the pressure distribution on the two facades of the building. The Shown pressure contours are interpolated from 100 measuring points on each façade (Only 50 points when the wind direction is 0 due to symmetry).



**Figure 6.14 Measured pressure distribution on sealed building for wind directions of 0, 30, 60 and 90 degrees.**

The pressure distribution is clearly influenced by the created wind profile. When a wind direction of 0 degrees is applied the maximum pressure is located at the top (vertically) of the building and in the middle (horizontally). In this location a separation of the flow occurs, a part of the flow is diverted towards the ground creating a small rise in the pressure in this area. The leeward side show only a small variation in the magnitude of the pressure. When the wind direction is altered from 0 the pressure is

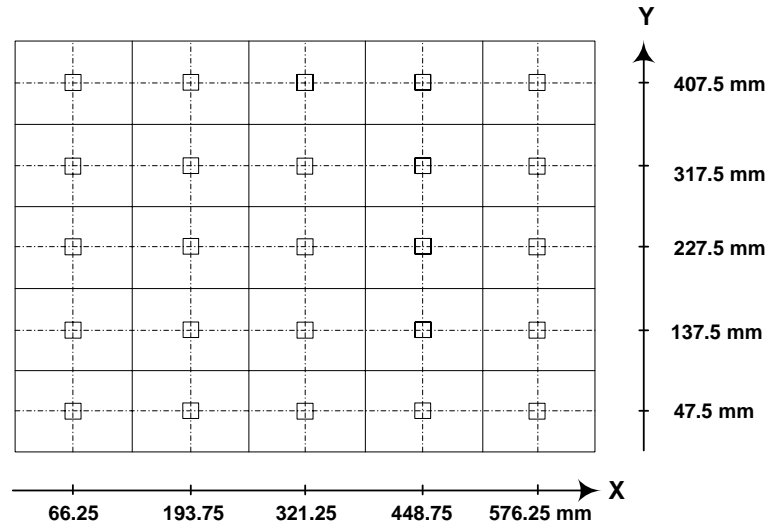
diverted towards the upwind side of the façade, and finally when the wind directions is 90 degrees the pressure is negative on both sides. When the wind direction is 60 degrees there is a small part of the windward side that obtains a negative pressure due to flow separation occurring on the end of the building diverting the flow away from the building at the downstream end of the façade.

#### **Comparison of pressure distribution with and without opening**

Due to the amount of measurement data only a representative part of this will be presented.

Figure 6.15 shows the partition of rooms in the building and the location of the openings and their corresponding local x- and y- coordinates. In connection to this it should be noted that when the building is placed at an angle compared to the flow the low x-values represent the part of the building that is placed downstream while the higher x-values represent the part placed upstream.





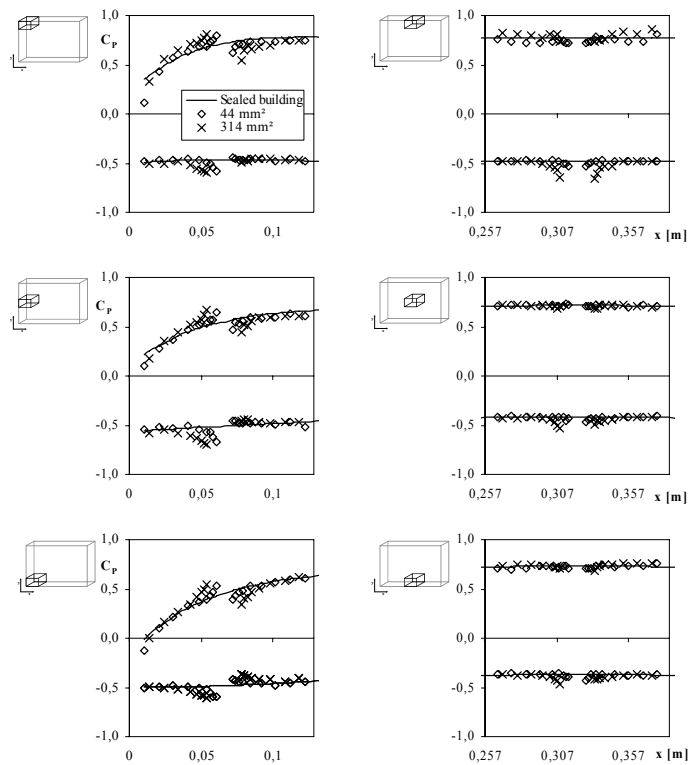
**Figure 6.15 Location of openings and definition of local x- and y-axis on the building.**

Figure 6.16 shows the pressure distribution of the sealed building compared to the pressure distribution when an opening (Opening sizes of 44 and 314 mm<sup>2</sup>) is placed in the building. The pressure distribution is shown for two rooms located at the bottom of the building, two in the middle as well as two rooms located at the top of the building.

Figure 6.16 shows that the windward side pressure for the openings placed off centre in the building is higher (than for the sealed building) on the one side of the opening, and lower on the other. This is due to the flow being directed from the centre of the building and towards the sides which causes the velocity distribution in the opening to be non-uniform with high velocities at the side of the opening placed nearest to the side of the building. The velocity distribution influences the pressure distribution in the vicinity of the opening. The leeward side pressure (for the openings placed horizontally off centre) is also changed due to the non symmetrical velocity distribution, however here the pressure becomes lower at the side placed

closest to the edge of the building which is the opposite of what is happening on the windward side. This is caused by the internal airflow in the room which changes direction from the upwind opening (which is directed away from the centre of the building) to the leeward one (which is directed towards the centre of the building).

The predictions show the same general tendency as the measurements and have therefore been left out.



**Figure 6.16** Measured horizontal surface pressure distribution as a function of the distance  $x$  both with and without an opening placed in the room. The wind direction was 0 degrees. The vertical location of the openings is shown above the depictions.

The pressure distribution close to the openings placed in the horizontal centre only show smaller deviances compared to the sealed building and mainly on the leeward side of the building.

In the same way the vertical pressure distribution is depicted in Figure 6.17.

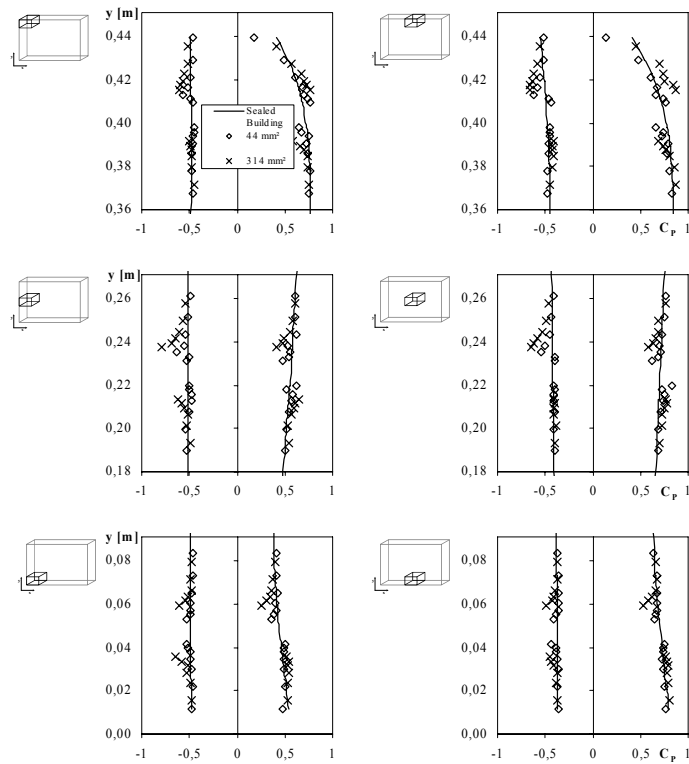


**Figure 6.17 Measured vertical pressure distribution both with and without an opening (opening areas of 44 and 314 mm<sup>2</sup>) placed in the room. The wind direction was 0 degrees. The horizontal location is shown above the depictions.**

Also the pressure measurements in the vertical direction show alteration compared to the sealed building. At the top of the building the distribution is similar to the one found for the horizontal measurements which is due to the airflow being directed upwards from the stagnation area.

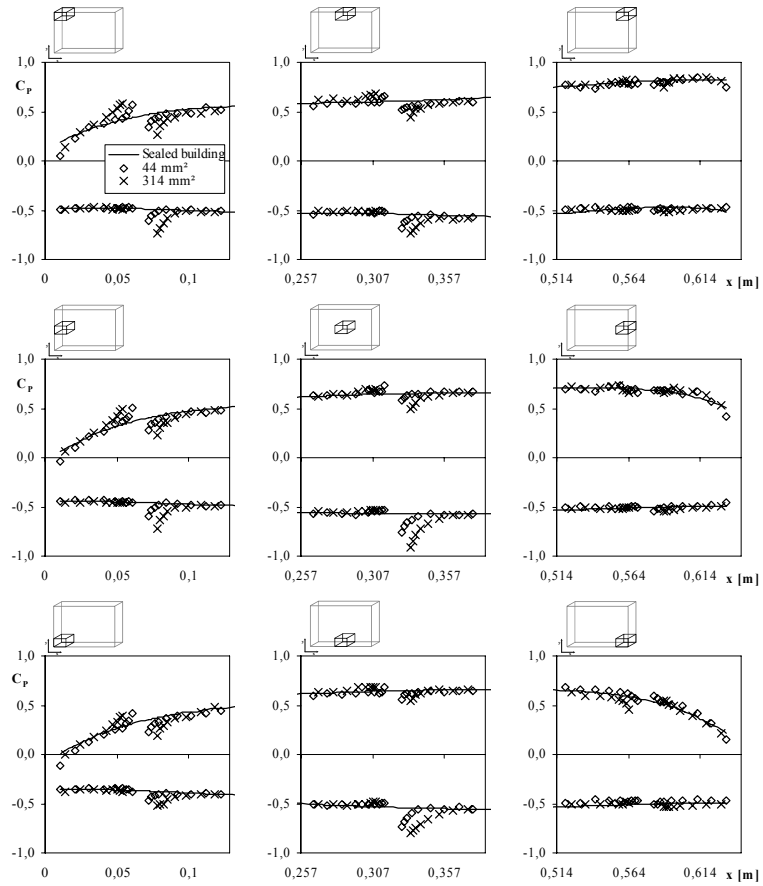
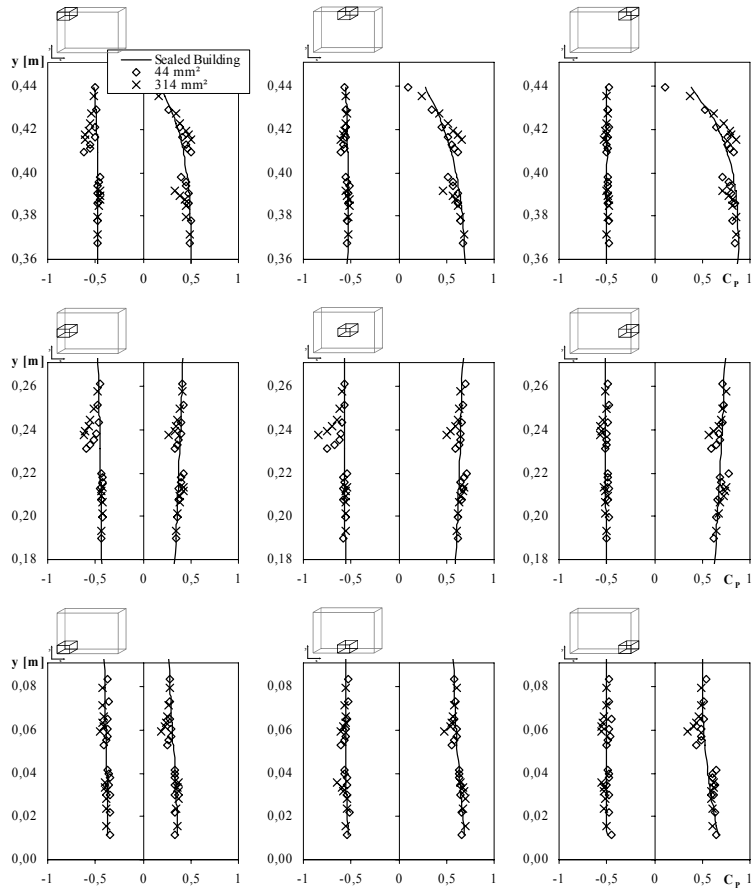


**Figure 6.18 Measured horizontal surface pressure distribution as a function of the distance  $x$  both with and without an opening placed in the room. The wind direction was 30 degrees. The vertical location of the openings is shown above the depictions.**

When a wind incident angle of 30 degrees is applied the pressure distribution on the windward side for the openings located downstream (Figure 6.18) experience the same alteration as was the case at an angle of 0 degrees. On the leeward side the pressure is only changed to the side placed

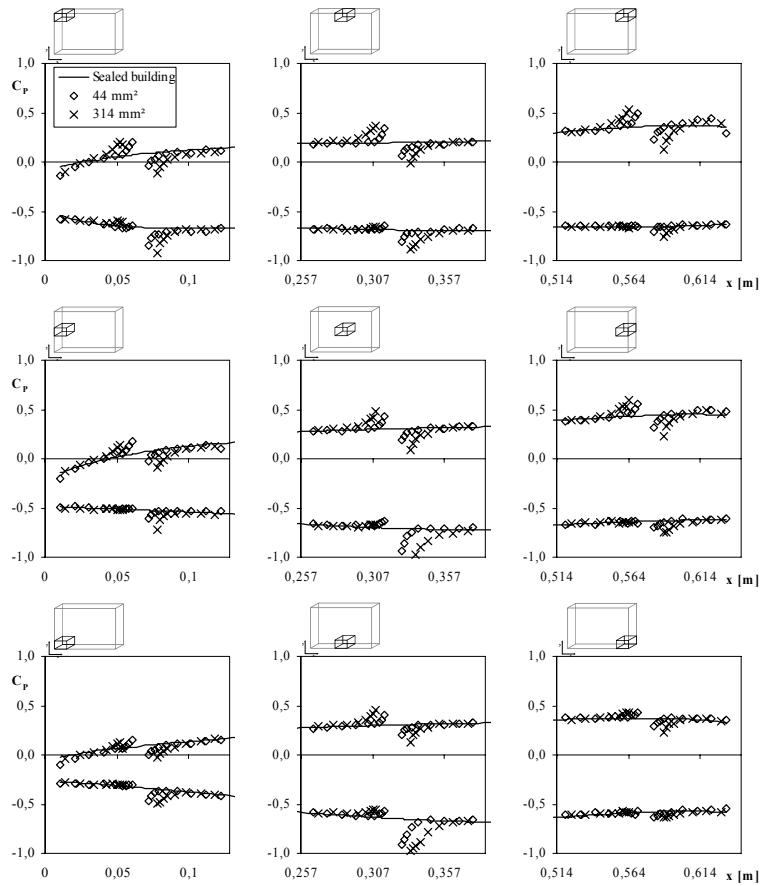
towards the centre of the building where the pressure is lower than for the sealed building. The corresponding airflow from the opening is also directed towards the centre of the building due to the flow path in the room. The pressure distribution in the vicinity of the openings placed in the horizontal centre of the building shows the pattern as the ones placed downstream. The pressure distribution close to the openings placed upstream show only a small or no deviation from the pressures for the sealed building.

Figure 6.19 shows the vertical pressure distribution measured close to the openings with a wind direction of 30 degrees. Similar deviations in pressure distribution caused by the changes in the airflow can be seen here.



**Figure 6.19 Measured vertical pressure distribution both with and without an opening (opening areas of 44 and 314 mm<sup>2</sup>) placed in the room. The wind direction was 30 degrees. The horizontal location is shown above the depictions.**

Figure 6.20 and Figure 6.21 show the horizontal and the vertical pressure distributions close to the openings using a wind incident angle of 60 degrees. Here all the measured horizontal surface pressures in the vicinity of the openings are affected by a non-symmetric velocity distribution in the openings.



**Figure 6.20 Measured horizontal surface pressure distribution as a function of the distance  $x$  both with and without an opening placed in the room. The wind direction was 60 degrees. The vertical location of the openings is shown above the depictions.**

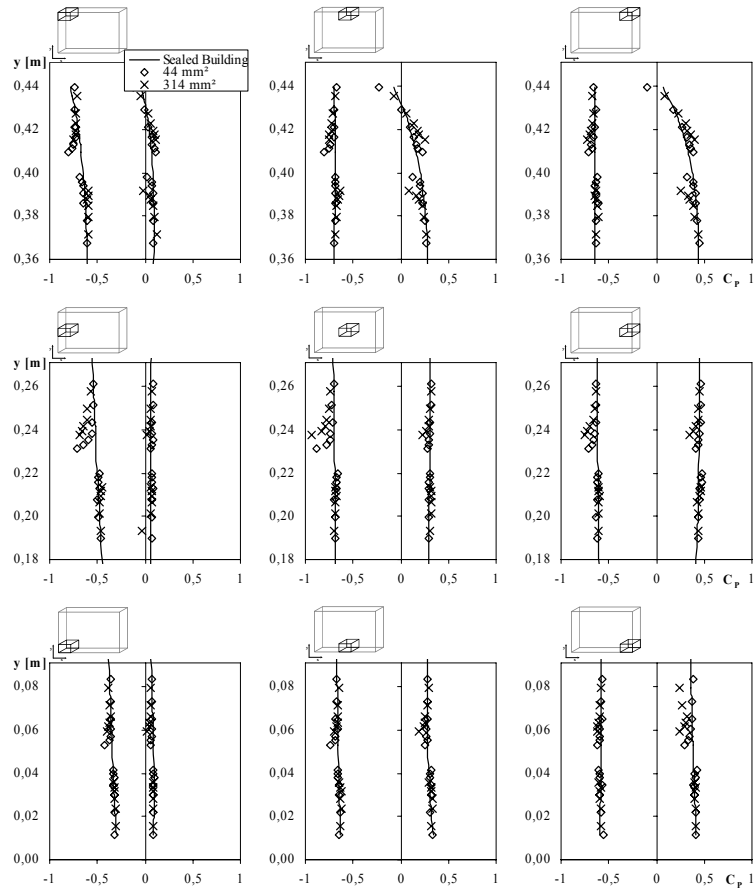


**Figure 6.21 Measured vertical pressure distribution both with and without an opening placed in the room. The wind direction was 60 degrees. The horizontal location is shown above the depictions.**

Figure 6.22 and Figure 6.23 shows the horizontal and respectively the vertical surface pressure distributions in the vicinity of the openings with a wind direction of 90 degrees. Due to symmetry the mean velocities in the openings are 0 and the pressure distributions are not influenced by the openings.



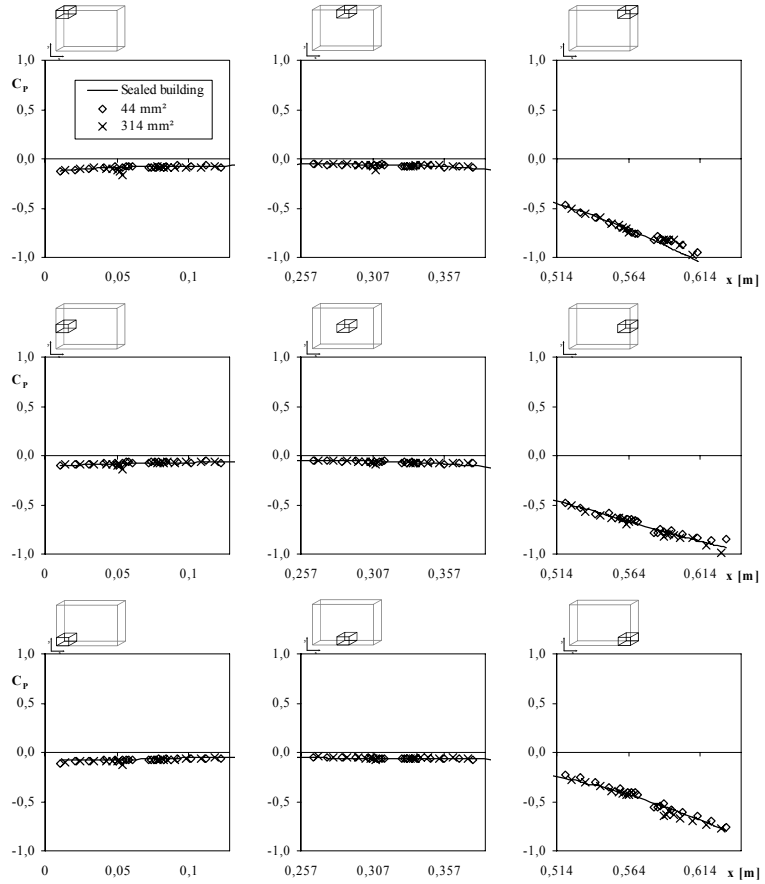


**Figure 6.22 Measured horizontal surface pressure distribution as a function of the distance  $x$  both with and without an opening placed in the room. The wind direction was 90 degrees. The vertical location of the openings is shown above the depictions.**

## Experimental and numerical analysis of Building scale model

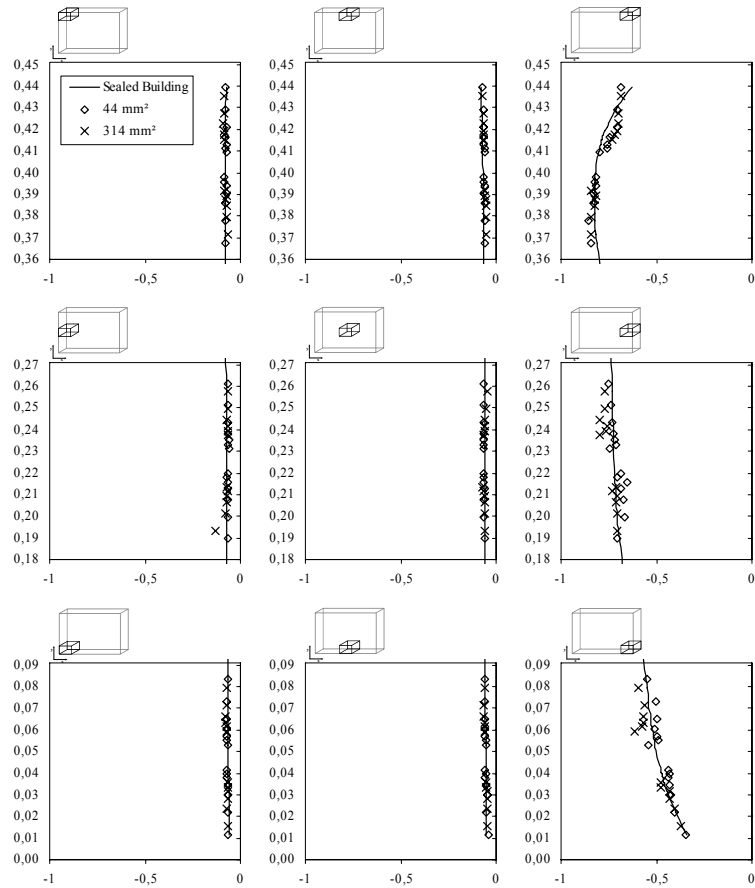


**Figure 6.23 Measured vertical pressure distribution both with and without an opening placed in the room. The wind direction was 90 degrees. The horizontal location is shown above the depictions.**

All pressure measurements can be found in the spreadsheet on the attached CD-rom.

### **Pressure Difference across building**

The pressure difference across the building is the commonly used measure of the driving force of the airflow through a building. The pressure was measured on both the windward and the leeward side of the building as well as inside the room where the openings were placed. Figure 6.24, Figure 6.25 and Figure 6.26 shows the pressure difference across the whole building for the wind directions of 0, 30 and 60 degrees respectively. A depiction using a wind direction of 90 degrees has not been included since it will just result in a pressure difference of 0.

When the wind direction is perpendicular to the building (0 degrees) the pressure difference is to some extent constant varying only from  $\Delta C_p = 0.90$  to 1.25. The pressure difference is smaller at the sides as well as in the lower part of the building. The pressure difference is not smallest at the bottom of the building due to the recirculation zone in front of the building which causes an airflow directed downwards and a higher pressure at the bottom than somewhere just above the bottom (see also Figure 6.14).

When the wind incident angle is 30 and 60 the part of the building placed downstream obtains a smaller pressure difference than the part placed upstream. The variation in pressure difference is also higher than for the perpendicular case. At 30 degrees the maximum pressure difference is obtained in the area of  $x = 448.5$  mm, which indicates the location of where the flow divides. This means that the flow to some extent is going the opposite direction of the general flow direction.

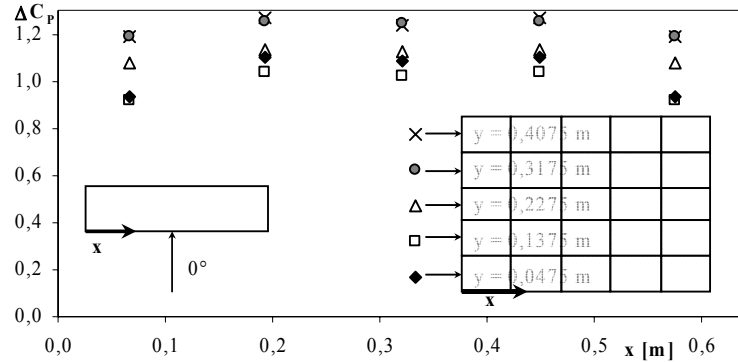


Figure 6.24 Total pressure difference across the building in the locations where the openings are placed with a wind direction of 0 degrees. Depicted as a function of the location on the x-axis for different values of y.

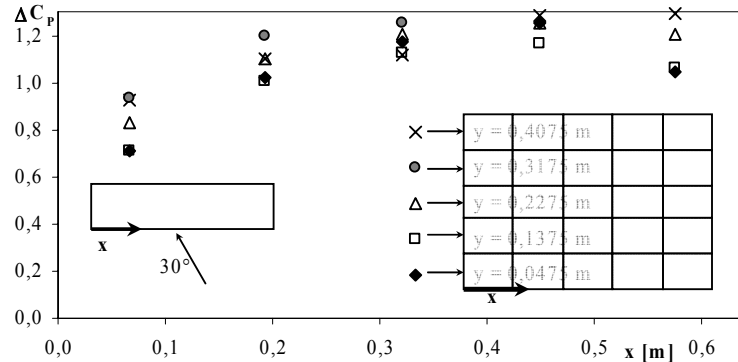
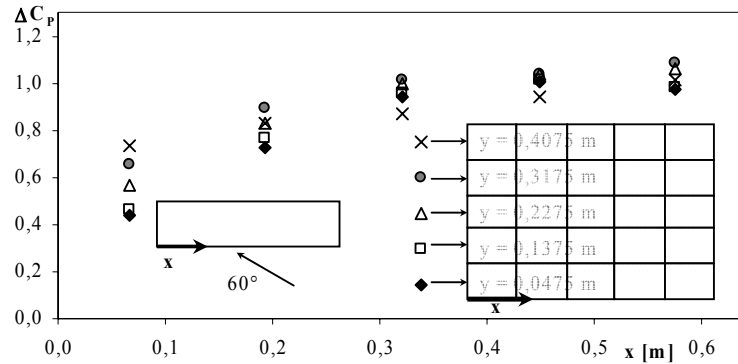


Figure 6.25 Total pressure difference across the building in the locations where the openings are placed with a wind direction of 30 degrees. Depicted as a function of the location on the x-axis for different values of y.



**Figure 6.26 Total pressure difference across the building in the locations where the openings are placed with a wind direction of 60 degrees. Depicted as a function of the location on the x-axis for different values of y.**

The effect of the wind direction on the pressure difference across the building in the location of the openings is analysed in the following Figure 6.27. Figure 6.27 shows the pressure difference across the building as a function of the wind direction for different locations on the building. From this it can be concluded that the pressure difference for openings placed off centre is highly influenced by the wind direction (see Figure 6.27,  $x = 0.06625$  m).

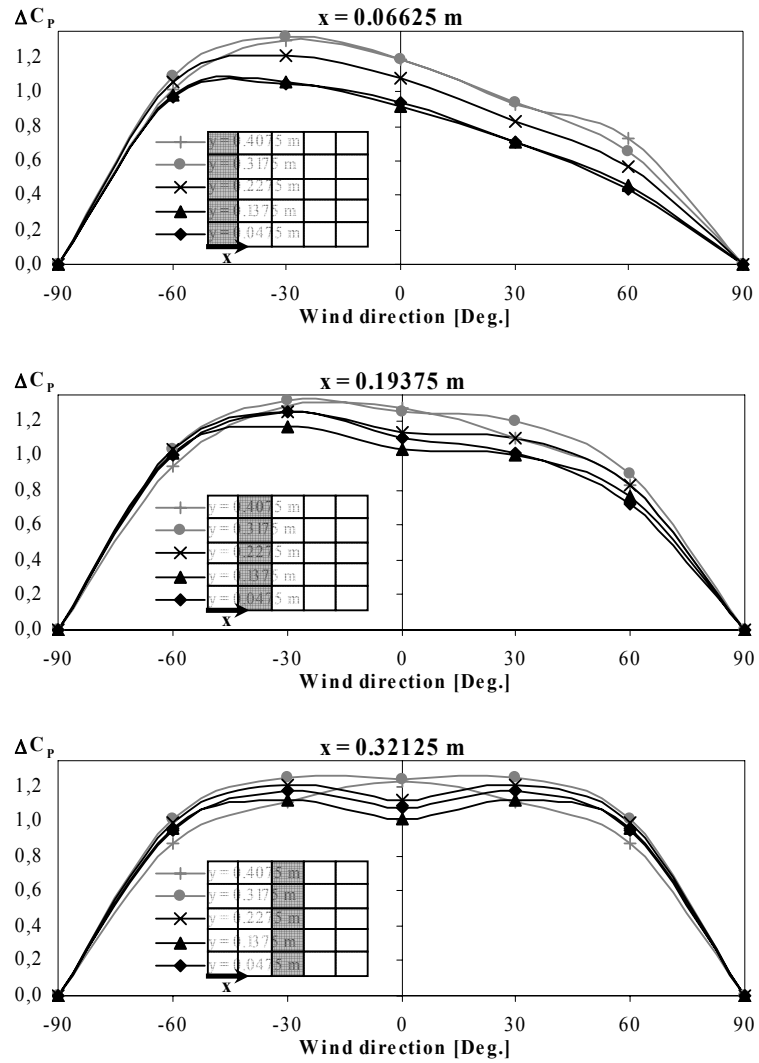


Figure 6.27 Pressure difference across the building as a function of the wind direction. Depicted for the location of the openings for three different locations on the x-axis and for different values of y.

In order to obtain knowledge of the pressure difference across the individual opening the pressure inside the rooms were measured, the corresponding pressure differences across the inlet and outlet openings for different wind directions are depicted in Figure 6.28, Figure 6.29 and Figure 6.30 for an opening size of  $A = 314 \text{ mm}^2$ . The pressure differences across the individual openings are not found to be of the same magnitude which indicates that there is a preservation of kinetic energy from the upwind opening which in turn decreases the pressure difference across the downstream opening. This seems to be the case for all three wind directions independently of the location of the opening. This means that there is flow contact between the openings.

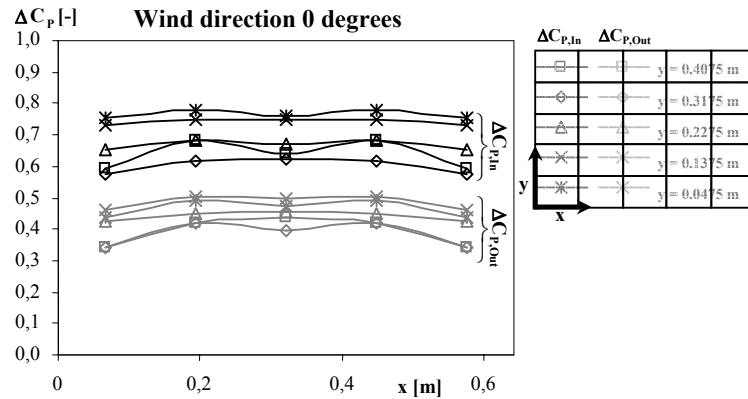


Figure 6.28 Measured surface pressure difference across the up- and downstream openings with a wind incident angle of 0 degrees. Depicted as a function of the width of the building in different heights.

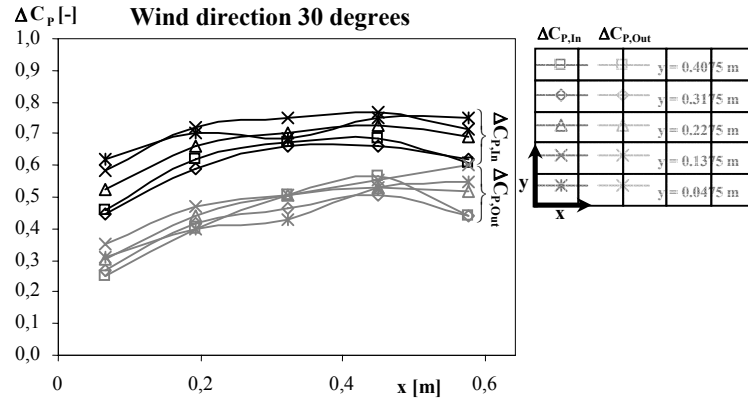


Figure 6.29 Measured surface pressure difference across the up- and downstream openings with a wind incident angle of 30 degrees. Depicted as a function of the width of the building in different heights.

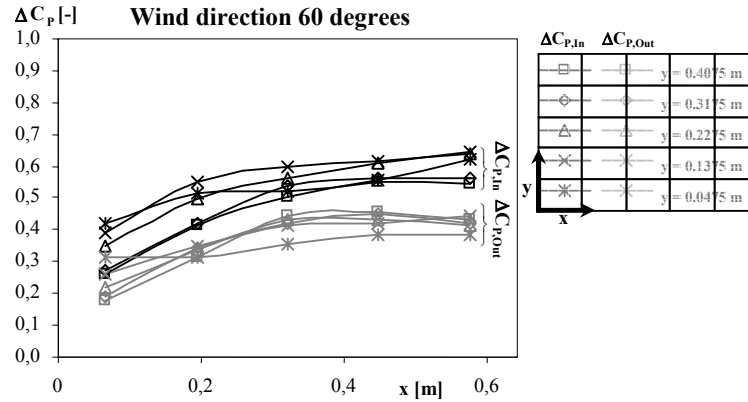
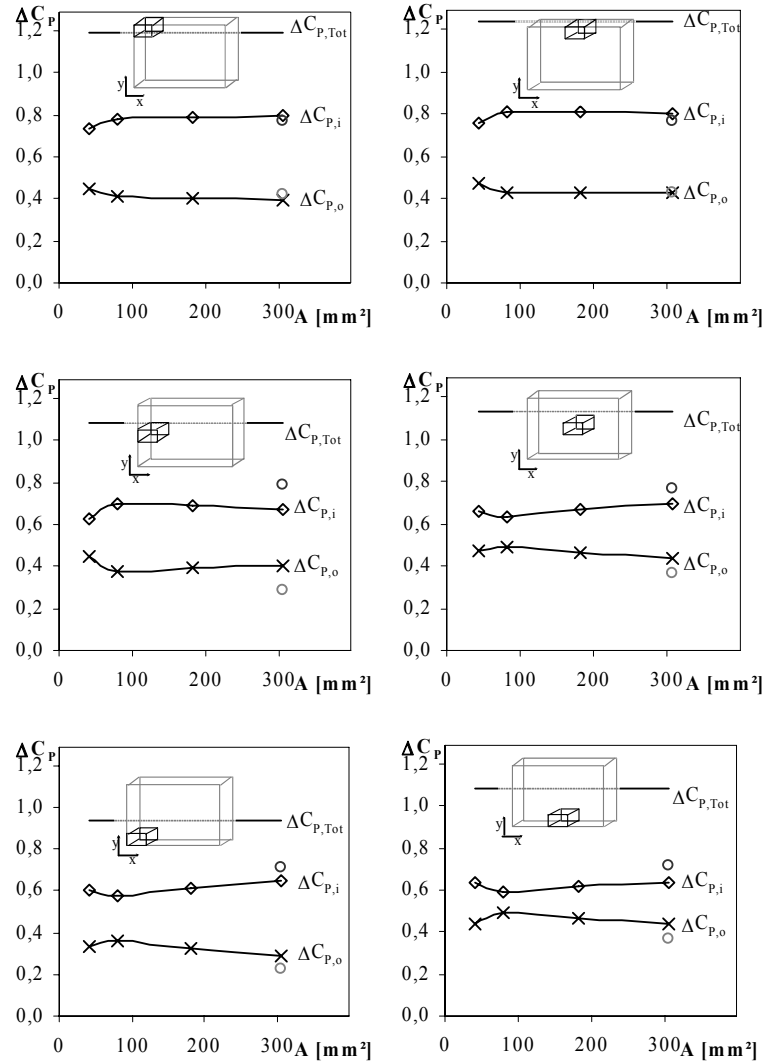


Figure 6.30 Measured surface pressure difference across the up- and downstream openings with a wind incident angle of 60 degrees. Depicted as a function of the width of the building in different heights.



The found flow contact between the openings is of cause dependent on the size of the opening and the distance between them as well as the inlet flow direction. If the pressure differences between the openings are identical the inlet jet is completely dissolved and there is no flow contact between the openings. The following Figure 6.31 shows the pressure difference across the individual opening as a function of the opening size at 6 different locations and at a wind direction of 0 degrees.

The found pressure difference between the upstream and downstream opening is surprisingly not equal even for the smallest opening size. There seems however to some extent to be an increasing tendency with the opening size. At the top of the building the pressure differences seem almost independent of the opening size. In three of the cases the smallest opening results in pressure differences that are higher than expected compared to the other openings, which could indicate some measurement error. The results of the angled flows seems to be similar to the ones depicted in Figure 6.31.



**Figure 6.31** Pressure difference for the whole building ( $\Delta C_{P,Tot}$ ) and across the up- and downstream openings ( $\Delta C_{P,i}$  and  $\Delta C_{P,o}$ ) as a function of the opening area. The pressure differences has been depicted for 6 opening locations at a wind direction of 0 degrees.

The pressure difference across the individual opening has not been found to be completely unambiguous, since the smallest opening should result in the pressure differences across the up- and downstream openings being closer together than the larger openings. This being due to the fact that the preservation of kinetic energy should be minimised by the decreasing opening size. At the top of the building the distribution of the two pressure differences is almost identical for the three larger openings this can be explained by considering the airflow around the sealed building which in this area is stagnant and the airflow will therefore be directed towards the normal of the opening.

#### *6.4.4. AIRFLOW RATE*

The airflow rate has been found by means of measurements of the velocity distribution in the openings placed on the leeward side of the building, as well as by means of the CFD predictions.

Figure 6.32 shows the relative airflow rate for the circular opening of 314 mm<sup>2</sup> as a function of the horizontal location. The depiction is shown for different vertical locations of the openings. The reference velocity used in the depictions is the measured velocity in the free boundary layer found in the height of the building.

The airflow rate is dependent on the location of the opening in the building. For a wind direction of 0 degrees the airflow is highest in the horizontal middle of the building as well as increasing with the height. When the building is placed at an angle towards the flow the airflow rate is higher for the openings placed upstream compared to those further downstream, but the vertical location seems to be of minor importance. It should be noted that the depictions are not completely representative for all measurements for all the openings since deviations are found, all measurements can be found on the CD-rom.

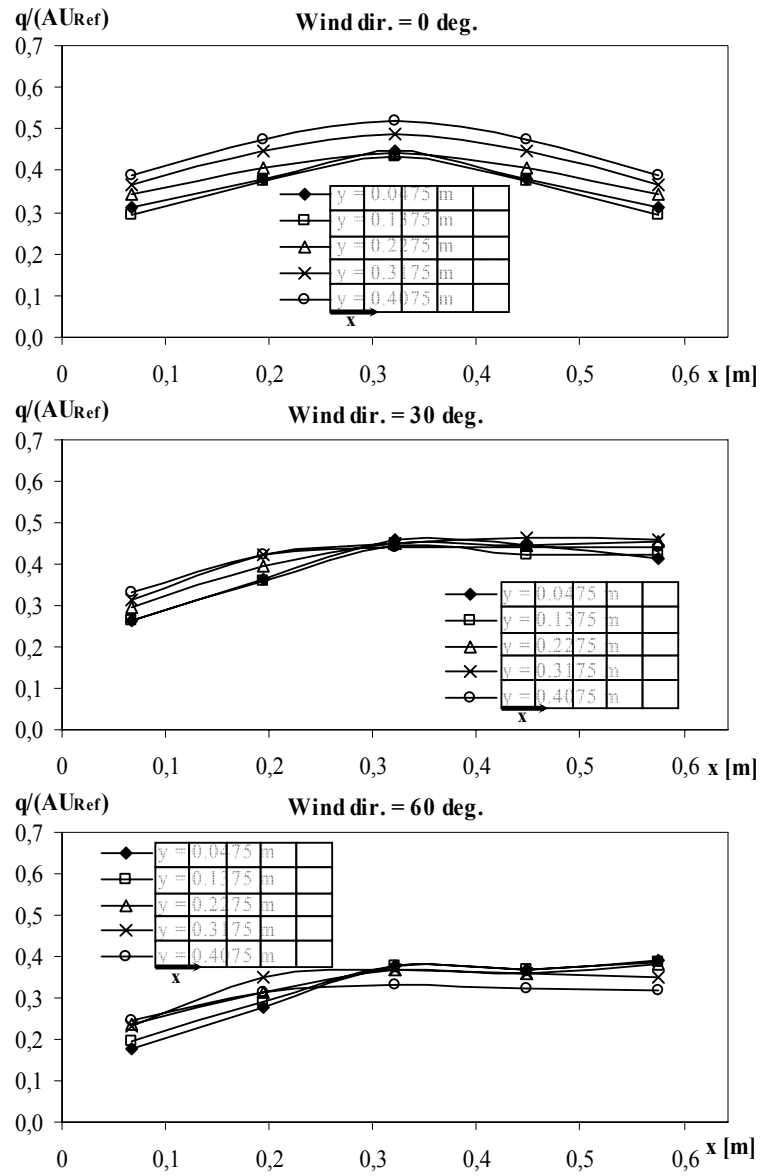


Figure 6.32 Relative airflow rate depicted as a function of the horizontal location with an opening area of 314 mm<sup>2</sup>.

Figure 6.33, Figure 6.34 and Figure 6.35 shows the relative airflow rates as a function of the horizontal location of the openings for wind directions of 0, 30 and 60 degrees respectively. The figures show depictions for 3 different vertical locations (openings placed at the top, middle and bottom). Both measurements as well as CFD (where available) has been included in the depictions.

There is a large variation in the magnitude of the relative airflow rates for different opening sizes, and this seems to some extent to be due to the calculation method especially since the values of the square openings obtain a generally higher level. The values found from the predictions are in the same vicinity as the measurements even though they seem to be a bit too small when an angled flow is applied. It is clear that no general conclusion can be drawn in regards to the size or shape of the opening, however a general tendency is found with regards to the location of the opening. The airflow rate increases with the vertical location of the opening and is higher closer to the regions where the pressure difference is highest (see Figure 6.24, Figure 6.25 and Figure 6.26).

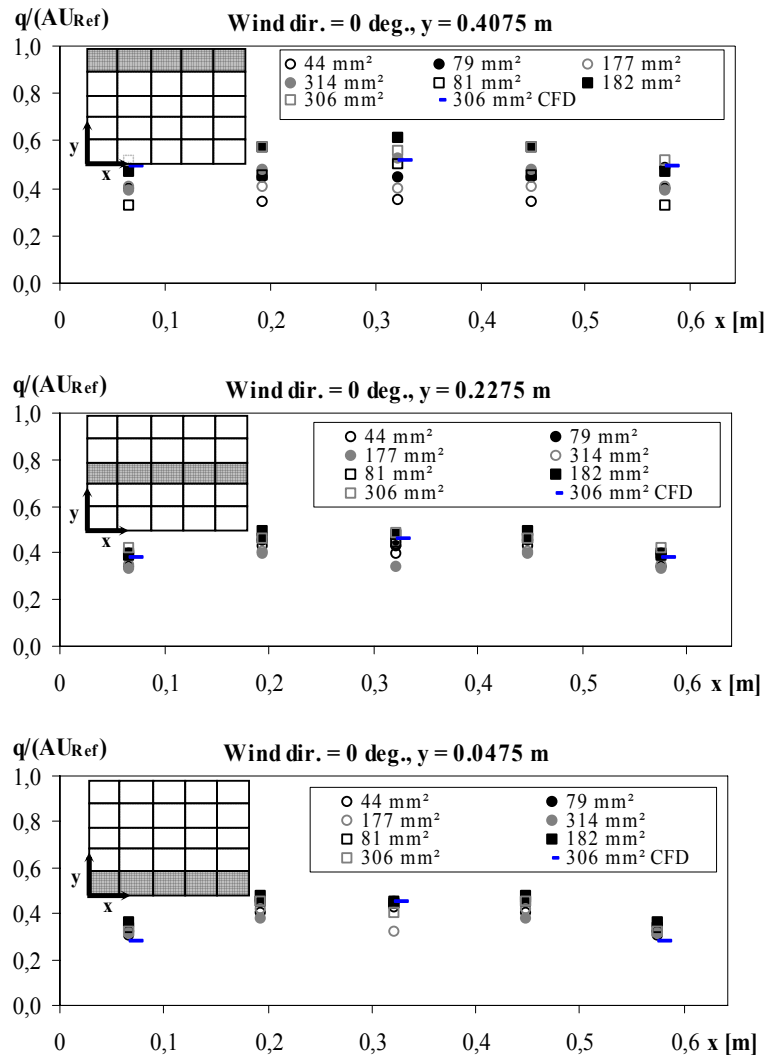


Figure 6.33 Relative airflow rate vs. horizontal location of the opening in the building found from measurements and predictions. Depicted for values found at the top, middle and bottom of the building. The wind direction was 0 degrees.

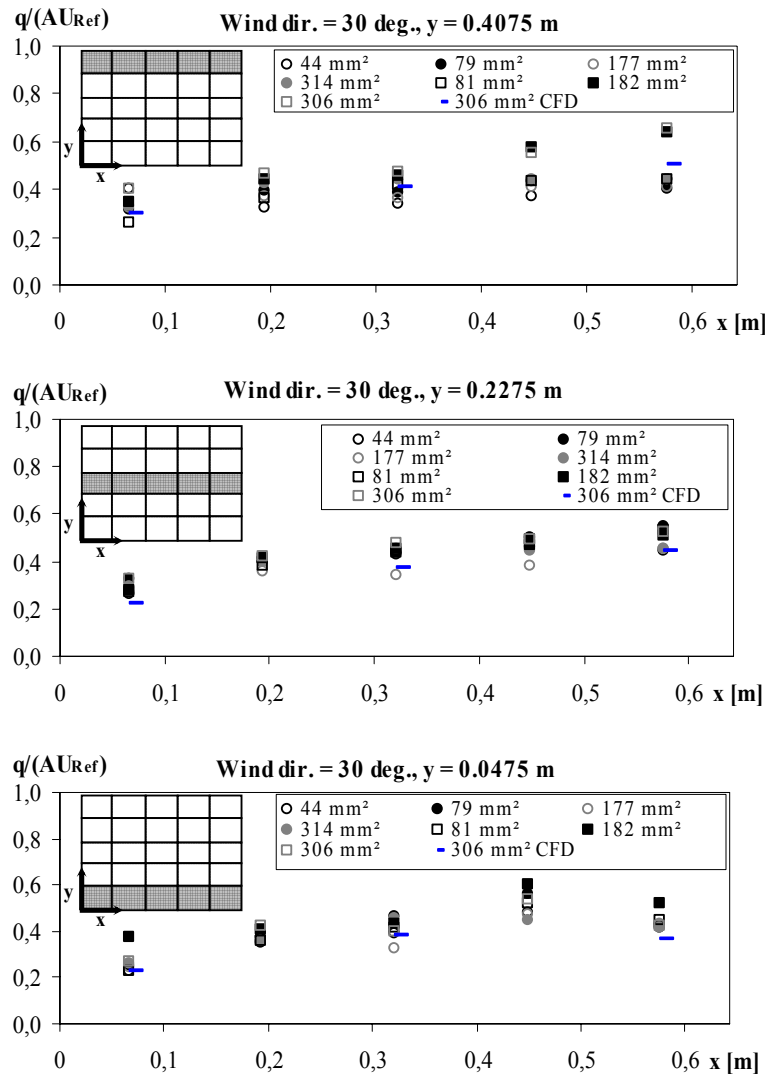


Figure 6.34 Relative airflow rate vs. horizontal location of the opening in the building found from measurements and predictions. Depicted for values found at the top, middle and bottom of the building. The wind direction was 30 degrees.

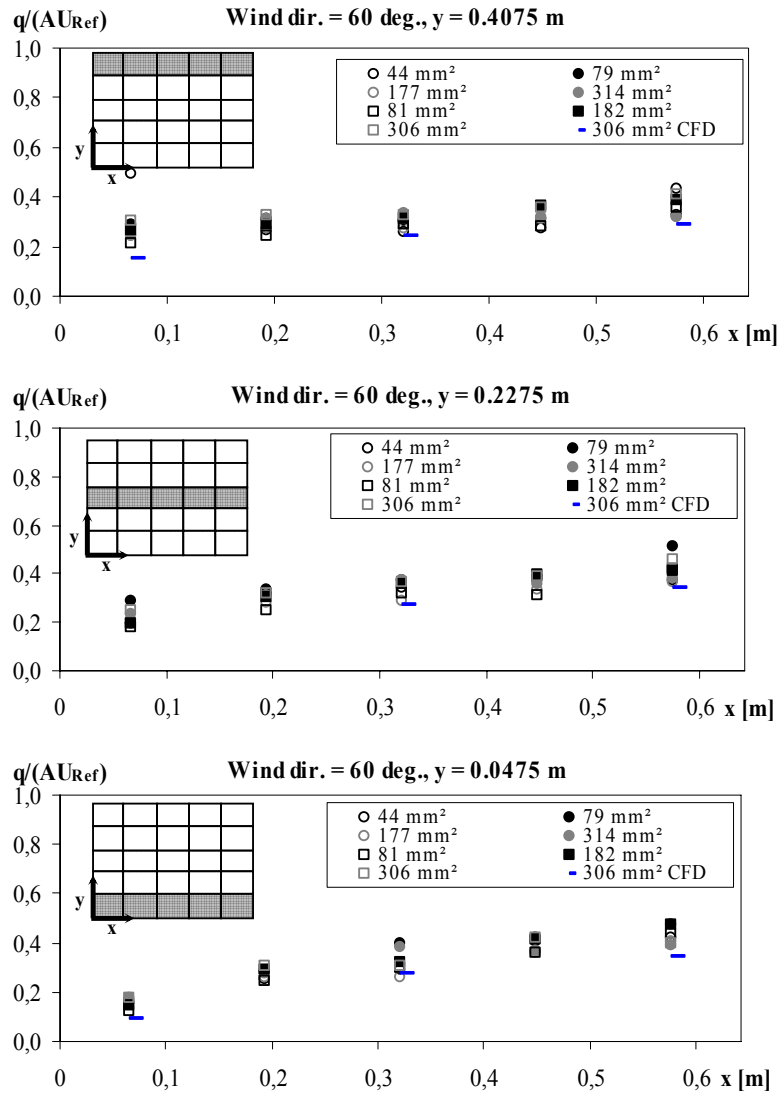


Figure 6.35 Relative airflow rate vs. horizontal location of the opening in the building found from measurements and predictions. Depicted for values found at the top, middle and bottom of the building. The wind direction was 60 degrees.



If the mean pressures measured on building surfaces are used in combination with a value of the discharge coefficients of 0.6, the airflow rates described in Table 6.2 are obtained. The relative airflow rates are calculated from:

$$\frac{q}{A \cdot U_{ref}} = C_D \sqrt{\frac{\Delta C_P}{2}} \quad (\text{Equation 6.2})$$

It should be noted that this expression is derived by applying the standard flow equation to both openings leading to 2 equations involving the internal pressure and by replacing the internal pressure from the one equation into the other equation 6.3 is obtained:

$$\frac{q}{A \cdot U_{ref}} = \frac{C_{D1} C_{D2}}{\sqrt{C_{D1}^2 + C_{D2}^2}} \sqrt{\Delta C_{P, total}} \quad (\text{Equation 6.3})$$

If the discharge coefficients are identical for the two openings equation 6.2 is obtained.

Wind direction	Mean pressure coefficient Wind side	Mean pressure coefficient Leeward side	Discharge coefficient	Relative airflow rate (q/(A·U <sub>ref</sub> ))
0	0.64	-0.46	0.6	<b>0.44</b>
30	0.58	-0.51	0.6	<b>0.44</b>
60	0.25	-0.62	0.6	<b>0.40</b>

**Table 6.2 Measured mean pressures and corresponding airflow rates when using the common flow equation and discharge coefficients of 0.6.**

Comparing the values of the relative airflow rates described in Table 6.2 with the measured depicted in Figure 6.33, Figure 6.34 and Figure 6.35 it is clear that the correspondence is varying, but the values found from the standard flow equation seem to give acceptable averages.

This can also be illustrated by considering the discharge coefficients found from the measurements of the airflow rates and the local pressures. Figure 6.36 shows these measured discharge coefficients in the middle of the building for wind directions of 0, 30 and 60 degrees compared to the

standard value of 0.6. The discharge coefficients are depicted in the same way as the airflow in Figure 6.33 - Figure 6.35, all values can be found as spreadsheet data on the CD-rom. It should be emphasized that the depicted  $C_D$  values are calculated using the above mentioned expression i.e. disregarding the internal pressure and only using the total local pressure drop across the building and assuming that the discharge coefficients for the up- and downstream openings are identical.

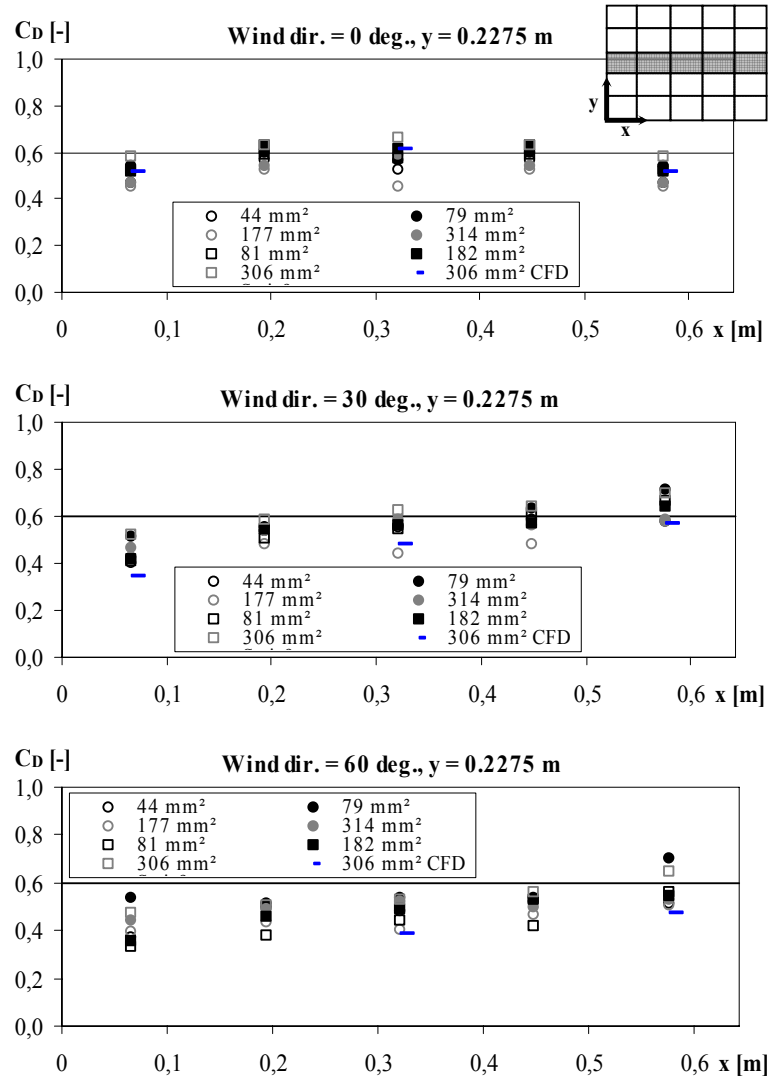


**Figure 6.36 Discharge coefficients found from local total pressure drop across the sealed building.**

Figure 6.36 shows that a value of  $C_D = 0.6$  may be misleading especially when the building is placed at an angle compared to the flow and that there

exists a large variation in the magnitude of the measured discharge coefficients. Comparing all measurements it is found that the highest value is 0.84 and the minimum value is 0.25, see spreadsheet on the CD-rom.

In connection to the discharge coefficients depicted in Figure 6.36 it should be emphasised that the internal pressure has been disregarded and the measured  $C_D$  value does not represent the actual value for the individual openings (inlet and outlet). Due to the internal pressure being higher than the mean value of the pressure on the leeward side and on the windward side, the jet from the inlet opening is not completely dissolved and there exists a conservation of kinetic energy. This affects the value of the discharge coefficients for the individual opening. For all cases it has been found that the pressure drop across each opening is highest at the inlet or the upwind opening, this means that the discharge coefficient is smaller for the opening placed upstream compared to the one placed downstream. The highest discharge coefficient at the downstream opening found from the measurements using a 0 wind incident angle is 0.91 where the corresponding  $C_D$  value at the upstream opening is 0.66. When the flow is angled compared to the building the differences in the upstream and downstream discharge coefficients are generally highest for the openings located in the downstream part of the building.

The values of the discharge coefficients can be found in the spreadsheet located on the CD-rom.

Comparing the relative airflow rates to the local pressure differences across the whole building could give an indication of the dependency of the discharge coefficient on the pressure difference. Figure 6.37 shows the relative airflow rate depicted as a function of the local pressure difference found from the sealed building. The depiction shows measured and predicted values with a square opening of 316 mm<sup>2</sup> for different wind incident angles.

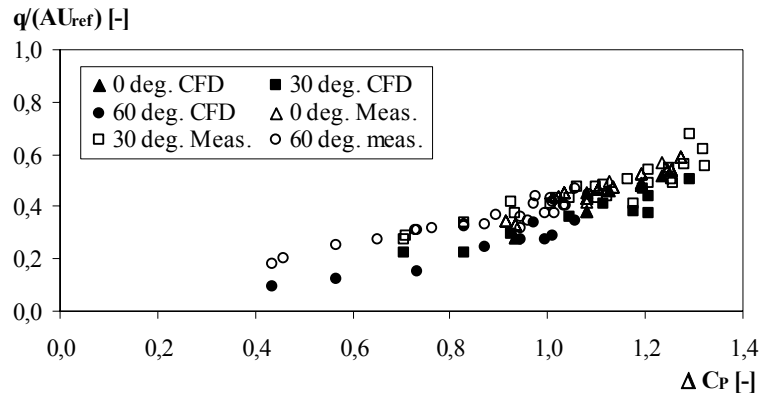


**Figure 6.37 Relative airflow rate as a function of the local pressure difference for measurements and predictions for an opening size of 316 mm<sup>2</sup>.**

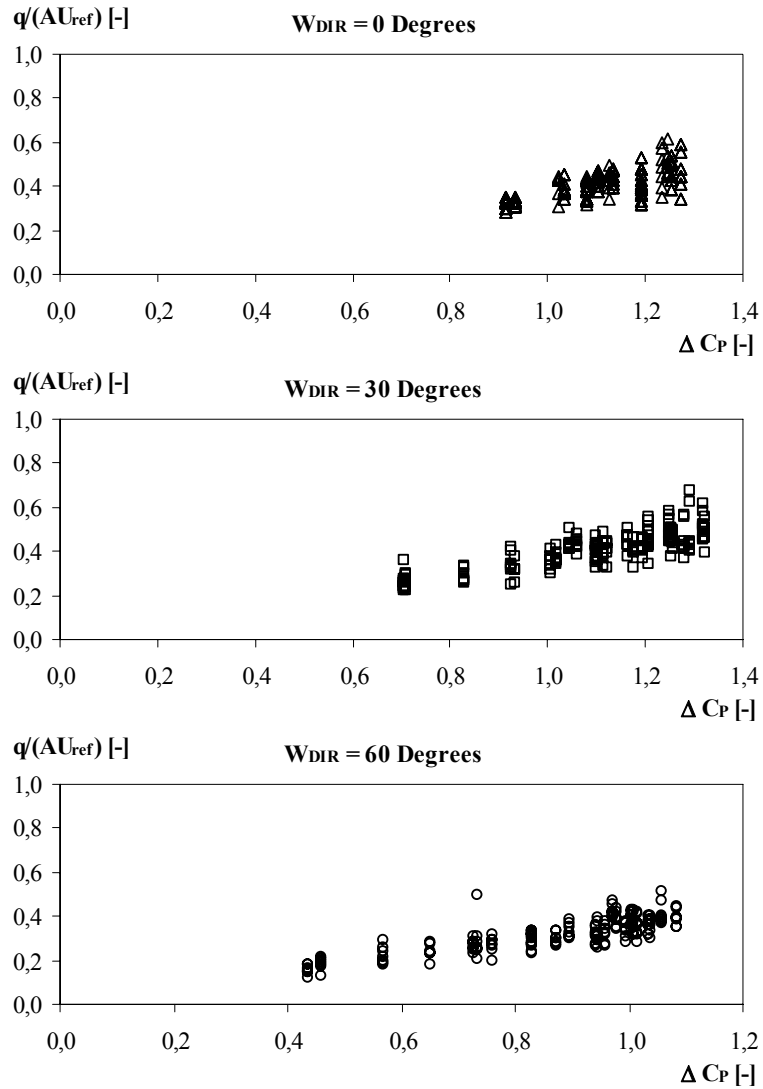
There seems to exist a linear dependency between the airflow rate and the surface pressure difference which does not correspond to the fact that the airflow should be proportional to the squareroot of the pressure difference. This linear dependency seems also to be independent of the flow direction. The pattern is the same for both the measurements as well as the predictions despite the generally smaller airflow rates found in the predictions. This deviance is connected to the difference in the airflow pattern since there exists a connection between the location of high pressure on the windward side (resulting in a high total pressure difference) and the angle at which the flow enters the room. This fact results in the openings located far off the location of highest pressure having airflow rates that are relatively smaller than the comparative ones placed closer to this location.

Figure 6.38 shows all measurements of the relative airflow rates divided into different wind directions as functions of the local surface pressure difference.

The dependency of the relative airflow rate seems also in Figure 6.38 to be a linear function of the total local pressure difference for the individual wind directions are considered. This being for all measurements of different

opening sizes and there are large deviancies airflow rates. If a linear fit is applied to the measurements shown in Figure 6.38 a proportionality constant of 0.36 - 0.37 is found for all three wind directions, this implies that with an acceptable approximation that the airflow rate can be described by:

$$\frac{q}{A \cdot U_{ref}} = 0.37 \Delta C_{p,local}$$



**Figure 6.38** Relative airflow rates for wind directions of 0, 30 and 60 degrees as functions of the local pressure difference across the whole building.

Another way of describing the airflow rate is as mentioned in an earlier chapter the use of the catchment area. This is however not immediately

applicable since the building is placed in a boundary layer and the reference velocity is not constant but varies and the air flowing through the opening does not necessarily originate from the same height (in the free boundary layer) compared to where the opening is placed. However in section 6.4.2 the upwind streamlines of the air flowing through the openings from CFD were depicted and it was found that the air originates from a finite area and that the height from where air originates in the free boundary layer only to some extent is dependent on the location of the opening. This height is approximately independent at a wind direction of 0 degrees varying only from  $0.65 - 0.69 \cdot H_{\text{Building}}$ , whereas the height varies more when an angled flow is applied ( $0.58 - 0.75 \cdot H_{\text{building}}$  for a wind direction of 30 and  $0.31 - 0.81 \cdot H_{\text{building}}$  for a wind direction of 60). This is due to the change in pressure distribution since the area of highest pressure is extended downwards with the flow angle, see Figure 6.14.

The corresponding catchment areas are depicted in Figure 6.39 as a function of the horizontal location in the building for different vertical heights in the building.

When the flow is angled the height from which the air originates in the undisturbed boundary layer varies and therefore the reference velocity varies, which makes not only catchment area a function of the location of the opening, but also the reference velocity.



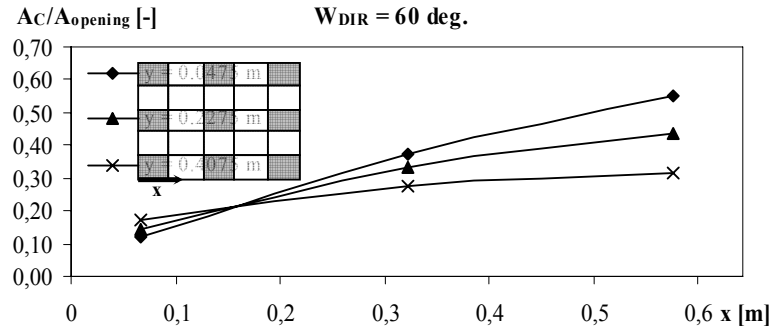
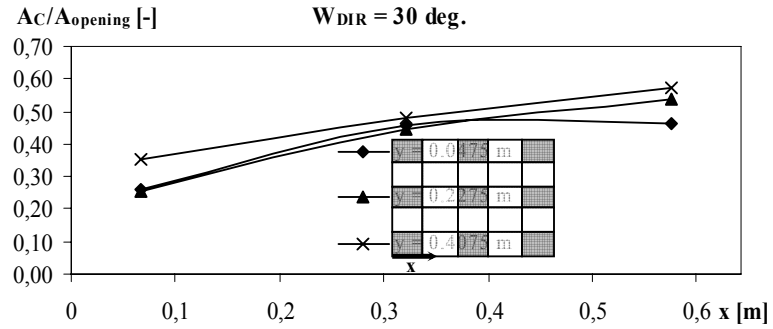
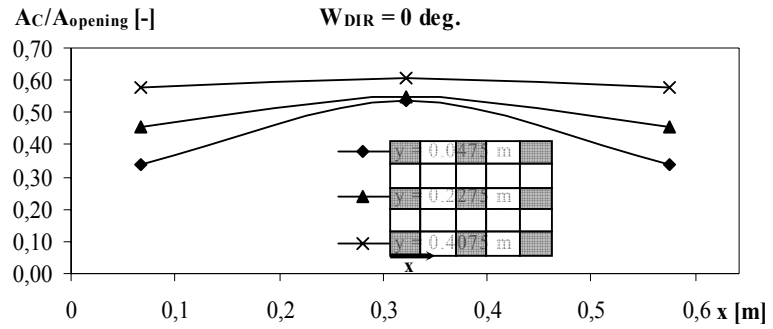


Figure 6.39 Relative catchment area as a function of the horizontal location in the building for wind directions of 0, 30 and 60 degrees.

## 6.5. DISCUSSION

The airflow through openings placed in a cross ventilated scale model of a building has been investigated both in a wind tunnel as well as by means of numerical predictions.

The predictions using a wind direction of  $0^\circ$  showed an airflow pattern consisting of streamlines entering the room in which the openings were located, that originated from approximately the same upstream area in the undisturbed boundary layer. This is caused by the air reaching the vicinity of the stagnation point on the building and from here distributed over or around the building or if openings are present into the building. When the building was exposed to an angled flow the streamlines did not completely originate from the same area in the undisturbed boundary layer since the “stagnation point” (or the area of highest pressure on the windward side) was a large area from which the air was distributed. This means that the vertical location of the opening has an influence on where the air originates. This dependency increased with the magnitude of the wind direction.

The influence that the opening has on the pressure distribution has been analysed and it is found that an opening in the building effects the surface pressure distribution in the vicinity of the opening.

Figure 6.40 shows a schematic outline of the change in horizontal pressure distribution for wind directions of 0 and 30 degrees when openings are placed in the building.

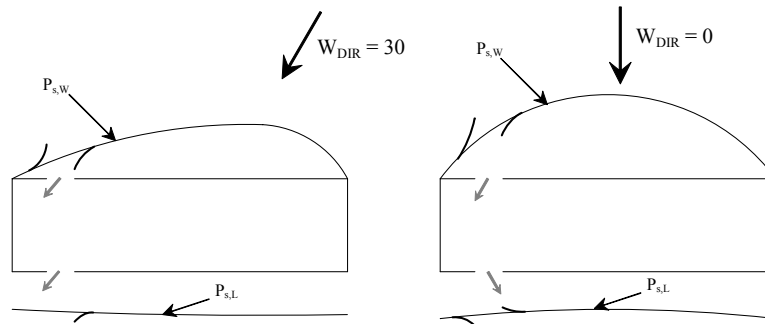


**Figure 6.40 Outline of the horizontal pressure distribution on building and the effect of cross ventilated openings.**

The static surface pressure distribution seems to be altered due to the flow entering the opening having a higher velocity in the part of the opening located close to side where the pressure is smaller and in turn a lower velocity in the part where the static pressure is higher. An indication of the described velocities is given in Figure 6.40. This shows that the direction of the flow is altered for a wind direction of 0 degrees from the upstream opening to the downstream one. The opposite is the case for the angled flow where the flow has the same orientation.

The alteration in the pressure distribution is very dependent on the location of the opening since if the opening is placed in the horizontal middle of the building and exposed to a perpendicular wind direction there will be a decrease or no change in the pressure on both sides of the opening (horizontal sides, there might be a difference in the vertical pressure. When the building is exposed to an angled flow the change in the pressure will depend on the location of the highest pressure on the windward side since this is where the flow divides and therefore determines the flow direction through the opening, which as explained is closely linked to the pressure distribution.

The internal pressure for various opening sizes was not found in any of the cases to be the mean of the pressure on the windward and leeward sides found from the sealed building. This may however be due to the fact that the pressure is altered when an opening is present and that the mean may be

smaller than expected. The distance between the openings in combination with the opening size should also have an impact on the internal pressure due to the conservation of kinetic energy between the openings.

The airflow rate through the openings is found to be dependent on the wind direction and the location of the openings in the building. Discharge coefficients are calculated based on the local pressure difference across the whole building and assuming that the discharge coefficients are identical for both openings (see equation 6.2) leading to values that are close to 0.6 for a wind direction of  $0^\circ$  but however smaller for the openings located at the sides than the ones in the middle and also with a variation in the vertical height. When the building is exposed to an angled flow the discharge coefficients are higher for the openings located in the upstream part of the building compared to the ones located further downstream. In addition to this the magnitude of the discharge coefficient also has a larger variation than when the flow is perpendicular to the building.

If the discharge coefficients are calculated individually (for both the inlet as well as the outlet) and hereby including the internal pressure the discharge coefficient for the outlet obtains a higher value than for the inlet due to the internal pressure being smaller than half the total difference.

It is found that by depicting the relative airflow rate as a function of the local pressure difference across the building that it is possible to describe the relative airflow rate with acceptable approximation as a linear function of the local pressure difference across the building independently of the wind direction. Figure 6.41 shows all measurements of the airflows depicted as a function of the local pressure difference across the building compared to the found linear relationship. In addition to this a comparative line is added calculated using the standard flow equation (based on the local pressure differences). The mean pressure differences for the 3 wind directions are also shown in order to compare the standard approach to the measurements (the intersection of these lines and the non-linear line describes these values).

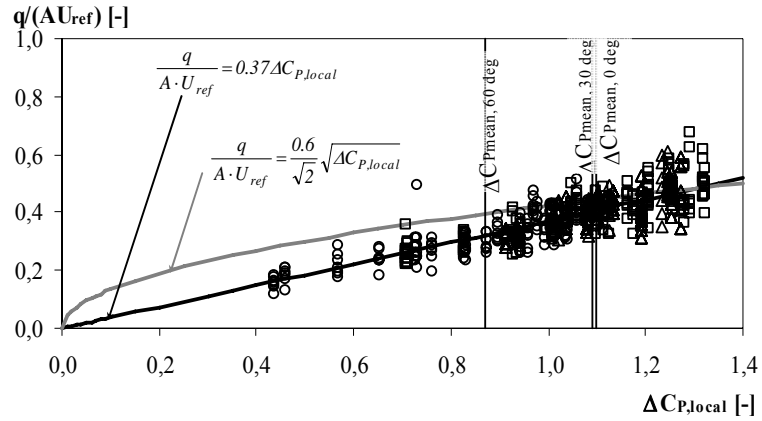


**Figure 6.41** Relative airflow rate for all measurements vs. the local pressure difference across the building.

There are still large deviances between the measurements and the approximated lines, but the figure clearly shows the necessity of applying the local pressure difference instead of a mean value. The deviances present are to some extent due to measurement errors and to some extent differences caused by the differences in the airflow for different size openings. Additionally despite the pressure difference being dependent on the location in the building the influence of the location is still not completely accounted for.

## **7. CONCLUSIONS AND DISCUSSION**

The conclusion is divided into a general discussion of the obtained results and a description of recommendations for future work.

### **7.1. GENERAL DISCUSSION**

The flow equation used in the design of natural ventilation is derived from the Bernoulli equation based on the flow through an orifice placed in pipe flow. This fact makes the appliance to the flow through an opening placed in a building envelope questionable since it is not immediately confined, however results from the present analysis have shown that there exists a “flowtube” which can be traced back to the undisturbed flow. Normally the orifice to pipe area ratio is included in the orifice equation, whereas it is disregarded in the flow equation used in the design of natural ventilation due to the area of the building being much larger than the area of the opening. This seems to be a misleading approach due to the existence of the “flowtube”.

The traditional approach of determining the wind driven airflow through building envelope openings is to measure or predict the pressure distribution on the sealed building. In order to calculate the airflow rate through an opening the average surface pressures are applied in the common flow equation. This approach seems questionable especially when large openings are applied since the pressure distribution can be altered dramatically. The maximum surface pressure difference across the object/building in chapter 5 is however found to be approximately of the same magnitude regardless of the porosity. The corresponding discharge coefficients based on the average surface pressures from the sealed objects are also approximately in the expected interval of 0.6 – 1.0. This is however across the whole object which in turn means that it covers 2 openings and assuming that the discharge coefficient is the same across the two openings this leads to  $C_D$  values in the interval 0.85 – 1.4. The reason for the high magnitude of these values is a combination of the average surface pressures being used and the omission of the area ratio in the equation.

Another matter of interest is the flow contact that can exist between openings which the traditional flow equation cannot account for since it will lead to unrealistic values of the discharge coefficient.

It is found that the Bernoulli equation is still valid for flow through building openings but that leaving out the opening area to flow tube area ratio may be misleading, and that the preservation of kinetic energy (when flow contact is present) should be included.

Flow through openings is a flow process consisting of a whole sequence of elements; separation from the external flow (selection procedure) – inflow – internal flow – outflow and reuniting with the external flow. Therefore it should be dealt with as a flow problem.

The catchment area is the cross section perpendicular to the wind containing the streamlines in the undisturbed air stream upwind which pass through the building. This area quantifies the selection procedure. The standard equations used for calculating the flow through cracks as a function of a pressure drop is based on the assumption that the catchment area is infinite. The catchment area is dependent on the resistance to the wind offered by the building. The more streamlined the building is the lesser is the flow through the openings.

When one has small openings in a building offering a large resistance to the wind (large drag) the catchment area may be larger than the area of the opening.

If the opening areas are equal then the largest pressure drop occur in the windward opening. With unequal opening areas, the largest pressure occurs across the smallest opening as expected. However, the flow rate is dependent on the order between the openings.

The standard approach is to relate the flow to a pressure difference across the building envelope. A better approach might be to regard the flow through openings as a flow catchment problem. The flow rate is expressed as a reference velocity times the catchment area. Then the result may be conveniently expressed as catchment area divided by the opening area.

The airflow through openings placed in a cross ventilated scale model of a building has been investigated when exposed to a boundary layer type flow. The predictions using a wind direction of  $0^\circ$  showed an airflow pattern consisting of streamlines entering the room in which the openings were located, that originated from approximately the same upstream area in the undisturbed boundary layer. This is caused by the air reaching the vicinity of the stagnation point on the building and from here distributed over or around the building or if openings are present into the building. When the building was exposed to an angled flow the streamlines did not completely originate from the same area in the undisturbed boundary layer since the “stagnation point” has become a “stagnation line” from which the air was distributed. This means that the vertical location of the opening has an influence on where the air originates. This dependency increased with the magnitude of the wind direction.

The influence that the opening has on the pressure distribution has been analysed and it is found that an opening in the building effects the surface pressure distribution in the vicinity of the opening. The alteration in the pressure distribution is very dependent on the location of the opening since if the opening is placed in the horizontal middle of the building and exposed to a perpendicular wind direction there will be a decrease or no change in the pressure on both sides of the opening. When the building is exposed to an angled flow the change in the pressure will depend on the location of the highest pressure on the windward side since this is where the flow divides and therefore determines the flow direction through the opening, which is closely linked to the pressure distribution.

The internal pressure for various opening sizes was not found in any of the cases to be the mean of the pressure on the windward and leeward sides found from the sealed building. This may however be due to the fact that the pressure is altered when an opening is present and that the mean may be smaller than expected. The distance between the openings in combination with the opening size should also have an impact on the internal pressure due to the conservation of kinetic energy between the openings.



The airflow rate through the openings is found to be dependent on the wind direction and the location of the openings in the building. Discharge coefficients are calculated based on the local pressure difference across the whole building and assuming that the discharge coefficients are identical for both openings leading to values that are close to 0.6 for a wind direction of  $0^\circ$  but however smaller for the openings located at the sides than the ones in the middle and also with a variation in the vertical height. When the building is exposed to an angled flow the discharge coefficients are higher for the openings located in the upstream part of the building compared to the ones located further downstream. In addition to this the magnitude of the discharge coefficient also has a larger variation than when the flow is perpendicular to the building.

If the discharge coefficients are calculated individually (for both the inlet as well as the outlet) and hereby including the internal pressure the discharge coefficient for the outlet obtains a higher value than for the inlet due to the internal pressure being smaller than half the total difference.

It is found that by depicting the relative airflow rate as a function of the local pressure difference across the building that it is possible to describe the relative airflow rate with acceptable approximation as a linear function of the local pressure difference across the building independently of the wind direction.

The appliance of a catchment area for the calculation of airflow rates through cross ventilated openings is valid but connected with some difficulty due to the variation in the reference velocity caused by the flow distribution from a stagnation line (instead of a stagnation point) when the building is exposed to an angled flow.

## **7.2. RECOMMENDATIONS FOR FUTURE WORK**

The thesis gives an indication of some of the factors that are important in the calculation of the airflow rate through openings placed in a building

exposed to wind driven natural ventilation. However a general model flow equation or the possible alteration to the existing flow equation is left untreated. This is a subject which to some extent is the end goal or purpose of the analysis and needs some further work but which the present analysis could be a contribution to.

The flow contact or the transfer of kinetic energy between openings is found in the present analysis to be of importance in the calculation of the airflow through openings in wind driven natural ventilation. The transfer of kinetic energy is linked to the determination of the opening being small or large, a matter dependent on a large number of variables of which only some have been investigated. A complete picture regarding the determination of whether an opening can be considered small or large is essential for the determination of the airflow rate through openings placed in wind driven naturally ventilated rooms. Therefore a further analysis of factors influencing the flow contact between openings is needed. One such factor is the distance between the openings combined with the size of the openings which has not been considered in the thesis.

## DANISH SUMMARY

Luftstrømningen gennem åbninger placeret i bygninger med vind dreven naturlig ventilation er undersøgt med det formål, at belyse de faktorer, der influerer luftmængden gennem åbninger. Ligningen, som benyttes i dimensionerings henseende til beregning af luftmængden gennem åbninger, er desuden analyseret i tæt sammenhæng med disse faktorer, for at bestemme dennes brugbarhed og berettigelse.

I kapitel 5 undersøges geometrisk simple modeller med det formål, at analysere effekten af en kombination af åbningsstørrelse, den geometriske form af objektet og placeringen af åbningerne. Geometrisk simple størrelser placeret i en ensartet strømning blev benyttet, for at holde antallet af variable på et minimum. De simple geometriske størrelser bestod af en cirkulær skive med varierende åbningsstørrelse placeret i midten såvel som placeret excentrisk, samt en cylinder af samme diameter i forhold til skiven ligeledes med varierende åbningsstørrelse placeret både i midten og excentrisk. Analysen af cylinder tilfældet er desuden forlænget med forskellige op- og nedstrøms åbningsstørrelser. Analysen består af målinger og numerisk simulering vha. *Computational Fluid Dynamics*. Den eksperimentelle del involvere målinger af tryk fordeling på luv- og læsiden af objekterne og desuden indeni cylinderen. Luftmængden gennem åbningerne er fundet vha. målinger af hastighedsfordelingen på læsiden af objekterne. Simuleringerne er foretaget både i sammenlignings henseende, men også for at opnå et mere komplet billede af tryk- og strømningsforhold i og omkring åbningerne.

Det er fundet, at store åbninger har en ikke uvæsentlig indflydelse på trykfordelingen, men at den maksimale trykforskel over bygningen eller objektet forbliver næsten uændret uanset porøsitet. Til gengæld ændres trykket fundet på en centerlinie igennem åbningerne markant ved stigende porøsitet. Når store åbninger betragtes ved krydsventilation, vil den betydeligste del af trykfaldet ske over den "første" åbning, dvs. den åbning som er placeret mod strømmen.

Denne forskel i trykfaldet over åbningerne resulterer i flere tilfælde i urealistiske strømningskoefficienter ( $C_D$ -værdier) for den "sidste" åbning, dvs. åbningen placeret nedstrøms. For den "første" åbning er strømningskoefficienten i alle tilfælde beliggende i intervallet 0.6 - 1.0. Beregnes en total strømningskoefficient i cylindertilfældet, findes et tilsvarende interval, dette dækker dog over to åbninger, og værdierne er derfor diskutabile. Baggrunden for de urealistiske strømningskoefficienter for den "sidste" åbning er overførelsen af kinetisk energi fra den "første" åbning.

Gennem observationen af "strømningsrør" er det fundet muligt i stedet at beskrive luftstrømningen gennem åbninger, som en strømningsproces vha. et indfangningsareal (*Catchment area*). Luftmængden beskrives herved som indfangningsarealet multipliceret med en reference hastighed.

Det er fundet muligt at beskrive luftstrømningen gennem åbninger vha. den gængse strømningsligning (baseret på Bernoullis ligning), men at udelade arealforholdet mellem åbningsarealet og arealet af strømningsrøret kan resultere i afvigelser, og at såfremt bevarelse af kinetisk energi (strømningskontakt mellem åbninger) er tilstede, er dette nødvendigt at medtage i ligningen.

Kapitel 6 omhandler en analyse af krydsventilation af rum placeret i en bygning anbragt i en grænselagsstrømning. Bygningen består af 5 gange 5 rum af ens størrelse. Analysen fokuserer på indflydelsen af placeringen og størrelsen af åbningerne i bygningen. Analysen består af målinger i en vindtunnel og numeriske simuleringer. Modellen i vindtunnelen var udført i plexiglas og grænselagsstrømningen eller vindprofilet skabt af ruhedselementer placeret i vindtunnelen. Det målte hastighedsprofil i vindtunnelen blev benyttet som en randbetingelse i de numeriske beregninger. En detaljeret analyse af trykfordelingen og åbningernes indflydelse på denne blev foretaget. Luftmængden gennem åbningerne for forskellige placeringer af disse blev sammenlignet, både som en funktion af placeringen, men også som funktion af den lokale trykdifferens. Faktorer

inkluderet i analysen var størrelse og placering af åbninger i kombination med forskellige vindretninger.

Ud fra en betragtning af luften som strømmer gennem åbningerne, kan det konkluderes, ved en vindretning som er vinkelret på bygningen og uanset placeringen af åbningen i bygningen, at denne kan spores tilbage til tilnærmelsesvist det samme område i den frie grænselagsstrømning. Dette skyldes, at luften fordeles fra stagnationspunktet enten over, udenom eller igennem åbningerne. Når bygningen er placeret med en vinkel i forhold til strømningsretningen, kan strømmlinierne ikke helt spores tilbage til det samme område, hvilket skyldes at stagnationspunktet i stedet er en stagnationslinie hvorfra luften fordeles. Dette betyder følgelig, at den lodrette placering af åbningen har indflydelse på hvorfra luften stammer. Denne afhængighed er stigende med forøget vindretning, da stagnationslinien ændres.

Det er fundet, at åbningen har indflydelse på trykfordelingen i nærheden af åbningen både på luv- og læside og at denne er afhængig af strømningen i og omkring åbningen. Trykket i de ventilerede rum blev ikke fundet til at være middelværdien af de lokale tryk på luv- og læside af bygningen uden åbninger uanset åbningsstørrelsen. Dette lader dog til, at skyldes, at selv ved den mindste åbning overføres kinetisk energi og den må derfor betragtes, som værende en "stor" åbning.

Luftmængden gennem åbningerne er fundet, at være afhængig af både vindretningen såvel som placeringen af åbningen i bygningen. Strømningskoefficienter er beregnet baseret på den lokale trykforskel (for placeringen af åbningen i den "lukkede" bygning) og under forudsætning af, at denne er ens for de 2 åbninger, hvilket resultere i værdier tæt på 0.6 ved en vindretning på 0 grader. Når strømningsretningen er vinklet i forhold til bygningen, bliver de resulterende strømningskoefficienter større for åbninger placeret i den del af bygningen som er opstrøms i forhold til de som er placeret længere nedstrøms. Beregnes strømningskoefficienterne individuelt, dvs. medtages det interne tryk, findes værdier for den "første" åbning som er mindre end for den "sidste" grundet det forholdsmæssigt lave interne tryk.

### Danish summary

---

Det er fundet at den relative luftmængden med god tilnærmelse kan beskrives som en linear funktion af den lokale trykforskel (hvor åbningen er placeret) uafhængigt af vindretningen, og ikke som ventet som kvadratroden af denne.

## REFERENCES

(Allard et al., 1998)

Allard, F, Santamouris, M, Alvarez, S, Dascalaki, E, Guarracino, G, Maldonado, E, Salvatore, S, Vandaele, L, *Natural ventilation in buildings – A design handbook*, James & James Ltd., 1998, ISBN: 1 873936 72 9.

(Andersen et al., 1982).

Andersen, B., Eidorff, S., Hallgreen, L., Lund, H., Pedersen, E., Rosenørn, S., and Valbjørn, O., *Vejrdata for VVS og energi. Dansk referenceår TRY*. SBI-rapport 135. Statens Byggeforskningsinstitut, Hørsholm, DANMARK, 1982.

(Andersen et al., 2000)

Andersen AA., Bjerre M., Chen ZD., Heiselberg P., Li Y. Experimental modelling of wind opposed buoyancy-driven building ventilation. Proceedings of the 21st AIVC Conference, Netherlands, September 26–29, 2000.

(Andersen et al., 2002)

Andersen, KT., Heiselberg, P. and Aggerholm, S., *Naturlig Ventilation i Erhvervsbyggerier – Beregning og Dimensionering, By og Byg Anvisning 202*, Statens Byggeforskningsinstitut, 2002, ISBN: 87-563-1128-1.

(ASHRAE fundamentals, 1993)

ASHRAE Handbook of Fundamentals, New York, ISBN: 0-910110-97-2, 1993.

(Awbi, 1991)

Awbi, H., *Ventilation of Buildings*, First Edition, Chapman and Hall, London, 1991, ISBN: 0-419-15690-9.

(Bakke, 1957)

Bakke, P., An Experimental Investigation of a Wall Jet, *Journal of Fluid Mechanics*, 2, pp. 467-472, 1957.

(Baskaran, 1992)

Baskaran, A. and Stathopoulos, T., Influence of Computational Parameters on the Evaluation of Wind Effects on the Building Envelope, *Building and Environment*, Vol. 27, 1, pp. 39-49.

(Baturin, 1972)

Baturin, VV., *Fundamentals of Industrial Ventilation* (English edition), Third enlarged edition, Pergamon Press Ltd., 1972.

(Bjerregaard et al., 1980)

Bjerregaard, E. and Nielsen, F., *Vindmiljø omkring bygninger*, SBI-Anvisning 128, Statens Byggeforsknings Institut, Hørsholm, Denmark, ISBN: 87-563-0380-7.

## References

---

(Bjørn et al., 2001)

Bjørn, E., Jensen, J., Larsen, J., Nielsen, P.V., Heiselberg, P. Improvements of Thermal Comfort in a Naturally Ventilated Office. *Proceedings of the 21<sup>st</sup> AIVC Conference, Den Haag, The Netherlands, September 22 – 25, 2000, AIVC, United Kingdom.*

(BS1042, 1964)

British Standard 1042: Part 1: 1964, Methods for the measurement of fluid flow in pipes, Part 1: Orifice plates, nozzles and venturi tubes, British Standards Institution, London, 1964.

(Carrilho da Graca et al., 2002)

Carrilho da Graca, G., Linden, P.F., Contributions to simplified modelling of building Airborne Pollutant removal, Proceedings of the 9th international conference on indoor air quality and climate, Monterey, California, 2002\*

(Chen et al., 2000)

Chen, Z.D., Li, Y. and Mahoney, J., Natural ventilation in an enclosure induced by a heat source distributed uniformly over a vertical wall, *Building and Environment*, vol. 36, 4, 2000.

(Chou, 1945)

Chou, P.Y., On the Velocity Correlations and Solution of the Equations of Turbulent Fluctuation, *Journal of Applied Mathematics*, 3 (1), pp. 38-54.

(Davidson and Nielsen, 1996)

L. Davidson, P. Nielsen, Large eddy simulation of the flow in a three-dimensional ventilation room, 5th International Conference on Air Distribution in Rooms, ROOMVENT96, July 17–19, 1996.

(DIN 1952, 1982)

DIN 1952, V.D.I. Durchflussregeln, Regeln für die Durchflussmessung mit genormten Düsen und Blenden, Verein Deutscher Ingenieure, Düsseldorf, 1963 (7<sup>th</sup> edition)

(Etheridge and Sandberg, 1996)

Etheridge D; Sandberg M (1996) “ Building Ventilation: Theory and Measurement” John Wiley and Sons, Chichester, England, ISBN: 0 471 96087 X.

(Fluent, 1998)

Fluent 5 – User’s Guide, Fluent Inc., Lebanon, New Hampshire, July 1998.

(Fluid Meters, 1959)

Fluid meters, their theory and application, A.S.M.E. Fluids committee report, 5<sup>th</sup> edition (1959)



## References

---

(Fracastoro and Perino, 2001)

Fracastoro GV., Perino M. (2001), WG-B5 IEA Annex 35 Technical Report “Wind Induced Airflow through Large Openings: A Numerical Analysis”, Politecnico di Torino

(Freskos, 1998)

Freskos, GO., Influence of Various Factors on the Prediction Furnished by CFD in Cross-Ventilation Simulation, Proceedings of Roomvent 98, 6th International Conference on Air Distribution in Rooms, June 1998, Stockholm, Sweden, Volume 1, pp 483-490.

(Heiselberg et al., 1999)

Heiselberg, P., Dam, H., Sørensen, L.C., Nielsen, P.V., Svidt, K. Characteristics of Air Flow through Windows. *Proceedings of the First International Forum on Natural and Hybrid Ventilation, HybVent Forum 99, 09/1999, Sydney, Australia.*

(Heiselberg et al., 2000)

Heiselberg, P., Svidt, K., Nielsen, P.V. Windows – Measurements of Air Flow Capacity. *Proceedings of ROOMVENT 2000, July 9-12, Reading, UK.*

(Heiselberg et al., 2001)

Heiselberg, PK., Svidt, KS. and Nielsen, PV., Characteristics of Airflow from Open Windows, *Building and Environment*, 36, pp. 859-869, 2001.

(Holman, 1994)

Holman, JP., *Experimental Methods for Engineers*, Sixth Edition, McGraw-Hill Inc., 1994, ISBN: 0-07-113345-3.

(Hunt et. al., 2000)

Hunt, G. and Holford, JM., The discharge coefficient – Experimental Measurement of a Dependence on Density Contrast, Proceedings 21<sup>st</sup> AIVC Annual Conference “Innovations in Ventilation Technology”, 2000.

(Iino, 1998)

Iino, Y., Kurabuchi, T., Kobayashi, N., Arashiguchi, A., Study on Airflow Characteristics in and around Building Induced by Cross-Ventilation using Wind Tunnel Experiment and CFD Prediction, Proceedings of Roomvent 98, 6th International Conference on Air Distribution in Rooms, June 1998, Stockholm, Sweden,, Volume 2, pp. 307-314.

(IPCC, 2001)

Climate Change 2001, IPCC Third assessment report, Intergovernmental panel on Climate Change, 2001.

## References

---

(Jensen and Larsen, 2000)

Jensen, JP. and Larsen, JT., Analysis of Flow in Natural Ventilation – In Danish, (Analyse af Strømningsforhold ved Naturlig Ventilation), Master thesis, Aalborg University, 2000.

(Jensen True et al. 2002)

Jensen True, JP., Heiselberg, P., and Nielsen, PV., Numerical Simulation of Air Flow Through Large Openings, IEA Annex 35 Technical Report, Aalborg University, 2002.

(Jensen True et al., 2002)

Jensen JP., Heiselberg P., Nielsen PV., (2002) “Numerical Simulation of Air Flow through large openings”, Proceedings Roomvent 2002, Copenhagen, Denmark

(Jensen True et al., 2003)

Jensen True, JP., Sandberg, M., Heiselberg, P., Nielsen, PV., Wind Driven Cross-flow Analysed as a Catchment Problem and as a Pressure Driven Flow, International Journal of Ventilation special edition, 2003.

(Jiang et al., 2001)

Jiang, Y. and Chen, Q., Study of Natural Ventilation by Large Eddy Simulation, Journal of Wind Engineering and Industrial Aerodynamics, 89, pp. 1155-1178, 2001.

(Jiang et al., 2002)

Jiang, Y. and Chen, Q., Effect of Fluctuating Wind Direction on Cross Natural Ventilation in Buildings from Large Eddy Simulation, Building and Environment 37, pp. 379-386, 2001.

(Jiang et al., 2003)

Jiang, Y., Alexander, D., Jenkins, H., Arthur, R. And Chen, Q., Natural ventilation in Buildings: Measurement in a wind tunnel and Numerical Simulation with Large Eddy Simulation, Journal of wind Engineering and Industrial Aerodynamics 91 pp. 331-353, 2003.

(Johansen, 1930)

Johansen, F.C., The influence of pipe diameter on orifice discharge coefficients, Engineer 149, 1930.

(Karabuchi et al., 2002)

Karabuchi, T., Ohba, M., Fugo, Y., Endoh, T., Local similarity model of cross-ventilation, Proceedings of The 8<sup>th</sup> international conference on air distribution in rooms, RoomVent 2002, Copenhagen.

## References

---

(Launder and Spalding, 1974)

Launder, B. E., Spalding, D. B., *The numerical computation of turbulent flows*, Computer Methods in Applied Mechanics and Engineering, 3, pp. 269-289, 1974.

(Launder et al., 1972)

Launder, BE., Morse, A., Rodi, W. and Spalding, DB., *The Prediction of Free Shear Flows – A comparison of Six Turbulence Models*, Imperial College Mechanical Engineering Department, London, 1972

(Launder et al., 1975)

Launder, BE., Reece, GJ. and Rodi, W., *Progress in the Development of a Reynolds Stress Turbulence Closure Model*, Journal of Fluid Mechanics, Vol. 68 (3), pp.537-567.

(Laws, 1978)

Laws EM., Livesey JL. (1978), "Flow through Screens" Ann. Rev. Fluid Mech. (1978) pp. 247-266

(Li et al., 1994)

Li, Y., and Holmberg, S., *General flow and thermal boundary conditions in indoor air flow simulation*, Building and Environment, Vol. 29, pp. 275 – 281, 1994.

(Li et al., 2001)

Li, Y., Delsante, A., Chen, Z., Sandberg, M., Andersen, A., Bjerre, M. and Heiselberg, P., *Some examples of solution multiplicity in natural ventilation*, Building and Environment Vol.36 Issue.7, pp. 851-858, 2001.

(McComb, 1990)

McComb, WD., *The physics of fluid turbulence*. Clarendon Press Oxford, 1990.

(McRee et al., 1967)

McRee, DI. and Moses, HL., *The Effect of Aspect Ratio and Offset on Nozzle Flow and Jet Reattachment*, Advances in Fluidics, The 1967 Fluidics Symposium, ASME, 1967.

(Monin and Yaglom, 1971)

Monin, A. S. and Yaglom, A. M.: 1971, *Statistical Fluid Mechanics: Mechanics of Turbulence*, Vol. 1, The MIT Press, Cambridge, MA, 1971.

(Müllejans, 1963)

Müllejans, H., *Über die Äntlichkeit der nicht-isothermen Strömung und den Wärmeübergang in Räumen mit Strahl Lüftung*, PH.D. Thesis, TH. Aachen, 1963.

(Murakami et al., 1989)

Murakami, SS. And Moshida, A., *Three Dimensional Numerical Simulation of*

## References

---

- Turbulent Flow Around Building Using the k- $\epsilon$  Turbulence Model, *Building and Environment*, Vol. 24, 1, pp. 51-64, 1989.  
(Murakami et al., 1991)
- Murakami, S.; Kato, S.; Akabayashi, S.; Mitsuanti, K. (1991) Windtunnel Tests on Velocity-Pressure Field on Cross-Ventilation with open Windows *ASHRAE Transactions: Symposia*, Vol , pp. 525-538  
(Murakami et al., 1992)
- Murakami, S., Mochida, A., Hayashi, Y. & Sakamoto, S., Numerical study on velocity-pressure field and wind forces for bluff bodies by k- $\epsilon$ , ASM and LES. *Journal of wind Engineering and Industrial Aerodynamics* 41- 44, pp. 2841-2852, 1992.  
(Murakami et al., 1993a)
- Murakami, S., Comparison of Various Turbulence Models Applied to a bluff body, *Journal of wind Engineering and Industrial Aerodynamics* 46 & 47, pp. 21-36, 1993.  
(Murakami et al., 1993b)
- Murakami, S., Mochida, A. and Ooka, R., Numerical simulation of flow field over surface-mounted cube with various second-moment closure models. Preprint of *9th Symposium on turbulent Shear Flows, 1993*.  
(Murakami et al., 1996)
- Murakami, S., Mochida, A., Ooka, R., Kato, S. And Lizuka, S., Numerical Prediction of Flow Around a Building with Various Turbulence Models: Comparison of k- $\epsilon$  EVM, ASM, DSM and LES with Wind Tunnel Tests, *ASHRAE Transaction*, Vol 102, Part 1, pp. 741-753, 1996.  
(Nielsen, 1974)
- Nielsen, P.V., *Flow in Air Conditioned Rooms – Model Experiments and Numerical Solution of the Flow Equations*, Ph.D. Thesis, Technical University of Denmark, 1976.  
(Nielsen, 1994)
- Nielsen, P.V., *Computational Fluid Dynamics in Ventilation*, Department of Building Technology and Structural Engineering, Aalborg University, 1994.  
(Nielsen, 1995)
- Nielsen, P.V., *Lecture Notes on Mixing Ventilation*, Department of Building Technology and Structural Engineering, Aalborg University, Denmark, 1995.  
(Nielsen, 1999)
- Nielsen, P.V., *Lecture Notes on Scale Model Experiments*, Dept. of Building

## References

---

Technology and Structural Engineering, Aalborg University, 1999.

(Olson, 1968)

Olson, R.M., Essentials of Engineering Fluid Mechanics, Second Edition, Intertext Books, London, 1968.

(Orme et al., 1994)

Orme, M., Liddament, M. and Wilson, A., *Numerical data for air infiltration and natural ventilation calculations*, Technical Note AIVC 44, Orme, Liddament and Wilson, 1994, ISBN 1-946075-97-2.

(Ower and Panckhurst, 1977)

Ower, E., and Panckhurst, R.C., The Measurement of Airflow, 5<sup>th</sup> Edition, Pergamon Press, 1977.

(Pettersen et al., 1969)

Pettersen et al., Byggnadsaerodynamik – Revy over Aktuella Frågeställningar, Rapport från Bygghforskningen, Stockholm, 1969.

(Rajaratnam, 1976)

Rajaratnam, N., Turbulent Jets, Developments in water Science, Elsevier, 1976

(Rodi, 1984)

Rodi, W., Turbulence Models and their Application in Hydraulics – A State of the Art Review, Second Revised Edition, 1984.

(Rösler, 2001)

Rösler M, Grundman (2001), WG-B5 IEA Annex 35 Technical Report, “CFD-Predictions for a disk in a Tunnel”, Dresden University of Technology.

(Sandberg 2002)

Sandberg M. (2002) “Airflow through Large Openings-A catchment problem?”, Proceedings Roomvent 2002 Denmark Copenhagen, pp. 541-544

(Sandberg, 2001)

Sandberg M. (2001), WG-B5 IEA Annex 35 Technical Report, “Wind Flow through Large Openings”, University of Gävle.

(Sandberg, 2002a)

Sandberg, Mats, Wind induced airflow through large openings: summary, University of Gävle, Annex 35 technical report. 2002.

(Sandberg, 2002b)

Sandberg, Mats, Airflow through large openings-A catchment problem?, University of Gävle, Roomvent 2002, pp. 541-544.

## References

---

(Sawachi, 2002)

Sawachi T (2002) "Detailed observation of cross ventilation and air flow through large openings by full scale building model in wind tunnel" Proceedings Roomvent 2002 Denmark Copenhagen, pp. 565-568

(Schlichting, 1979)

Schlichting, H., Boundary Layer Theory, McGraw-Hill, New York, 1979.

(Schwarz and Cosart, 1960)

Schwarz, WH. and Cosart, WP., The Two Dimensional Turbulent Wall Jet, Journal of Fluid Mechanics, 10, pp. 481-495, 1960.

(Sforza and Herbst, 1970)

Sforza, WH. and Herbst, G., A Study of Three Dimensional Incompressible Turbulent Wall Jets, AIAA Journal., 1970.

(Shih et al., 1995)

Shih, T., Liou, W., Shabbir, A., Yang, S., Zhu, J., *A New Eddy Viscosity Model for High Reynolds Number Turbulent Flows*, Computers Fluids Vol. 24, No. 3, pp. 227-238, 1995.

(Shih et al., 1995)

Shih, T., Liou, W., Shabbir, A., Yang, S., Zhu, J., *A New Eddy Viscosity Model for High Reynolds Number Turbulent Flows*, Computers Fluids Vol. 24, No. 3, pp. 227-238, 1995.

(Spitglass, 1922)

Spitglass, JM., Orifice coefficients - data and results of tests, Transaction A.S.M.E. 44 (1922).

(Sprenkle, 1962)

Sprenkle, RE., The thin plate orifice for flow measurement, Flow measurement in closed conduits, Paper B-1, vol. I, 127, H.M.S.O., Edinburgh (1962)

(Summers et al., 1986)

Summers, DM., Hanson, T. and Wilson, CB., Validation of a Computational Simulation of Wind Flow over a Building Model, Building and Environment, Vol. 21, 2, pp. 97-111, 1986.

(Svidt et al., 2000)

Svidt, K., Heiselberg, P., Nielsen, P.V. Characterization of the Airflow from a Bottom-Hung Window under Natural Ventilation. *Proceedings of ROOMVENT 2000, July 9-12, Reading, UK.*

(Verhoff, 1963)

Verhoff, A., The Two Dimensional Turbulent Wall Jet with and without an

## References

---

External Free Stream, Report No. 626, Princeton University, 1963.

(Versteeg et al., 1995)

Versteeg, HK and Malalasekera, W., An Introduction to Computational Fluid Dynamics – The finite Volume Method, Longman Group Ltd., 1995, ISBN: 0-582-21884-5.

(Waschke, 1974)

Waschke, G., Über die Lüftung mittels isothermer turbulenter radialer Deckenstrahlen, Dissertation, RWTH, Aachen, Germany, 1974.

(Yakot and Orszag, 1986)

Yakhot, V., Orszag, S. A. *Renormalization group analysis of turbulence I. Basic theory*, Journal of Scientific Computing. 1986, 1 (1) , p. 3-51

(Zhang and Chen, 2000)

W. Zhang, Q. Chen, Large eddy simulation of indoor airflow with altered dynamic subgrid scale model, Int. J. Heat Mass Transfer 43 (17) (2000) 3219–3231.